

STATUS REPORT
(Seventh Yearly Report for the Period
1 June 1966 to 31 May 1967)

NONLINEAR ASPECTS OF COMBUSTION INSTABILITY
IN LIQUID PROPELLANT ROCKET MOTORS

by

L. Crocco, D.T. Harrje, W.A. Sirignano
F.V. Bracco, C.E. Mitchell, P.K. Tang, R.M. Williams,
G.R. Black and W.A. Stinger

prepared for

NATIONAL AERONAUTICS AND SPACE ADMINISTRATION

June 1967

CONTRACT NASr-217

Technical Management
NASA Lewis Research Center
Cleveland, Ohio
Chemistry and Energy Conversion Division
Marcus F. Heidmann

Guggenheim Laboratories for the Aerospace Propulsion Sciences
Department of Aerospace and Mechanical Sciences
PRINCETON UNIVERSITY
Princeton, New Jersey

RSL	_____
JAS	_____
FEC	_____

AUG 28 1967

TABLE OF CONTENTS

	Page
TITLE PAGE	1
TABLE OF CONTENTS	2
I. <u>SUMMARY</u>	3
II. <u>INTRODUCTION</u>	6
III. <u>ENERGY SOURCES</u>	
A. Use of Shock Waves to Study Combustion Parameters	9
B. Experimental Shock Wave Studies	21
C. Mixture Ratio Gradient Measurements	25
D. Droplet Population Density Investigation	38
E. Vapor Displacement and Stream Breakup Experiments	41
IV. <u>DAMPING DEVICES</u>	
A. Theoretical Studies of Flow Behavior with Acoustic Liners	44
B. Experimental Liner Studies	53
V. <u>EXTENSIONS TO THE THEORY</u>	
A. Shock Wave Instability in the Axial Mode	60
B. Nonlinear Transversal Instability	68
C. Droplet Burning Under Oscillatory Conditions	70
D. Numerical Calculation of Wave Phenomena in Chambers	92
REFERENCES	96
FIGURES AND TABLES	
DISTRIBUTION LIST	

I. SUMMARY

To investigate steady-state combustion and to evaluate energy sources for sustaining combustion instability, shock wave propagation through the combustion zone of a liquid propellant rocket motor is under investigation in a theoretical-experimental program. Six equations with nine unknowns can be written for the region of interest within the chamber. Evaluation of parameters immediately before and immediately after the passage of the shock front will be utilized in the equation solution. The goal of the research is to produce a method by which most of the steady-state combustion parameters can be calculated after having measured only the static pressure immediately before and immediately after the passage of the shock and the shock velocity. (III-A)*

The experimental program is being conducted with the square-motor hardware. An upgrading of the experimental technique from that previously reported¹ has been necessary in order to meet the accuracy requirements for parameter measurement. Different transducers have been chosen, together with vastly improved recording capabilities. The initial shock pulse has been tailored to more closely resemble a step-function to aid in the determination of the peak pressure. Static pressure survey techniques² have also been further refined. Streak photography is providing important secondary data as well as supplying a means for checking the prime source of shock velocity measurement, the axial array of pressure transducers. (III-B)

Mixture ratio surveys of the injector types employed in these square-motor tests have been conducted with thermocouple probes. This technique, using heated pseudo-oxidizer and room temperature RP-1, has been found very helpful in following the extremely rapid mixture ratio gradients immediately downstream of the injector face. Spray interpenetration can be modeled via Gaussian distributions. (III-C)

Extensions to the work on droplet population density variations,^{1,2} as a possible source of intermediate frequency instability, have continued. The effects of additional parameters have been investigated and a non-dimensional empirical relationship was derived. (III-D)

Studies within a pseudo rocket environment to investigate the vapor

* Refers to Chapter and Section.

displacement mechanism for combustion instability have also continued. The droplet generator when run in conjunction with the horns, which generate the tangential wave motion, has allowed sufficient separation of the individual droplets to view the vapor sheaths individually. However, the data are qualitative and indications are that significant vaporization increases are to be found at locations where velocity or pressure is maximized, with the former location producing the greatest effect. (III-E)

A simplified nonlinear model of the gasdynamic oscillations in acoustic liner cavities and orifices, and near lined surfaces has been developed and analyzed. The resulting nonlinear system of ordinary differential equations has been numerically integrated for certain combustion chamber oscillations, thereby determining orifice velocity and cavity pressure versus time. This information is used to calculate the liner admittance coefficient which is the important stability parameter. (IV-A)

To evaluate the analytical predictions of the behavior of acoustic resonator cavities, a chamber section employing 53 individually adjustable resonators has been fabricated and tested on the 9-inch diameter, transverse mode hardware. The tests have involved unlike doublets and like-on-like doublets of low and high impingement angle as well as the use of an annular motor in addition to the tests on conventional hardware where pulsing can be supplied. In these tests there are injector configurations which were "triggered" into high frequency instability and such instability could be suppressed with what were often relatively small increases in damping. Damp times were influenced by the number of "active" resonator cavities. The placement of the damping was also shown to play a significant role. On the other hand, suppression of pressure oscillations in spontaneously unstable tests using unlike injector designs would appear to be a more difficult task. Amplitude decreases were found but stability could not be attained, at least within the limitations of the acoustic liner design tested. In those tests the tuning of the cavities switched the instability to another tangential mode rather than providing stability. (IV-B)

Extensions of the sensitive time-lag theory to the nonlinear regime

have been developed in both the longitudinal and transverse cases. In the longitudinal case, both concentrated and distributed combustion are considered. Oscillations with shock waves are found, although in a limited range of the τ , n plane near the linear stability limits continuous wave forms are found. The possibility of triggering is indicated for operation near the stability limits. Distributed combustion is more stable than concentrated combustion. (V-A)

The transverse mode was studied in the special case of thin annular chambers. Again, oscillations with shock waves are typical and triggering is possible. However, the stability of this mode is not as sensitive to the combustion distribution as the longitudinal mode is. In another analysis of this transverse case, a simplified droplet burning model was employed instead of the sensitive time-lag model. Due to the simplifications, no phase lag in the combustion response appeared and only one combustion stability parameter (analogous to n) appeared. (V-B)

A more complete study of the linear combustion response with a quasi-steady droplet burning model has been performed. A small perturbation analysis has been performed and both the steady-state and perturbation equations have been solved by numerical means. From these results the combustion response factor is calculated. Under special conditions, the response factor maximizes in a certain frequency range indicating a time-lag behavior. (V-C)

The transverse wave motion and shock formation in chambers are being studied by numerical means. In the first attempt, thin annular chambers have been considered. A new numerical technique which involves a rotating frame of reference has been employed and the results compare favorably with those obtained by a standard technique. In the thin annular case, wave steepening and shock formation occur. (V-D)

II. INTRODUCTION

This is the Seventh Yearly Report on the research at Princeton University on the problem of combustion instability in liquid propellant rocket motors. These investigations are being sponsored by the National Aeronautics and Space Administration under NASA Contract NASr-217 and, in the past, under NASA Grant NsG-99-60. The nonlinear aspects of the problem have been emphasized in both the theoretical and experimental portions of the program. Presently, the theoretical research is concentrating on studies of possible mechanisms of combustion instability such as droplet burning, the nonlinear gasdynamic oscillations associated with combustion instability involving shock-type waves in both the tangential and longitudinal modes, the effect of damping devices on stability with particular emphasis on nonlinear effects associated with acoustic liners, and fundamental studies of the basic energy sources. In connection with the theoretical program, an experimental program of equally broad range is being conducted. This program includes basic experiments with rocket motors and "cold" chambers which have been designed to study various phases of the combustion process and/or the instability phenomena to provide understanding which would prove useful in the construction of theoretical models. It also includes studies of the effects of exhaust nozzles and damping devices upon the instability as well as controlled testing of liquid rocket motors with parametric variations intended to determine the factors which strongly influence the incidence of nonlinear combustion instability.

In the theoretical study of mechanisms of combustion instability, the greatest difficulty involves the construction of the model or models which contain the essential physical aspects of the phenomena. In this respect the basic experiments are extremely useful. The theoretical study of the nonlinear gasdynamic oscillations presents another type of difficulty. Generally, mathematical techniques for the treatment of nonlinear partial differential equations are not well-developed and, in most cases, they are undeveloped. Therefore, the theoretician must develop techniques as he works with the physical problem. In Sections V-A and V-B of this report, certain nonlinear problems are discussed together with the special

techniques developed for their solutions. It is the evolution of analytical techniques which controls the rate of progress with the nonlinear problems. Often, linear mathematical approaches have proven useful in effecting a better understanding of the nature of the instability. Therefore, a linear treatment has also been used in this report to analyze droplet burning.

As is the norm for any status report, a considerable amount of the material discussed herein is in the state of active investigation. Thus, only tentative conclusions or observations are sometimes possible. At least a mention of one example of each type of work being conducted has been made so that this report would prove to be of maximum benefit to those readers working in similar areas.

During the past year the following technical reports, papers and book have been (or are about to be) published:

"Axial Mode Shock Wave Combustion Instability in Liquid Propellant Rocket Engines", C. E. Mitchell, Department of Aerospace and Mechanical Sciences Technical Report No. 798, July 1967. (NASA CR-72259)

"A Preliminary Study of the Effects of Vaporization and Transverse Oscillations on Jet Breakup", J. A. Newman, Department of Aerospace and Mechanical Sciences Technical Report No. 785, July 1967. (NASA CR-72258)

"Experimental Investigations of Liquid Propellant Combustion Processes Using Streak Photography", R. M. Williams, Jr., Department of Aerospace and Mechanical Sciences Technical Report No. 800, July 1967.

"Acoustic Liner Studies", W. A. Sirignano, L. Crocco and D. T. Harrje, ICRPG 3rd Combustion Conference, CPIA Publication No. 138, Vol. 1, February 1967, pg. 581.

"A Theoretical Study of Nonlinear Combustion Instability in Liquid Propellant Rocket Motors", B. T. Zinn, Ibid, pg. 444.

"Axial Energy Distribution Studies in a Liquid Propellant Rocket Motor", D. T. Harrje and L. Crocco, Ibid, pg. 523.

"Longitudinal Shock Wave Combustion Instability in Liquid Propellant Rocket Engines", C. E. Mitchell, L. Crocco, W. A. Sirignano, Ibid, pg. 395.

"Effect of the Transverse Velocity Component on the Nonlinear Behavior of Short Nozzles", L. Crocco and W. A. Sirignano, AIAA Journal, Vol. 4, No. 8, August 1966, pg. 1428.

Behavior of Supercritical Nozzles Under Three Dimensional Oscillatory Conditions, L. Crocco and W. A. Sirignano (in the process of being published as an AGARD Monograph).

Another paper is scheduled to be presented in the next few months the title is:

"Nonlinear Wave Phenomena in Liquid Rocket Combustion Chambers", L. Crocco, C. E. Mitchell and W. A. Sirignano, to be presented at the Colloquia on Gas Dynamics of Explosions, Brussels, Belgium, September 1967.

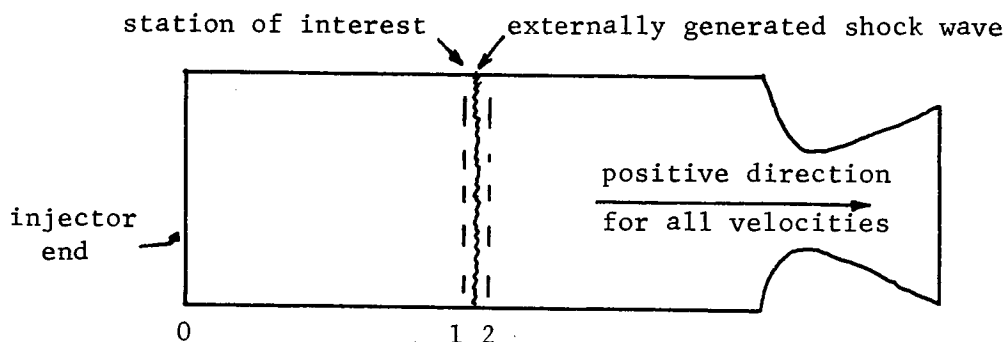
Additional background and history of the research on combustion instability at Princeton University may be found in the partial list of References 1 - 11. In addition, Reference 12 represents the final report in an extensive series of reports on earlier work primarily concerned with the linear type of combustion instability (i.e., spontaneous buildup from steady-state operation).

It should be acknowledged that this work made use of computer facilities supported in part by National Science Foundation Grant NSF-GP579.

III. ENERGY SOURCES

A. USE OF SHOCK WAVES TO STUDY COMBUSTION PARAMETERS

It has long been felt that information on the steady-state combustion parameters can be gained by studying the propagation into the combustion chamber of an externally generated shock.^{1,13,14} Consider the following sketch:



If a steady-state is assumed to exist between the injector end (station 0) and the station of interest (station 1), the mass, momentum, and energy conservation equations between these two sections can be written in algebraic form. The same three principles can also be applied through the shock, thus relating the combustion parameters at the station of interest just before the arrival of the shock, to the shock velocity and to the same parameters immediately after the shock front. Thus six equations become available and, as it will presently be seen, they contain the following nine unknowns: density, pressure and velocity of the gaseous phase, and density and velocity of the liquid phase at the station of interest just before the arrival of the shock, density, pressure and velocity of the gaseous phase at the station of interest immediately after the shock front and the shock velocity. Thus if any three of the above nine parameters are measured the other six can be calculated. The most important element of this approach is having considered as unknowns the parameters immediately after the shock front instead of the parameters way down stream after the shock front in, or at the end of, the expansion wave. Since the velocity immediately after the shock front is subsonic with

respect to the local speed of sound, the shock velocity and all the shock parameters are functions of whatever adjustments the gaseous and liquid phases undergo in the expansion following the shock front. Thus all these adjustments must be included in the equations if the parameters in, or at the end of the expansion wave are considered as unknowns. This requires that the nature of these adjustments be postulated and that new unknowns be introduced with the final result that too many variables must be measured to solve for the others or that only qualitative information can be gathered from the equations. On the other hand, the parameters immediately after the shock front can be related to those immediately before the shock front by the Rankine-Hugoniot equations without knowledge of the down stream adjustments. It is still necessary to postulate what changes occur through the front of the shock but these changes can be understood more easily than the entire adjustments occurring in the expansion waves. For instance, considering that the shock thickness is of the order of a few mean-free-paths, it can be postulated that no droplet shattering will occur at the shock front. The problem is that of a shock going around a spherical obstacle. The unsymmetrical load will deform the drop which eventually will break, perhaps after some oscillations. This is particularly evident if the shock is of moderate intensity in which case the unsymmetrical load due to the shock is counteracted by the inertia and surface tension of the drop. Thus it can be postulated that there is no droplet shattering through the front of a moderate shock.

More specifically, it is assumed:

1. Steady-state between the injector end and the station of interest.
2. One-dimensional flow.
3. Instantaneous vaporization of the oxidizer and distributed vaporization of the fuel.
4. That mass, energy, and momentum of the droplets do not change through the shock front.
5. That the shock front is a plane one and moving parallel to the flow direction.
6. That the fuel droplet temperature is equal to the boiling temperature of the fuel.

7. That gaseous fuel and oxidizer react immediately to give equilibrium reaction products.

Of the above assumptions only the first one is essential to the application of this method. The others could be partially or totally removed by modifying the equations presently used.

The main goal of this research is to produce a method by which most of the steady-state combustion parameters can be calculated after having measured only the static pressure immediately before and immediately after the shock and the shock velocity. This method of investigation could be applied to most rocket engines of current interest.

The main difficulty, besides that of solving a system of several nonlinear equations, is in determining the accuracy of the calculated parameters as a function of the accuracy of the measurements and of the assumptions made.

The Equations

The equations are now given and then their meaning and their solution will be discussed. c.g.s. units are used unless otherwise specified.

$$\dot{w}_F + \dot{w}_O = \rho_e u_e A + \rho_i u_i A \quad (1)$$

$$\dot{w}_F u_{xF} + \dot{w}_O u_{xO} + p_0 A - 4 \pi \frac{S}{D} \left(\frac{1}{2} \rho_i u_i^2 \right) A = A \rho_e u_e^2 + A \rho_i u_i^2 + A p_i \quad (2)$$

$$\begin{aligned} & \dot{w}_F \left[\frac{u_{0F}^2}{2} - c_F (T_{varF} - T_{0F}) - Q_{varF} - c_{pF} (298 - T_{varF}) \right] + \\ & \dot{w}_O \left[\frac{u_{0O}^2}{2} - c_O (T_{varO} - T_{0O}) - Q_{varO} - c_{pO} (298 - T_{varO}) \right] - \lambda A \left(\frac{\Delta T}{\Delta R} \right) - \lambda A \left(\frac{\Delta T}{\Delta x} \right) = \\ & = \rho_i u_i A \left[E_i - H_i + \frac{u_i^2}{2} + \frac{p_i}{\rho_i} \left(1 - \frac{\rho_e}{\rho_i} \right) \right] + \rho_e u_e A \left[\frac{u_e^2}{2} - c_{pF} (298 - T_{varF}) - Q_{varF} \right] \end{aligned} \quad (3)$$

$$\rho_1 (u_1 - U) = \rho_2 (u_2 - U) \quad (4)$$

$$\left(1 - \frac{\rho_e}{\rho_i} \right) (p_1 - p_2) = \rho_2 (u_2 - U)^2 - \rho_1 (u_1 - U)^2 \quad (5)$$

$$(E_2 - E_1) - (H_2 - H_1) = \left(\frac{p_2 + p_1}{2} \right) \left(\frac{1}{p_1} - \frac{1}{p_2} \right) \left(1 - \frac{p_e}{p_L} \right) \quad (6)$$

$$u_{oF} = \dot{\omega}_F / p_L A_{IF} \quad ; \quad u_{o\phi} = \dot{\omega}_\phi / p_{L\phi} A_{I\phi} \quad \text{OR:} \quad (7)$$

$$u_{oF} = \left[u_F^2 + 2\beta \frac{(p_F - p_0)}{p_L} \right]^{1/2} \quad ; \quad u_{o\phi} = \left[u_\phi^2 + 2\beta \frac{(p_\phi - p_0)}{p_{L\phi}} \right]^{1/2} \quad (8)$$

$$u_{x_F} = u_{oF} \cos \theta \quad ; \quad u_{x\phi} = u_{o\phi} \cos \theta \quad (9)$$

$$Z = \frac{\dot{\omega}_\phi W_{TF}}{W_{T\phi} (\dot{\omega}_F - p_e u_{eA})} \quad (10)$$

$$C_2 H_6 O_C + Z O_2 \rightarrow X_1 OH + X_2 CO + X_3 CO_2 + X_4 O + X_5 O_2 + X_6 H_2 + X_7 H_2O + X_8 H \quad (11)$$

$$W_{TEN} = a(12.011) + b(1.008) + (c + 2Z)(16.00) \quad (12)$$

$$Y_i = \sum_{i=1}^8 x_i \quad (13)$$

$$x_2 + x_3 = a \quad (14)$$

$$x_1 + 2x_6 + 2x_7 + x_8 = b \quad (15)$$

$$x_1 + x_2 + x_3 + x_4 + 2x_5 + x_7 = c + 2Z \quad (16)$$

$$\log_{10} \left\{ \frac{x_4}{x_5^{1/2}} \left[\frac{p_1 10^{-6}}{Y_1} \right]^{1/2} \right\} + \frac{1.3425 10^4}{T_1} - 3.528 = 0.0 \quad \frac{1}{2} O_2 \rightleftharpoons O \quad (17)$$

$$\log_{10} \left\{ \frac{x_8}{x_6^{1/2}} \left[\frac{p_1 10^{-6}}{Y_1} \right]^{1/2} \right\} + \frac{1.2035 10^4}{T_1} - 3.213 = 0.0 \quad \frac{1}{2} H_2 \rightleftharpoons H \quad (18)$$

$$\log_{10} \left\{ \frac{x_1}{x_5^{1/2} x_6^{1/2}} \right\} + \frac{0.1185 10^4}{T_1} - 0.668 = 0.0 \quad \frac{1}{2} O_2 + \frac{1}{2} H_2 \rightleftharpoons OH \quad (19)$$

$$\log_{10} \left\{ \frac{x_7}{x_6 x_5^{1/2}} \left[\frac{p_1 10^{-6}}{Y_1} \right]^{-1/2} \right\} - \frac{1.327 10^4}{T_1} + 3.085 = 0.0 \quad H_2 + \frac{1}{2} O_2 \rightleftharpoons H_2O \quad (20)$$

$$\log_{10} \left\{ \frac{x_3}{x_5^{1/2} x_2} \left[\frac{p_1 10^{-6}}{Y_1} \right]^{-1/2} \right\} - \frac{1.423 10^4}{T_1} + 4.265 = 0.0 \quad CO + \frac{1}{2} O_2 \rightleftharpoons CO_2 \quad (21)$$

$$p_i = \frac{Y_i (8.31431 10^7) T_1 p_1}{W_{TEN} (1 - p_e/p_L)} \quad (22)$$

$$H_1 = - (4.186 10^{10}) \left\{ x_1 (9.33) + x_2 (-26.416) + x_3 (-94.04) + x_4 (59.56) + \right. \quad (23) \\ \left. + x_5 (0.0) + x_6 (0.0) + x_7 (-57.798) + x_8 (52.102) - [\Delta H_f^\circ]_F - Z[0.0]_O \right\} / W_{TEN}$$

$$E_1 = (4.186 \cdot 10^{10}) \sum_{i=1}^8 \left\{ x_i \int_{298}^{T_1} c_{p_i} dT - (1.987)(T_1 - 298) x_i \right\} / W_{TEH} \quad (24)$$

where c_{p_i} are polynomial curve fits of molar specific heats at constant pressure versus temperature for each of the 8 products

Equations 25 to 36 are formally equal to Equation 13 through 24 but have $p_2, T_2, Y_2, \rho_2, H_2, E_2$ instead of $p_1, T_1, Y_1, \rho_1, H_1, E_1$.

In the above equations the subscript 0 refers to the injector end, 1 to the station of interest immediately before the shock arrives, 2 to the station of interest immediately after the shock arrives, and ℓ to the liquid phase (fuel droplets).

Equation 1 expresses the mass conservation between station 0 and station 1 at which some liquid fuel (ρ_ℓ = grams of liquid fuel per unit volume of the combustion chamber) may exist and move with the velocity u_ℓ .

Equation 2 expresses the momentum conservation between stations 0 and 1. Since fuel and oxidizer are usually injected at an angle with respect to the axis of the combustion chamber (θ), only the components of their velocities along the axis appear in the momentum equation (u_{x_F}, u_{x_θ}). These velocities are related to the feed line velocities and pressures by Equations 8 and 9 where a discharge coefficient (β) takes into account possible losses through the injectors. The initial momentum of the liquid, although small, is still important in the momentum equation since it is of the same order of the loss of static pressure ($p_0 - p_1$) and therefore it is equally important in influencing the velocities of the gaseous and liquid phases (u_1, u_ℓ).

Equation 3 expresses the energy conservation between stations 0 and 1. In this equation E_1 is the internal energy per gram of products (gaseous phase) and H_1 is the heat released by the chemical reaction per gram of products. In both cases the reference temperature is $298^\circ K$. This equation was obtained just on physical reasoning but can also be derived

from the usual steady one-dimensional conservation equation as follows.

Starting from:

$$\dot{m} \left[h + \frac{1}{2} u^2 \right] - \mu u u_x - \lambda T_x - q_x = \text{CONSTANT}$$

where $h = c_p (T - 298) + h^0$ = latent plus formation enthalpy per unit mass. Neglecting viscous dissipation and applying it at stations 0 and 1 it is found:

$$\begin{aligned} & \dot{w}_F \left[c_F (T_{0F} - T_{\text{VAP}_F}) + c_{pF} (T_{\text{VAP}_F} - 298) + H_F^0 + \frac{u_{0F}^2}{2} \right] + \\ & \dot{w}_O \left[c_O (T_{0O} - T_{\text{VAP}_O}) + c_{pO} (T_{\text{VAP}_O} - 298) + H_O^0 + \frac{u_{0O}^2}{2} \right] - \\ & - \left[\lambda A T_x + k A_1 \left(\frac{\Delta T}{\delta R} \right)_1 + (\dot{w}_F - \rho_e u_e A) Q_{\text{VAP}_F} + \dot{w}_O Q_{\text{VAP}_O} \right] = \\ & = \rho_i u_i A \left[\sum c_p (T_i - 298) + \sum H_p^0 + \frac{u_i^2}{2} \right] + \rho_e u_e A \left[c_{pF} (T_{\text{VAP}_F} - 298) + H_F^0 + \frac{u_e^2}{2} \right] \end{aligned}$$

In the above equation, H_F^0 , H_O^0 , H_p^0 are enthalpies per gram of fuel, oxidizer and products respectively. Hence :

$\sum c_p (T_i - 298) = E_i + \frac{P}{\rho_i} (1 - \rho_e / \rho_L)$ = enthalpy per gram of products. Then comparing this equation with Equation 3 it is seen that they are equal if:

$$- \rho_i u_i A H_i = \rho_i u_i A \sum H_p^0 - (\dot{w}_F - \rho_e u_e A) - \dot{w}_O H_O^0$$

That the above equation is verified can be seen by substituting in its right end side the definitions of H_i and z from Equations 10 and 23 and using the mass conservation (Equation 1) i.e.:

$$- \rho_i u_i A H_i = - \rho_i u_i A \left\{ - \frac{\sum H_p^{0*} - H_F^{0*} - z H_O^{0*}}{W_{T_{EN}}} \right\}$$

and substituting the following expressions:

$\sum H_p^{0*}$ = enthalpy of formation of the products per mole of fuel

$H_F^{0*} = H_F^0 W_{T_F}$ = enthalpy of formation per mole of fuel

$H_O^{0*} = H_O^0 W_{T_O}$ = enthalpy of formation per mole of oxidizer

$$\begin{aligned}\sum H_p^0 &= \frac{\sum H_p^{0*} (\dot{w}_p - \rho_e u_e A)}{W_{TF} (\rho_i u_i A)} = \text{enthalpy of the products per gram of products} \\ W_{TEH} &= W_{TF} + z W_{T\phi} = \text{molecular weight of the equivalent mole} \\ z &= \frac{\dot{w}_\phi W_{TF}}{W_{T\phi} (\dot{w}_p - \rho_e u_e A)} = \text{moles of oxidizer per mole of fuel} \\ \rho_i u_i A &= (\dot{w}_p - \rho_e u_e A) + \dot{w}_\phi = \text{grams of products per second}\end{aligned}$$

In the energy equation the term $\kappa A, (\Delta T / \Delta R)$, takes into account heat losses through the combustion chamber walls from station 0 to station 1 (including the injector end surface), and $\lambda A (\Delta T / \Delta x)$ heat losses through the plane passing by station 1 and parallel to the injector end surface. Finally notice that the heat of vaporization of the fuel, which is usually included in the heat of formation of the fuel (since the fuel at $298^\circ K$ is in the liquid phase) is in Equation 3 considered explicitly.

Equations 4 and 5 express mass and momentum conservation through the shock front. The coefficients $1 - \rho_e / \rho_L$ takes into account the fact that when some liquid fuel is present the effective density of the gas is higher. If ρ_i is the grams of products per unit volume of the combustion chamber, ρ_e the grams of liquid fuel per unit volume of the combustion chamber, ρ_L the grams of liquid per unit volume of liquid (equal to the specific gravity of the fuel in the c.g.s. system) then the effective density of the products is $\rho_i / (1 - \rho_e / \rho_L)$. This corrective factor is always small ($\rho_e / \rho_L \leq 10^{-3}$) and could possibly be neglected.

Equation 6 expresses the energy conservation through the shock front. The terms E_1, E_2, H_1, H_2 which are energies and enthalpies per gram of products before and after the shock, are related to the temperatures and pressures before and after the shock by Equations 10 through 24 and 25 through 36 respectively. They are also related to the presence of liquid fuel by Equation 10. Equations 10 through 24 and 25 through 36 express chemical equilibrium among the products before and after the shock. Equations

tion 10 takes into account that not all the injected fuel is available for chemical reaction since part of it is still in the liquid phase. Thus the fuel to oxidizer ratio changes with the distance from the injector end.

Equation 11 is not an algebraic equation to be solved with the others but merely defines which products are being considered.

Equation 12 defines the molecular weight of the "Equivalent Mole: $C_a H_b O_{c+2z}$ " which is the mass of reactants per mole of fuel.

Equation 13 defines the total number of mole per mole of fuel.

Equations 14, 15, and 16 express the conservation of carbon, hydrogen, and oxygen respectively.

Equations 17 through 21 define the chemical equilibrium between the species indicated on the right of the same equations.

Equation 22 is the perfect gas equation of state.

Equations 23 and 24 define H_i and E_i in terms of the chemical composition of the products and of their temperature.

As previously stated, Equations 25 through 36 are formally equal to Equations 13 through 24 but they refer to quantities immediately after the shock.

All the constants appearing in Equations 17 through 24 either come directly from "JANAF" tables or are curve fits of data available there.

Solution of the Equations

In the first six of the 36 equations presented, the unknowns are: $p_1, p_2, u_1, p_e, u_e, p_2, p_2, u_2, U$. The other parameters are either known constants or are defined in terms of the previous ones by Equations 7 through 36. In particular this is the case for the internal energies (ϵ_1, ϵ_2) and the enthalpies (H_1, H_2), which are functions of p_1, T_1, p_2, T_2 , and $p_e u_e A$ through the chemical processes occurring in the combustion chamber described by Equations 7 through 36. Thus all the 36 equations (actually 35, excluding Equation 11) should be solved

simultaneously. After a few substitutions they can be reduced to about 20 nonlinear complicated equations which are still too many to be solved simultaneously. Thus they must be broken into groups and iterations must be used among groups. In the present attempt to solve those equations the fact is used that the product $\rho_e u_e A$ decreases constantly with increasing distance from the injector end. It represents the mass flux of liquid fuel which must decrease since the liquid fuel can vaporize but it cannot condense. Moreover this product is equal to zero far from the injector end where no liquid is present. Starting where

$\rho_e u_e A = 0$ and using experimentally measured p_1 , p_2 and U , Equations 10 through 36 can be solved for $E_1, H_1, Y_1, E_2, H_2, Y_2$ for various temperatures: T_1, T_2 . Curve fitting these solutions the following functions are determined: $E_1 = E_1(T_1)$; $H_1 = H_1(T_1)$; $Y_1 = Y_1(T_1)$; $E_2 = E_2(T_2)$; $H_2 = H_2(T_2)$; $Y_2 = Y_2(T_2)$ which give $E_1, H_1, Y_1, E_2, H_2, Y_2$ for any values of T_1 and T_2 . The use of these curve fittings is consistent with the fact that the chemical equilibrium equations (Equations 17 through 21 and 29 through 33) and the equations for c_{H_i} are curve fits of experimental results. All these curve fits are expected to be accurate to the fourth significant digit. Next two specific volumes are introduced:

$$v_1 = \frac{Y_1 (8.31431 \cdot 10^7) T_1}{p_1 W_{T_{en}} (1 - p_e/p_L)} \quad (37)$$

$$v_2 = \frac{Y_2 (8.31431 \cdot 10^7) T_2}{p_2 W_{T_{en}} (1 - p_e/p_L)} \quad (38)$$

Then Equations 1 and 2 are solved for p_e and u_e , and Equations 4 and 5 for u_1 and u_2 while Equations 3 and 6 are left unchanged:

$$p_e = \frac{(C_1 - u_1/v_1)^2}{(C_2 - u_1^2 (1 + 2f_{\frac{5}{2}})/v_1)} \quad (39)$$

$$u_e = \frac{(C_2 - u_1^2 (1 + 2f_{\frac{5}{2}})/v_1)}{C_1 - u_1/v_1} \quad (40)$$

$$u_1 = U + v_1 \left[(p_2 - p_1) \left(\frac{1}{v_1 - v_2} \right) \left(1 - \frac{p_e}{p_L} \right) \right]^{1/2} \quad (41)$$

$$u_2 = U + v_2 \left[(p_2 - p_1) \left(\frac{1}{v_1 - v_2} \right) \left(1 - \frac{p_e}{p_L} \right) \right]^{1/2} \quad (42)$$

$$\frac{u_1}{v_1} \left[E_1 - H_1 + \frac{u_1^2}{2} \right] + u_1 p_1 \left(1 - \frac{p_e}{p_L} \right) - p_e u_e \left[B_3 - \frac{u_e^2}{2} \right] + F_5 = 0 \quad (43)$$

$$(H_1 - E_1) - (H_2 - E_2) - \left(\frac{p_2 + p_1}{2} \right) (v_1 - v_2) \left(1 - \frac{p_e}{p_L} \right) = 0 \quad (44)$$

where:

$$G_1 = (\dot{\omega}_F + \dot{\omega}_\phi) / A$$

$$G_2 = p_0 - p_1 + (\dot{\omega}_F u_{x_F} + \dot{\omega}_\phi u_{x_\phi}) / A$$

$$B_3 = Q_{vnr_F} + c_{p_F} (298 - T_{vnr_F})$$

$$F_5 = \lambda \left(\frac{\Delta T}{\Delta x} \right) + \lambda \frac{A_1}{A} \left(\frac{\Delta T}{\Delta x} \right)_1 - G_3 / A$$

$$G_3 = \dot{\omega}_F \left[\frac{u_{\phi_F}^2}{2} - c_F (T_{vnr_F} - T_{\phi_F}) - Q_{vnr_F} - c_{p_F} (298 - T_{vnr_F}) \right] + \\ + \dot{\omega}_\phi \left[\frac{u_{\phi_\phi}^2}{2} - c_\phi (T_{vnr_\phi} - T_{\phi_\phi}) - Q_{vnr_\phi} - c_{p_\phi} (298 - T_{vnr_\phi}) \right]$$

When $p_e = u_e = 0$, for any T_1 and T_2 Equations 37 and 38 give v_1 and v_2 , Equation 41 gives u_1 so that Equations 43 and 44 become two equations for T_1 and T_2 to be solved simultaneously. Then Equations 39 and 40 must confirm that p_e and u_e are null. If they are different from zero, their values are used to calculate $p_e u_e A$ and then to calculate new $E_1 = E_1(T_1)$; $H_1 = H_1(T_1)$; $v_1 = v_1(T_1)$; $E_2 = E_2(T_2)$; $H_2 = H_2(T_2)$; $v_2 = v_2(T_2)$ and to repeat the process. There is no guarantee that this iteration on $p_e u_e A$ will converge. The fact that the behavior of $p_e u_e A$ is known should help. If it doesn't, the problem can always be solved for several values of $p_e u_e A$ and the value which satisfies the equations best can be considered the solving one. Preliminary results are encouraging but they are not sufficient to deserve discussion.

NOMENCLATURE

a	=	atoms of carbons in the fuel molecule
A	=	combustion chamber cross sectional area (cm^2)
A_1	=	chamber walls area up to the station of interest (cm^2)
b	=	atoms of hydrogen in the fuel molecule
c_F	=	specific heat of the liquid fuel ($\text{erg/g}^\circ\text{K}$)
c_ϕ	=	" " " " " oxidizer "
c_{pF}	=	" " " " " gaseous fuel "
$c_{p\phi}$	=	" " " " " oxidizer "
c_{p_i}	=	" " " " " individual combustion products ($\text{erg/mole}^\circ\text{K}$)
c	=	atoms of oxygen in the fuel molecule
D	=	combustion chamber diameter (cm)
E_1	=	internal energy per gram of products (ref. 298°K) before arrival of the shock (erg/g)
E_2	=	internal energy per gram of products (ref. 298°K) after arrival of the shock (erg/g)
f	=	wall function coefficient
H_1	=	heat per gram of products (ref. 298°K) released before arrival of the shock (erg/g)
H_2	=	heat per gram of products (ref. 298°K) released after arrival of the shock (erg/g)
h	=	heat transfer coefficient to the walls ($\text{erg/sec cm}^\circ\text{K}$)
p_0	=	injector end static pressure (dyn/cm^2)
p_1	=	static pressure at station of interest before arrival of the shock (dyn/cm^2)
p_2	=	" " " " " " after " " " " "
p_F	=	fuel feeding line pressure (dyn/cm^2)
p_ϕ	=	oxidizer " " " "
$Q_{\text{vap}F}$	=	heat of vaporization of the fuel (erg/g)
$Q_{\text{vap}\phi}$	=	heat of vaporization of the oxidizer (erg/g)
S	=	distance of the station of interest from the injector end (cm)
T_1	=	temperature at the station of interest before arrival of the shock ($^\circ\text{K}$)
T_2	=	" " " " " " after " " " " "
$T_{\text{vap}F}$	=	vaporization temperature of the fuel ($^\circ\text{K}$)
$T_{\text{vap}\phi}$	=	" " " " " oxidizer ($^\circ\text{K}$)
T_{0F}	=	feeding line fuel temperature ($^\circ\text{K}$)
$T_{0\phi}$	=	" " " oxidizer temperature ($^\circ\text{K}$)

- u_e = velocity of the liquid fuel at the station of interest (cm/sec)
 u_i = " " " gaseous product at the station of interest before arrival of the shock (cm/sec)
 u_z = velocity of the gaseous product at the station of interest after arrival of the shock (cm/sec)
 u_F = feeding line fuel velocity (cm/sec)
 u_ϕ = " " oxidizer velocity (cm/sec)
 u_{oF} = injector end fuel velocity (cm/sec)
 $u_{o\phi}$ = injector end oxidizer velocity (cm/sec)
 u_{xF} = component of u_{oF} in the axial direction (cm/sec)
 $u_{x\phi}$ = " " $u_{o\phi}$ " " " " "
 U = shock velocity (cm/sec)
 v_i = specific volume of the gaseous products at the station of interest before arrival of the shock (cm³/g)
 v_z = specific volume of the gaseous products at the station of interest after arrival of the shock (cm³/g)
 \dot{w}_F = fuel mass flow (g/sec)
 \dot{w}_ϕ = oxidizer mass flow (g/sec)
 WT_F = molecular weight of the fuel (g/mole)
 WT_ϕ = " " " " oxidizer (g/mole)
 WT_{EH} = " " " " equivalent mole (g/mole)
 x_i = number of moles of product i per equivalent mole
 γ_i = total number of moles of product at the station of interest before arrival of the shock
 γ_z = total number of moles of product at the station of interest after arrival of the shock
 z = effective moles of oxidizer per mole of fuel
 β = discharge coefficient
 θ = angle between the injector axis and the combustion chamber axis
 λ = heat transfer coefficient of the gaseous products (erg/sec cm² K)
 ρ_e = mass of liquid per unit volume of combustion chamber at the station of interest (g/cm³)
 ρ_i = density of the combustion products at the station of interest before arrival of the shock (g/cm³)
 ρ_z = density of the combustion products at the station of interest after arrival of the shock (g/cm³)
 ρ_L = specific gravity of the fuel (g/cm³)
 $\rho_{L\phi}$ = " " " " oxidizer (g/cm³)

B. EXPERIMENTAL SHOCK WAVE STUDIES

Associated with the analytical approach to investigate energy sources, as described in the previous section, is an experimental program being conducted with the square-motor rocket hardware. In recent months this program has centered on experimental refinements deemed necessary to provide the required measurement accuracy. These efforts cover a range of experimental improvements: the pressure transducers to be used in future tests are ablatively protected, flush-mounted piezoelectric (quartz) units with natural frequencies in the 400 KHz range, the tape recording system employs equipment with less than $\pm 1\mu$ second time displacement between channels and with flat FM frequency response to 80 KHz, the streak film recording techniques have been further refined together with a new streak window, the initial shock pulse has been modified to more closely resemble a step-function, and improved means of accurately determining the static pressure profile have been developed. Other tests such as the mixture ratio gradient measurements described in Section C of this Chapter have also helped to better define the early combustion conditions present in the rocket chamber.

Concerning the choice of transducer, the selection was primarily based on prevention of any compromise in the range of frequency response of the recording equipment (80 KHz). Therefore, the choice was limited to transducers whose natural frequency was 3 - 5 times this value, or greater than 240-400 KHz.

We note with great interest the path pursued by Nicholls et al¹⁵ at Michigan in the development of a piezoelectric transducer using a ferroelectric element. In these past months we have also been looking into the possibilities of producing similar pressure measuring instruments, roughly equivalent to the Kistler 603A unit, which would possess characteristics that might even better fit our individual needs from the standpoint of natural frequency, signal output, freedom from acceleration effects, etc. This effort is continuing.

Currently, the plan is to rely on the Kistler 603A units using an .125 inch thickness of RTU 580 ablative coating (a measurement technique developed by Rogero et al at JPL¹⁶). We have found this approach extremely useful in our acoustic liner studies. As in the previous tests, which were conducted to survey the varying conditions that are associated with the passage of a shock wave,¹³ six transducers have been suitably placed in the square-motor.

To maintain time agreement between the six transducers to tolerances of less than one microsecond, all transducer signals pass through a single recording head onto one-inch tape. Detailed tests on our recently acquired Honeywell 7600 equipment indicate that the dynamic time displacement between outside tracks (worst case) is less than \pm one microsecond. Static time displacement error between any two tracks is of the same order. The compound error from static and dynamic combinations also appears to fall within a two microsecond band.

A signal to noise ratio of 48-51 db has been determined using the double-extended range (this is the worst case from a S/N standpoint), recording at 120 ips, playback at 1 7/8 ips, and with phase lock on the capstan. With 1 7/8 ips playback and phase lock on the tape the S/N ratio is reduced to 46 db, however, the time base is preserved. At all higher playback speeds the S/N ratio is not deteriorated by phase locking on the tape. These tests were made on worn Memorex tape to duplicate end of tape life conditions and hence represent a limiting condition.

These data indicate that the noise levels represent less than one percent of the recorded signal. The overall rise time from 10 to 90% of a square wave signal is less than 5 microseconds. These characteristics together with excellent time correlation between channels are deemed necessary to make the detailed wave shape and location measurements which are the key to this experimental program.

Section A shows that the six conservation equations involve nine unknowns, thus for the system of equations to be determinate three of these must be measured experimentally. Two sets of these measurable quantities seem to present themselves. These are the measurements of static pressure behind and in front of the shock, and the shock velocity. Also possible, would be the measurement of gas velocity behind and in front of the shock,

and the shock velocity. The first set seems to be the easiest and will be done with the new pressure instrumentation. The second, which makes use of streak photography, involves difficulty in measuring the velocity immediately behind the shock and will only be used as a rough check on the first technique. However, the streak film can also be used for performance measurements since the gas velocity is directly related to the characteristic exhaust velocity. Also qualitative results should be obtainable from comparison of the pressure traces and the streak films, as well as data on the mixture ratio striations at various axial positions.

The principle modifications to the research motor are the addition of an 8-inch window section for streak photography and the use of the recently developed pulse gun. The 8" window section has 5" slits (of 1/4 inch width) in each side and utilizes plexiglas windows. Thus, streak photographs can be taken with either the combustion light or with backlighting. This chamber section is capable of being placed anywhere within the first 40" of the rocket motor. Mounted on top of the window section are positions for three pressure transducers so that direct comparisons of pressure records and streak films can be made. The streak camera is of the continuous loop variety (as described in Reference 17) with the shutter synchronized with the pulse gun in such a manner that part of the streak record contains the steady conditions and the remainder shows the pressure oscillations following the pulse. A typical streak photograph utilizing the new window is shown as Figure 1 .

The new pulse gun design is the result of the desire to obtain an accurate value of the static pressure immediately behind the shock. The previously used technique produced an exponential decay following the shock and even the best transducers can not respond sufficiently fast to accurately determine the true peak amplitude in such cases.¹⁸ To alleviate this problem a pulse gun has been designed which generates a step-function shaped pulse. This allows the transducer sufficient time to read the true pressure level behind the initial shock wave. This pulse is generated in a similar manner as before,* however, in the present case a much larger charge is used and the combustion products are fed into the chamber at a controlled rate lasting several milliseconds. A picture of a typical

* A rapidly burning charge of gunpowder bursts a calibrated disk supplying the shock wave.

pulse shape can be seen in Figure 2 .

A modification to the run procedure is a result of the new pressure instrumentation. This limits the possible run time to the order of a few hundred milliseconds so that the transducers are not unduly influenced (or damaged) by the heat transfer environment. In order to make runs for these short times a timer was designed to operate the research motor which includes firing the pulse gun and activating the photographic system. Since the start transient on this hardware is very reproducible and is less than 100 milliseconds in duration, it is expected that this system will actually improve data quality by making the operation more uniform to run.

Finally, since steady-state data involving pressure and velocity is important in the model, the previous approach using a ten-tube mercury manometer has been further improved. A remotely operated ten-passage valve has been designed to trap the mercury columns at individual levels once chamber pressure has been established. This eliminates the objectionable column surges (present even with shubbers and porous filters in the lines) associated with starting and shutdown transients. Also photographic and parallax problems are no longer a factor. It is unlikely, due to valve actuation times, that these data can be obtained during a standard run. However, test pressures and mixture ratios can be duplicated within a few percent and these static pressure profiles obtained on longer duration tests.

Preliminary tests are now being performed on the overall system following initial delays with the Honeywell 7600 recorder which was partially destroyed when dropped from a cargo plane at Denver.

C. MIXTURE RATIO GRADIENT MEASUREMENTS

The injector is one of the most critical elements in a rocket propulsion system. Injectors must be designed to meet a number of objectives, including performance maximization, avoidance of unstable conditions, and appropriate heat transfer environment.¹⁹ Unfortunately, the mechanisms which link injector design to these objectives are in many cases little understood.

Although obviously the ideal testing situation would have been in an actual rocket engine, the difficulties associated with measuring mixture ratios under such conditions prohibited this. One must be content to assume that the mixture ratio in cold flow tests approximates that of actual hot tests.

Spacial distribution studies of mixture ratio are of particular importance because mixture ratio distribution has been shown to have a major effect upon the performance of a rocket engine. Recent investigations at Aerojet-General Corporation have employed this effect in theoretical calculations of performance of rocket engines.²⁰ This technique has resulted in a considerable improvement over the old method of calculating performance where this factor was not taken into account.

Therefore, a method of predicting accurately the spacial distribution of mixture ratio would be quite useful. Injectors with low performance potential could then be identified in the design phase at a great saving in time and money which would have been spent in fabrication and testing. It should be emphasized that the approach described here provides data on sharp mixture ratio gradients which are overlooked with more conventional sampling approaches.

The investigations described in this section were meant to shed light on this question of how the propellants mix. A grossly simplified model has been applied to help explain the observed data and to provide clues toward solving the more complex problem of predicting mixture ratio distribution for any given injector.

As suggested before, unstable conditions which may occur in a rocket engine are quite often linked to injector design. The same injectors

(and other similar designs) which are the topic of this report have and are continuing to be used in hot firings here at Princeton to investigate the problem of combustion instability.^{1,13}

Experimental Apparatus and Testing Procedure

The experimental apparatus can conveniently be divided into two parts: 1) the testing facilities and 2) the measuring and recording apparatus. Further, two radically different measuring and recording systems were used at separate times to measure the mixture ratio under the face of the injector. The testing facilities include the testing booth, the injector and chamber section, the associated systems which feed the injector, and a barrel to collect the propellants as they drain off underneath. The apparatus employed in the primary method of measuring and recording data consisted of a moving thermocouple probe rake operated by a motor, Bristol recording charts equipped with re-transmitting slide wires, a helipotter, and the IBM 1620 Computer. The second method of collecting data, which was used only to check the accuracy of the results of some of the tests using the primary method (see page 28), employed a collector device consisting of 81 glass tubes. We shall now discuss each of these systems in further detail.

Testing Facilities

The testing booth is approximately eight feet tall with a base about four feet square. The injector and chamber section is mounted in the top of the booth, and the measuring equipment under the chamber section. One side of the testing booth is glass so that the run may be observed. The barrel to collect the propellants is located in the lower half of the booth.

The propellants, RP-1 and ethylene glycol (pseudo-lox) are contained in separate tanks located on the roof of the building. Both of the tanks are nitrogen pressurized and have a capacity of forty gallons. The tanks have a pressure limit of 630 psi. Cavitating venturis have been placed in both of the propellant feed lines to aid in maintaining the desired mass flow rates.

Primary Method of Measuring and Recording

The primary method of data collection utilizes a moving probe rake on which ten copper-constantan thermocouples are mounted at half inch intervals. Only six of these thermocouples were used in the tests, however, since the other four do not pass under the spray from these injectors. An ice bath is used for the thermocouple reference junction.

Prior to making a run, the oxidizer is heated up to 180 - 190° Fahrenheit by a cal rod heater located in the roof tank system which constantly circulated the ethylene glycol to equalize the temperature throughout the tank. The fuel remains close to 60°F. (depending on the ambient temperature, storage time, etc.). Each run consisted of three different flows while the thermocouple probe moved under the spray. The first flow was fuel only, the second flow oxidizer only, and the third flow consisted of both the fuel and oxidizer. Knowing the temperature of the fuel alone, oxidizer alone, and the mixture at a specific point under the injector face, one can determine the mixture ratio based on the specific heats of each fluid.

In Figures 3 - 4 we can see the path that each of the thermocouples follows relative to the injector. These paths are perpendicular to the rows of fuel elements and oxidizer elements. (In Figure 3 each fuel element is represented by "+" and each oxidizer element by "O".) The mixture ratio attained by this method along each of the thermocouple paths at each of the three axial distances is also plotted in Figures 3 and 4 .

Because of the limited number of recording charts which existed until recently, and lack of sufficient cables leading from the test cell to the recording room, it was possible to obtain readings from only three of the thermocouples at one time. Hence, the thermocouple wires were connected to a system of relays and wired such that either the odd thermocouple readings (i.e. numbers 1, 3, and 5) or the even thermocouple readings (i.e. numbers 2, 4, and 6) would be sent over the lines to the recording room depending on whether the relay switch was on or off.

The system of testing was as follows: for each flow the thermocouple

probe rake rests under the right chamber edge (in Figures 3-4) until the propellant injector temperature reaches a steady value. Then the probe moves from right to left (in Figures 3-4) during which readings from the odd thermocouples are being sent to the recording room. When the probe reaches the left inside chamber edge an automatic relay switch is activated so that readings from the even thermocouples are sent to the recording room instead of the odd, and the probe retraces the path. A helipotter is used to record the position of the thermocouple probe rake.

From the recording room the readings from the thermocouples and helipotter are sent via the retransmitting slide wires to the IBM 1620 Computer. Here the data is punched directly onto computer cards during the run at the rate of two data cards/second or four data points/second. By sending the data directly to the computer rather than taking the readings off the Bristol carts the results have been shown to be more accurate than hand reduction as well as taking much less time.

Second Method of Measuring and Recording

An alternate method of finding mixture ratio data was to use a device which collected samples of the spray underneath the injector. The collecting apparatus consisted of 81 glass tubes $\frac{1}{4}$ inch in diameter arranged in nine rows of nine. The spacing between adjacent tubes was $\frac{1}{2}$ inch. Since the two propellants used are immiscible they separate after being collected, providing individual mass flow measurements. From these samples the mixture ratio can now be determined as well as local mass flow.²¹

This method was used to check the accuracy of the results obtained from some of the tests which employed the primary method of measuring and recording the mixture ratio. To do so, the collector apparatus was put at the same distance from the injector face as the thermocouple probe and the alignment was such that a row of collecting tubes coincided with each of the six thermocouple paths.

The primary method of finding mixture ratio has a great advantage over the second method because we obtain a continuous mixture ratio profile along the thermocouple paths instead of only averaged values at

half inch intervals. Since the mixture ratio may vary a great deal in a half inch space, the results obtained from the primary method are considered more representative of the actual conditions. On the other hand, the second method is basically more accurate since mixture ratio is measured in a much more direct fashion. The second method also provides information regarding mass distribution, which cannot be obtained from the primary method.

The IBM 1620 Computer and Calcomp Plotter were used to reduce and plot the data respectively from these runs.

Discussion of Accuracy

There are of course many sources of error associated with finding the mixture ratio using the thermocouple probe. In this section the more important sources of error will be discussed and estimates given of their magnitude.

The largest source of error results because the thermocouples do not respond instantaneously to temperature variations. As the thermocouple probe moves under the spray the temperature is continually varying, and before a thermocouple can become adjusted to a temperature at one point it has moved to another point at a different temperature. The concentration of liquid streams and droplets plays an important role in the thermocouple response.

The error introduced due to the delayed thermocouple response varies in magnitude depending on the degree of temperature variation, the probe speed, and naturally is a function of the thermocouple junction size. In this probe .010 inch diameter wires were used to maintain position under the loads imposed by the liquid streams and droplets. When the temperature across the injector face is approximately constant (as it is when the fuel alone is flowed or the oxidizer alone) the error introduced is small. Where the mixture ratio varied greatly, however, (for instance the runs with the Type IV injectors at the 3-inch axial station) quite large errors resulted from delayed response. In the majority of runs the error introduced by the time delay was estimated as less than $\pm 15\%$, but in one or two cases of extreme mixture ratio variation the error slightly

exceeded 50%.

As mentioned before, the thermocouple probe is placed so that it rests just inside the edge of the spray during the initialization (i.e. until injector temperatures become steady) and does not go outside the spray during any flow. The technique was employed to avoid the larger errors that would have resulted from the delayed response if the probe had moved outside the spray to inside it or vice-versa.

One technique which could have alleviated the error due to delayed response would have been to drastically cut down the thermocouple probe speed (about $\frac{1}{4}$ inch/second in our tests). Unfortunately, this was not feasible because had this been done there would have been insufficient propellants to insure a complete run. (The greater part of the propellant consumption is involved in initializing.) In the future it will be possible to take measurements from all thermocouples at once, eliminating three traverses of the probe rake, and thus allowing slower probe speeds to be employed.

Error also arose in determining the position at which the mixture ratio is taken. Errors arising due to the helipotter method of determining position are no more than $\pm .05$ inches. However, there are also errors due to alignment in setting up the thermocouple rake or the collector apparatus before each run which may reach $\pm .1$ inches.

One error in mixture ratio determination that might also be expected would result from air from outside the spray circulating into the spray and influencing the temperature measurements. This problem was encountered in individual doublet spray tests without chamber wall confinement. However, if this were the case in these tests, mixture ratio readings near the edge of the chamber would be expected to show greater disagreement with collector readings than those in the center of the chamber. This effect was not observed.

One must also consider the accuracy of the Bristol charts, retransmitting slide wires, and computer operations. This includes error due to interpolation of data points from the three flows (fuel, oxidizer, and mixture) since the positions of the data points measured (from the computer output) during the three flows do not coincide exactly. Inaccuracy in mixture ratio due to this factor was less than $\pm 3\%$.

It is interesting to compare the accuracy attained by having the data punched up directly on the IBM 1620 Computer with the accuracy that would have been attained by reading and recording the data points off the Bristol charts. One run was reduced by both methods in order to obtain a measure of this. Coming directly into the computer is definitely the more accurate of the two methods. The major discrepancy between the two methods turns out to be in determining position, rather than mixture ratio, since correlating the position readings from the chart with the thermocouple readings (on different charts) was an error-prone procedure. Position measurements by the two methods agreed within $\pm .1$ inch and mixture ratio readings within $\pm 2\%$. Coming directly into the computer resulted in mixture ratio/position profiles that had a smoother appearance than by the other method.

Results and Conclusions

The experimental findings of this research are summarized in Figures 3 - 4. Figure 3 shows the mixture ratio variation for the Type II, 4 x 4 injector at the three axial stations, while Figure 4 show the results at the three axial distances for the Type IV, 4 x 4 and Type IV, 6 x 6 injectors placed side by side.

Basic Assumptions of Model

1. The differences in mixture ratio distribution between cold flow tests and hot firings with the same injector and propellant flow rates is negligible, especially near the injector face.
2. There is no interaction among the various sprays from the different elements.
3. Chamber walls have an effect upon mixture ratio distribution by reflecting mass from the walls (important for small engines).
4. All oxidizer elements (they all have like geometry) have the same mass distributions. This applies also to all fuel elements.
5. The mass distribution resulting from a single row of either fuel

elements or oxidizer elements along a line perpendicular to the said row and parallel to the injector face is symmetric with respect to this row.

Discussion of Model

The method used in applying the proposed model is straightforward. The first step is to make use of assumptions 2, 4, and 5 to set up mass distribution profiles along the thermocouple path due to each fuel and oxidizer row separately. Then the mass distributions due to the fuel rows are added together, as well as the mass distributions due to the oxidizer rows. Finally, to each of these sums the effect of mass reflected off the chamber walls (assumption 3) is added in so that the total mass distribution along the thermocouple path due to each propellant is now known. From this the theoretical mixture ratio along the thermocouple path is found. By a judicious choice of the magnitude of the key (a, σ) one tries to obtain theoretical results that agree well with the experimental findings.

The above description leaves two questions unanswered. They are: 1) What shape shall be chosen for the mass profiles due to each fuel and oxidizer row separately? and 2) How can the mass reflected off the chamber walls be accounted for quantitatively in the model? The author chose solutions to each of these questions which seemed to be the most plausible available. The approximate nature of the technique chosen to answer these two questions must be kept in mind. As it turns out, different methods than those chosen would have worked also. A discussion of how both of these questions were answered follows.

It is assumed that the mass profiles due to each fuel and oxidizer row separately could be represented by the formula $f(x) = \frac{a}{\sigma\sqrt{2\pi}} \exp\left\{-\frac{(x-\mu)^2}{2\sigma^2}\right\}$, where a , σ , and μ are constants. In the normalized form, the coefficient $a = 1$, and then we have the so-called "Gaussian" or "Normal" distribution. The mathematics of the Gaussian curve can be found in any textbook on statistics (e.g. Ref.22).

The Gaussian curve exhibits a characteristic bell shape and is symmetrical about the mean as is required by assumption 5. Studies made

earlier by the author with the collector on single fuel and oxidizer elements very similar to the ones employed in these investigations indicated that the mass profile along any line parallel to the injector face could be fitted by a Gaussian Distribution quite well. It is thought that the Gaussian curve could also be applied approximately to rows of fuel and oxidizer elements as has been done in the proposed model. It turns out that one can manipulate the shape of a Gaussian curve quite easily to fit the needs of the model by changing the standard deviation (i.e. σ) in the preceding formula.

The problem of accounting for the mass reflected off the chamber walls is complicated because one cannot assume that this mass rebounds elastically. The spray hits the wall in the form of tiny droplets which will be deformed and may break up upon contact with the wall. Some of the fluid may in fact run along the wall and not be reflected at all. Thus, accounting for where the mass hitting the wall goes becomes an exceedingly complex problem.

For the purposes of the proposed model it was assumed that the "coefficient of restitution" for impact of mass in a direction normal to the walls is 0.5. This is equivalent to saying that the mass which hits the chamber wall rebounds with a velocity (normal component) equal to half its incoming velocity (normal component). A discussion of the coefficient of restitution (defined for inelastic collisions) may be found in certain physics or dynamics textbooks (e.g. Ref.23). Although one would expect the coefficient of restitution to vary greatly (between 0 and 1) for the reflected mass, it is thought that assuming an average value might yield a fair approximation. Differences caused because the chamber length does not extend the entire distance to the sampling plane are neglected in finding reflected mass.

It was found that the above model could indeed be applied (in a trial and error fashion) to produce mixture ratio variations close to those observed. Figures 5 and 6 illustrate how this model has been applied to thermocouple number three at the three inch and seven inch axial stations for the Type II, 4 x 4 injector. Figures 7 and 8 illustrate how this model has been applied at the three inch axial station

to the Type IV, 4 x 4 injector and the Type IV, 6 x 6 injector respectively for thermocouple number three. The scale for mass flux in these figures was chosen arbitrarily. A slight displacement correction has been applied to the experimental findings in Figures 7 and 8 where careful analysis of the data indicates that the thermocouple probe rake was misaligned to the injector.

Indeed, the proposed model is flexible enough that mass distribution curves other than those which were chosen could have been employed to fit the data equally well. For instance, other Gaussian curves but with different standard deviations (σ) and which were multiplied by different constant coefficients (a) would have worked within a relatively narrow range of values. In this fashion one can also manipulate the ratio of the area under the oxidizer mass distributions to the area under the fuel mass distributions without destroying agreement with experimental findings. It is also evident that the assumptions made regarding the shape of the mass profiles and the distribution of the mass reflected off the walls, however correct or incorrect they might be, could have been replaced by other schemes that would have worked.

In the next section it will be seen how the proposed model can be used to deal with the many factors involved and to explain many of the observed characteristics of the three injectors.

Wall Effects and Injector Differences

In the first place it is interesting to note how necessary it is to include the effect of mass reflected off the chamber walls into our calculations of theoretical mixture ratio. The reason is as follows. Consider for the moment Figures 5 - 7 in which the theoretical mixture ratio distribution for the two 4 x 4 element array injectors is found. Comparing the theoretical mixture ratios at the positions where the two oxidizer rows are located reveals that the theoretical mixture ratio at the second oxidizer row (going from left to right in Figures 5 - 7) must be no more than twice the mixture ratio at the first oxidizer row if wall mass reflection is not taken into account. This is because at the positions of the two oxidizer rows the oxidizer theoretical mass flux

readings are the same (assumption 4) but the fuel mass flux at the first oxidizer row can be no more than twice the fuel mass flux at the second oxidizer row (from assumption 4 and summing principles).

Similar reasoning places other bounds on the problem if wall mass reflection effects are not taken into account. For instance, for the 6 x 6 element array injector the theoretical mixture ratio without wall reflection at the position of the third oxidizer row (going from left to right in Figure 8) can be no more than twice the theoretical mixture ratio at the positions of the first two oxidizer rows. Rather than linger on this point for too long, it is suffice to say that without taking into account the effect of mass reflected off the chamber walls good agreement between theoretical mixture ratio variation and experimental findings would have been impossible in the wall region. This argument helps to support assumption 3 which was made.

As the axial distance from each of the three injectors is increased, the observed variation in mixture ratio becomes less severe. This observation is correctly predicted by the proposed model, because as we increase the axial distance one would expect the bell-shaped mass distribution due to each row to become wider and flatter (which corresponds to increasing σ in the formula for the Gaussian Distribution). The model predicts that mixture ratio variation levels off as the bell-shaped distributions become wider (compare Figures 5 and 6).

The major differences between the mixture ratio variation of the Type II, 4 x 4 injector and the Type IV, 4 x 4 injector can be explained in light of the proposed model. Consider Figures 9a and 9b which show these two injectors. One would expect the shape of the mass distributions along a thermocouple path due to separate fuel and oxidizer rows to be wider for the Type II injector, since in this injector the thermocouple paths along the major axis of the elliptical mass distributions due to each element, while in the Type IV injector the thermocouple paths are at an angle to the elliptical mass distributions. The proposed model would take this effect into account by predicting less severe mixture ratio variation for the Type II, 4 x 4 injector than for the Type IV, 4 x 4 injector. This in fact is supported strongly by the experimental

findings (compare Figure 3 with Figure 4)

Another experimental finding is that the mixture ratio variation along the thermocouple paths for the Type IV injectors tends to be more severe toward the center of the injector, which is especially evident at the 3-inch axial station (see Figure 4). This observation can be at least partially explained by the proposed model in the following way. Referring to Figure 9b, one would expect the bell-shaped distribution due to each fuel row and oxidizer row separately to become wider near the walls parallel to the thermocouple paths since the mass distribution (in the direction of the thermocouple paths) of the elements nearest these walls would widen upon reflection. According to the proposed model the mixture ratio variation should become smoother as this happens. For the Type II injector, on the other hand, one would expect much less reflection from the walls parallel to the thermocouple paths. This would help to explain why the effect of more severe mixture ratio variation toward the center is not observed in this injector.

Suggested Method of Predicting Mixture Ratio

In this last section it will be shown how the model proposed in this paper might be modified and extended in order to solve the more complex problem of predicting mixture ratio variation for a given injector. Such a method of predicting mixture ratio variation would be based on assumptions 1, 2, and 3 listed previously, and would proceed as follows.

First, a detailed mass survey using a collector device would have to be taken (at the proper flow rate) for each fuel and oxidizer element of the injector which has a different geometry. If an element is of the like-on-unlike variety, we would also need mixture ratio information. Note that it would appear to be necessary to take surveys of these single elements at only one axial station. This is possible because it can be shown (Ref. 24) that the flow rate along a radial line from the point of impingement of a spray is given by $G_1 = G_0(L_0/L_1)^2$ where G_0 and G_1 are the local mass fluxes on the given line corresponding to the distances L_0 and L_1 respectively. Thus if the mass distribution in one plane due to the element is known it can be found for any other plane, however, in the confined space available in the rocket motor tested

these regions overlap.

Second, a method of accounting accurately for the distribution of the mass flux reflected from the walls would have to be developed. This is very essential to the problem for small rocket motors as the investigations described in this paper show.

Lastly, the mass distributions of each element, along with its position and orientation would be plugged into a computer program. The mass distributions would then be superimposed and wall reflections taken into account by the computer program. Theoretical mixture ratio distributions could then be calculated.

It is evident that if this method of predicting mixture ratio is to work, many details must be ironed out in the future. The problem is obviously not a simple one especially when combustion effects are present in an actual firing.

D. DROPLET POPULATION DENSITY INVESTIGATION

A possible source of energy for buzz-type instability, i.e., injection-coupled phenomenon, is the grouping of the injected droplets into high and low density clumps. Viewed from the combustion "zone" these variations are akin to mass fluctuations even though the feed system might be supplying a constant mass flow.

The preliminary results of the study of variations in droplet population densities in impinging jet sprays were reported in last year's progress report.¹ The cold flow study of this phenomenon is now finished and is more completely outlined in a MSE thesis to be released shortly as a technical report.¹⁷ In the past year, additional variables have been investigated with the primary emphasis being placed upon the separation of the liquid properties of viscosity and surface tension; until recently these properties were combined into one dimensionless parameter. In addition to the actual parametric studies an attempt was made at improving the existing data recording and reduction techniques.

The experimental investigation of the droplet population density variation involved the following parameters: breakup frequency, chamber pressure, injection velocity (Δp), injector diameter (proportional to drop size), and the fluid properties, density, viscosity and surface tension. Also included in the dimensional analysis (described later) is the gas viscosity, although this parameter was not varied in this cold flow study. As reported last year, the ratio of the number of droplets in the wave maximum to that in the wave minimum was also measured. This was done as a check for the existence and magnitude of possible resonance effects. The primary test procedure was to fix all of the variables except chamber pressure, and to then make a series of four runs at various pressures. After data reduction of the streak film, a curve of breakup frequency vs. chamber pressure was obtained for the various test conditions. The previously reported results¹ were obtained with only two fluids, water and 50% water-50% methyl alcohol. The resulting data did not allow the fluid properties to be separated so further tests were run with a surface tension reducing agent added to water. This allowed the surface tension to be significantly varied while maintaining viscosity and density constant. Tests

were also conducted with 100% methyl alcohol to more closely simulate the actual rocket motors.

From the resulting data an empirical relation was obtained using nondimensionalized analysis. This approach was as follows:

assuming that frequency = $f = f(P_c, D_I, V_I, \rho_I, \mu_I, \sigma_I, \mu_g)$

$$\text{OR } f = A (D_I^a \rho_I^b V_I^c \sigma_I^d \mu_I^e P_c^f \mu_g^g)$$

now considering dimensions
$$\frac{1}{T} = L^a \frac{M^b}{L^{3b}} \frac{L^c}{T^c} \frac{M^d}{L^2 d} \frac{M^e}{L^2 T^e} \frac{M^f}{L^f T^{2f}} \frac{M^g}{L^3 T^g}$$

and balancing dimensions

$$M: 0 = b + d + e + f + g$$

$$L: 0 = a + 3b + c - e - f - g$$

$$T: -1 = -c - 2d - e - 2f - g$$

$$\text{OR } a = -(1 + d + e + g)$$

$$b = -(d + e + f + g)$$

$$c = 1 - 2d - e - 2f$$

thus
$$f = A \frac{V_I}{D_I} \left(\frac{\sigma_I}{D_I \rho_I V_I^2} \right)^{c_1} \left(\frac{\mu_I}{D_I \rho_I V_I} \right)^{c_2} \left(\frac{\rho_I V_I^2}{P_c} \right)^{c_3} \left(\frac{\mu_g}{\mu_I} \right)^{c_4}$$

or
$$\frac{f D_I}{V_I} = A \left(\frac{\sigma_I}{D_I \rho_I V_I^2} \right)^{c_1} \left(\frac{\mu_I}{D_I \rho_I V_I} \right)^{c_2} \left(\frac{\rho_I V_I^2}{P_c} \right)^{c_3} \left(\frac{\mu_g}{\mu_I} \right)^{c_4}$$

From the test data one can now obtain the exponents. These in fact are: $c_1 = -.25$, $c_2 = 3.25$, $c_3 = .8$, and $c_4 = 2.9$. From the resulting final empirical plot (Figure 10) one also gets the empirical constant ($A = 2 \times 10^{16}$). Thus the final cold flow empirical result is:

$$\frac{f D_L}{\nu_L} = 2 \times 10^{16} \left(\frac{\sigma_L}{D_L \rho_L \nu_L^2} \right)^{-.25} \left(\frac{\mu_L}{D_L \rho_L \nu_L} \right)^{3.25} \left(\frac{\rho_L \nu_L^2}{P_L} \right)^{.8} \left(\frac{\mu_L}{\rho_L} \right)^{2.9}$$

Also seen in Figure 10 is a curve resulting from the data obtained from transverse rocket tests exhibiting intermediate frequency pressure oscillations. As can be seen, this curve has a constant of $A = 7.0 \times 10^{10}$. It is believed that this difference in the empirical constants can be attributed to the inability to include the gas viscosity directly in the analysis, except in conjunction with the liquid viscosity.* The large increase in gas viscosity (about two orders of magnitude) in the rocket motor seems to account for the large change in the empirical constant. Thus, we see that this experimental evidence seems to support the hypothesis that the droplet breakup phenomenon does affect intermediate frequency combustion instability.

It should also be noted that no effects were found to indicate any enhancement of the natural breakup phenomenon by operating the chamber under oscillation conditions. However, it is felt that the low amplitude oscillations induced by the siren (peak-to-peak amplitude approximately 10% of steady-state pressure) and the lack of sensitivity of the streak technique for such measurements tend to make inappropriate any conclusion concerning the possibility of resonance effects.

To further investigate resonance effects and to reduce the effect required to obtain and reduce data, various electro-optical techniques were investigated. These included the direct use of photocells and photo-transistors to "look" into the chamber and the indirect use to reduce the streak film. However, after several attempts to obtain a workable system these techniques were abandoned in favor of the previous approach. This was necessary in order to insure that all data was reduced within a reasonable time, since it appeared that significant sophistication and hence

* This parameter could not be significantly varied in the cold flow experimental apparatus since most gases have similar viscosities at room temperature.

further development time was required in the case of electro-optical techniques before obtaining a working system.

Returning to the rocket motor tests displaying intermediate frequency pressure oscillations, several interesting features are evident in the pressure traces (Figure 11). These include phase relationships between transducers separated by 90° and phase relationship between the maximum and minimum envelopes of any one transducer. Such effects are not readily explainable since acoustic propagation should be found for any pressure variation and hence such phase differences should be associated with much higher frequencies.

E. VAPOR DISPLACEMENT AND STREAM BREAKUP EXPERIMENTS

Another energy source within the rocket motor is the coupling of the pressure oscillations via associated vapor displacement with the resulting changes in the instantaneous burning rate. Referred to as the "vapor displacement mechanism" this coupling is important in the case of transverse mode instability. Over the past few years experiments on pseudo rocket hardware have sought to add quantitative data to the qualitative evidence of the importance of this mechanism.¹⁻³ A recent technical report²⁵ covers one portion of this investigation in detail. In that report experiments performed to investigate the breakup of a vaporizing liquid Freon jet are described. Behavior of the jet has been studied under a variety of steady and oscillatory pressures.

It has been observed that chamber pressure in the pseudo rocket has no significant effect on jet length in the laminar regime so long as the fluid is not rapidly evaporating. For the fluid whose vaporization rate is substantial, a decrease in chamber pressure and the subsequent increase in vaporization, leads to a slight decrease in jet length. This effect becomes more pronounced the larger the jet diameter. In the turbulent region the effect of pressure depends on the fluid under observation, the jet velocity and jet diameter. For a very slowly evaporating fluid, chamber pressure always accelerates jet breakup. This can be attributed to the increased effect of air friction. The length of a vaporizing Freon jet, however, sometimes decreases with chamber pressure and under other circumstances increases. Generally, the evaporation process becomes more

important than air friction in controlling jet length when the jet diameter is large and the jet velocity is high.

When the gas in the chamber is subjected to acoustic oscillations, jet breakup is generally enhanced regardless of whether the fluid is rapidly evaporating or not. The effect, however, is only measurable in the laminar regime for the range of oscillation amplitudes employed. At low steady-state chamber pressures, oscillatory pressure (standing mode at a pressure antinode) and oscillatory velocity are both about as effective in promoting the breakup of a non-evaporating fluid. At higher steady pressure levels, pressure oscillations (standing mode at a pressure antinode compared to the spinning mode) appear to be more effective than velocity oscillations. The behavior of a vaporizing fluid is essentially the same as a non-vaporizing fluid except that velocity oscillations become as effective in promoting breakup as pressure oscillations at high chamber pressure. As chamber pressure is lowered and vaporization rates increase, velocity oscillations become more effective than pressure oscillations.

Under none of the circumstances encountered in the pseudo rocket experiment did the spinning mode enhance jet breakup to a greater extent than the standing mode.

Viewing the results of droplet spray fan mixing in a hot rocket environment, tangential displacements resulting from velocity variations were observed. A sodium seeded jet was used as a tracer and indicated no detectable unidirectional motion within the range of the test conditions.

Very recent experiments have concentrated on separating the injected Freon jet into droplets via vibrations of the hypodermic tube injector. It was found that uniform, well-spaced droplet streams could only be formed from specially vibrated laminar jets. Thus we were concerned with low velocity, low Reynolds number flow. Through extensive experimentation it was found that droplet stream stability required relatively high, yet still laminar, velocity; large hypodermic diameter; and high vibration frequency. This stability is essential in that photographs of an established stream in the various chamber modes must show droplets in approximately the same position if there are to be definite picture comparisons. Also, streams without good stability are very often destroyed by the violent pressure and velocity oscillations that are studied. Since once the stream was established

it could not very easily be checked until after the entire run, much time was wasted in taking and developing pictures which had already been destroyed.

In the present study the major interest was in obtaining maximum droplet separation (so as to be able to distinguish individual vapor sheaths in shadowgraph pictures). This requirement made very low jet velocity, and low generator frequency necessary. Clearly then there was a compromise between separation and stability; and experimental procedure here became a matter of sensitive touch, patience, and often a good deal of luck. Figure 12 shows such preliminary data.

With the Strobotac placed on the spark source side of the chamber, a laminar jet of about one-half inch is established. A chamber pressure of at least 20 psig was necessary when Freon 114 was used to keep this liquid from vaporizing instantly. Laminar flow was easily seen as a straight-line jet free of perturbations. With its amplifier turned up to full volume, the audio generator was turned on and a stable droplet was established at about 100 cps and the drops were made visible and stationary by adjusting the Strobotac in its low frequency range. From this point both the generator and stroboscope frequency were continuously dialed down until a stable stream could no longer be maintained. During this slow-down process the jet velocity also had to be cut back. Once the optimum separation point was reached the generator frequency was raised slightly to insure stability throughout the following run.

Placement of the neoprene feed tube was crucial - as much of the tube as possible had to be suspended so as to feed freely and vertically into the hypodermic. If the tube hung from the generator its weight created a sideways force which disrupted uniform flow sending droplets in more than one direction in a spray.

Many low-frequency streams required the full power of the 40-watt home-made amplifier and care was taken not to overheat the hypodermic voice coil.

The tentative findings of this study is that droplets are more rapidly vaporized in velocity as opposed to pressure oscillating fields.

IV. DAMPING DEVICES

A. THEORETICAL STUDIES OF FLOW BEHAVIOR WITH ACOUSTIC LINERS

One of the essential goals of the study of acoustic liners is to determine the optimum cavity design for a chamber oscillation of a particular frequency or range of frequencies. For small amplitude oscillations the cavity resonant frequency is determined by the Helmholtz resonator formula, but for larger amplitudes there may be a significant deviation from this value. One of the purposes of this analysis is to try to determine the extent of this deviation.

The main dissipation mechanism under consideration in an acoustic liner is the loss of kinetic energy of the gas jets as they leave the orifices. This kinetic energy is converted into turbulence of the gas in the chamber or the cavity, and hence no longer contributes to the energy of the oscillating wave. This mechanism is nonlinear because it involves the square of the velocity. The equations describing the process are not solvable analytically and one resorts to other techniques. In this analysis the equations contained several parameters, and solutions for particular values of these parameters were found by numerical integration on the 7094 computer.

The known quantity here is taken to be the chamber pressure as a function of time and the desired results are the orifice velocity and cavity pressure oscillations.

Two sets of equations have been developed, making a different assumption about the flow in the orifice in each case. Based on the second order analysis of Sirignano¹ the assumption was made that the velocity is constant along the length of the orifice at any instant of time. A second case was run for comparison in which the assumption was that the mass flux is constant along the orifice at any instant of time.

The model used to develop the equations is isentropic flow in both directions through the orifice but with different mean gas temperature in the chamber and in the cavity. Thus we assume the cavity gas maintains the relationship $\rho^\gamma = C$ where C is a constant in time. The chamber gas is also assumed to follow this relationship but with a different value of the constant.

In both cases the variables were non-dimensionalized with respect to the mean chamber conditions. The velocity direction convention can be seen from Figure 13.

It is also assumed that the acceleration of the gas to the velocity u at the entrance of the orifice occurs in a very short distance and with no lag in time. Thus, the pressure at the orifice entrance may be expressed as

$$P_{1,2} = P_{2,2} (1 - w_{1,2}^2)^{\frac{\gamma}{\gamma-1}}$$

where the choice of subscripts will depend on the flow direction and where

$$w_1 = \frac{u_1}{\sqrt{2 C_p T_x}}$$

w_2 may written in identical form.

In the first case we assume velocity constant along the orifice length and a linear density variation, hence at any instant of time, $u = \text{const}$ and $\rho = b_1 + b_2 x$ where x is axial distance along the orifice and b_1 and b_2 are constants.

Under these restrictions, the one-dimensional, integrated momentum equation, applied to the orifice as a control volume gives us the following result for positive flow,

$$\frac{du}{dt} = \frac{2}{\gamma} \frac{[P_2(1-w_{1,2}^2)^{\frac{\gamma}{\gamma-1}} - P_2]}{[P_2^{\frac{1}{\gamma}}(1-w_{1,2}^2)^{\frac{1}{\gamma-1}} + P_2^{\frac{1}{\gamma}}]}$$

where

$$w_1 = \frac{u}{\left(\frac{2}{\gamma-1}\right)^{\frac{1}{2}} P_2^{\frac{\gamma-1}{2\gamma}}}$$

and the continuity equation applied to the cavity yields,

$$\frac{dP_I}{dt} = \gamma \alpha \beta \alpha^{\frac{1}{\gamma}} P_I$$

Similarly for negative flow, we obtain

$$\frac{dU}{dt} = \frac{2}{\gamma} \alpha^{\frac{1}{\gamma}} \frac{[P_I - P_{II}(1-w_2^2)^{\frac{\gamma}{\gamma-1}}]}{[P_I^{\frac{1}{\gamma}} + P_{II}^{\frac{1}{\gamma}}(1-w_2^2)^{\frac{1}{\gamma-1}}]}$$

where

$$w_2 = \frac{U}{\left(\frac{2}{\gamma-1}\right)^{\frac{1}{2}} P_{II}^{\frac{\gamma-1}{2\gamma}} \alpha^{\frac{1}{\gamma}}}$$

and

$$\frac{dP_{II}}{dt} = \gamma \beta \alpha P_{II}(1-w_2^2)^{\frac{1}{\gamma-1}}$$

In the above, $\alpha = C_{II}/C_I$ and $\beta = A\ell/V$. Also, pressures are non-dimensionalized with respect to p_0 , the mean chamber pressure, orifice velocity with respect to a_0 , the mean speed of sound, and time with respect to ℓ/a_0 .

It must be noted that as a consequence of the assumptions these equations do not match together at zero velocity, that is

$$\lim_{u \rightarrow 0^+} \frac{dU}{dt} = \frac{1}{\alpha^{\frac{1}{\gamma}}} \left[\lim_{u \rightarrow 0^-} \frac{dU}{dt} \right]$$

In the second case, the assumption was that the mass flux is constant along the length of the orifice. With this assumption, the momentum equation gives, for positive flow

$$\frac{dm}{dt} = \gamma \left[P_{II}(1-w_1^2)^{\frac{\gamma}{\gamma-1}} K_1 - P_{II} \right]$$

where

$$K_1 = 1 - \frac{2\gamma}{\gamma-1} \frac{W_1^2}{1-W_1^2} \left[\left(\frac{P_2}{P_1} \right)^{\frac{1}{\gamma}} (1-W_1^2)^{\frac{1}{\gamma-1}} - 1 \right]$$

And continuity for the cavity results in,

$$\frac{dP_2}{dt} = \gamma \alpha^{\frac{1}{\gamma}} \rho m P_2^{\frac{\gamma-1}{\gamma}}$$

While for negative flow,

$$\frac{dm}{dt} = \gamma \left[P_1 - P_2 (1-W_2^2)^{\frac{\gamma}{\gamma-1}} K_2 \right]$$

where

$$K_2 = 1 - \frac{2\gamma}{\gamma-1} \frac{W_2^2}{1-W_2^2} \left[\left(\frac{P_2}{P_1} \right)^{\frac{1}{\gamma}} (1-W_2^2)^{\frac{1}{\gamma-1}} - 1 \right]$$

and

$$\frac{dP_2}{dt} = \gamma \alpha^{\frac{1}{\gamma}} \rho m P_2^{\frac{\gamma-1}{\gamma}}$$

The values of w_1 and w_2 must be determined from the following equations,

$$(1-W_1^2)^{\frac{1}{\gamma-1}} W_1 = \frac{m}{\left(\frac{2}{\gamma-1} \right)^{\frac{1}{2}} P_1^{\frac{\gamma+1}{2\gamma}}}$$

and

$$(1-W_2^2)^{\frac{1}{\gamma-1}} W_2 = \frac{m}{\left(\frac{2}{\gamma-1} \right)^{\frac{1}{2}} P_2^{\frac{\gamma+1}{2\gamma}}}$$

In the above equations, m is nondimensionalized by $\rho_0 a_0$. These last equations must be solved using an iteration scheme for particular

values of m and p_I or p_{II} .

In the second case the equations are not discontinuous at zero velocity.

We have neglected such effects as flow separation at the entrance to the orifice, nonzero velocity in the chamber and temperature changes in the cavity. Further study will have to determine the actual magnitude of these effects, but it is hoped that this analysis will be a useful first approximation to such a complex problem.

The scheme chosen for integrating the equations is a form of the Milne variable-interval technique. This technique was chosen because it allows a smaller interval to be used where it is needed, without taking as much computer time as a Runge-Kutta scheme for that same interval size. Also there was a well tested program available at the Guggenheim Computing Center which utilized this technique.

Even with the equations in nondimensionalized form there are many parameters which must be chosen before a solution can be obtained. These involve the particular form of the input (chamber) pressure, the geometry of the cavity-orifice combination, and the ratio of the isentropic constants in the cavity and the chamber.

The programs are presently arranged to take an input pressure expressed as a Fourier series, but it would be relatively easy to substitute some other functional form. Also, the programs were run only for a value of the ratio of specific heats (γ) of 1.2 but it would be a simple matter to change to some other value.

It was decided that the most convenient form of output would be in the form of Fourier components, both since it is compact (yet definitive) as well as the fact that one of the ultimate uses of these programs will be to calculate values of admittance coefficients for an acoustic cavity. The admittance coefficient is determined by the ratio of the complex velocity at the entrance to the complex chamber pressure, where the real parts of the velocity and pressure are the first harmonic components expressed as a cosine with a phase angle.

A check was made to assure that there was no mean mass flow in either direction (this would be inconsistent with our analysis) and it was found the mean flow in each case was less than one-half of one percent of the

first harmonic mass flow component, which was considered within the range of numerical accuracy.

In order to have a constant reference for the frequency, it has been expressed as a ratio of the actual nondimensional frequency to the Helmholtz resonant frequency. We find that,

$$f_{res} = \frac{1}{2\pi} (\alpha^{\frac{1}{2}} \beta)^{\frac{1}{2}}$$

Here, f_{res} is nondimensionalized with respect to a_0/ℓ . So in the data a frequency of 1.0 corresponds to the Helmholtz resonant frequency.

All of the values of orifice velocity and pressure amplitude are first harmonic values. The chamber pressure wave consisted of a constant (of value 1 because of the nondimensionalization) plus a first harmonic term only. As this work progresses further, it is intended to investigate the effect of higher harmonic terms in order to more closely approximate actual chamber waves.

The range of interest of the parameter β is quite large, for we see that the resonant frequency of the cavity-orifice combination from the Helmholtz formula is,

$$f_{res} = \frac{a}{2\pi} \left(\frac{A}{\ell V} \right)^{\frac{1}{2}} = \frac{a}{2\pi \ell} (\beta)^{\frac{1}{2}}$$

where a is the cavity sound speed. Since the resonant frequency desired for a wide range of rocket chambers varies over about two orders of magnitude and possible orifice lengths vary over about one order of magnitude, the value of β could vary over as much as six orders. Due to reasonable limitations on computer time we were able to study only two values of β . These two values were 0.1 and 0.01. It can be seen from Figures 14 to 21 at the lower value of β the pressure amplitudes are much lower. This seems reasonable in view of the fact that for a given orifice length and orifice area, decreasing β amounts to increasing the size of the cavity which would naturally result in lower cavity pressure amplitudes. Also, for the lower value of β , the velocity amplitude becomes less sensitive to frequency variations, at least up to 1.2 times the Helmholtz resonant

frequency. This would seem to follow from the fact that the velocity derivative is proportional to the pressure difference across the orifice and as the cavity amplitude decreases this difference is less affected by phase differences. Hence ultimately the velocity amplitude varies less.

The parameter α is determined mainly by the ratio of the temperatures in the cavity and the chamber. With a little manipulation we can see that, taking mean conditions in the cavity and the chamber,

$$\alpha = \left(\frac{p_0}{p_*} \right)^{\gamma-1} \left(\frac{m_* T_*}{m_0 T_0} \right)^{\gamma}$$

where the subscript * refers to a mean cavity condition, and m stands for the molecular weight of the gas. Since we have no idea of what the value of p_0/p_* should be, we cannot pick both it and the value of T_*/T_0 . We are fortunate then that for $\gamma = 1.2$ this ratio occurs to the 1/5 power in α . So, assuming it to be close to 1, we calculate from the following,

$$\alpha = \left(\frac{m_* T_*}{m_0 T_0} \right)^{\gamma}$$

As a check on this assumption it was found from the integration that the value of p_0/p_* was generally in the range 0.95 to 1.05, which indicates that we have an error on the order of 1%.

The programs were run for three values of the parameter α . The value $\alpha = 1.0$ gives the case in which both chamber and cavity are at the same temperature. In this situation the Helmholtz formula should be most accurate and this is indeed seen (for low amplitudes) in Figure 14. The value $\alpha = 0.15$ corresponds approximately to the case of a "hot" cavity into which hot chamber gases have been pumped. Finally, the value $\alpha = 0.05$ simulates the "cold" condition in the cavity, which is normally the situation when instability begins.

It appears that as the value of α is reduced from 1.0 the pressure peak moves down in frequency and also the velocity reaches higher values at low frequencies of the order of 0.2 times the resonant frequency.

The nonlinearity of the problem under consideration is very evident from the data. We could reasonably expect if the problem were linear that we would have maximum cavity pressure amplitude, maximum velocity amplitude, and 90 degree phase lag of the cavity pressure related to the chamber pressure at the point corresponding to the natural frequency of oscillation of the orifice-cavity combination. However, the situation in this case is not quite so simple. While the velocity amplitude seems to peak right near the Helmholtz natural frequency, the pressure peak is strongly affected by the value of the parameters α and ϑ . In addition, the cavity pressure peak is shifted by an increase in amplitude of the chamber pressure wave.

As far as the two different cases are concerned, they show the same general trends but the amplitudes of the velocity and pressure responses differ in most cases. For example, in the velocity response for Case 1 the velocity amplitudes around the resonant frequency decrease with decreasing α , whereas in Case 2 the amplitudes remain very nearly constant.

Further points will have to be taken to determine if there is an optimum value of ϑ or if the trends shown with the two taken in this analysis continue throughout the range of interest. It may also be important to determine which case is giving valid results, if either, with regard to the velocity amplitude change with decreasing α . Since increasing α corresponds to increasing the cavity temperature, which would occur if hot chamber gases were being pumped into the cavity, an increase in velocity amplitude could mean an increase in damping capability in this situation.

NOMENCLATURE

A - orifice area

ℓ - orifice length

V - cavity volume

a - local sound speed

p - pressure

ρ - density

u - orifice velocity

m - orifice mass flux/unit area

C - isentropic pressure density constant ($-\frac{P}{\rho^{\gamma}} = C$)

M - molecular weight

Subscript I - condition in chamber

Subscript II - condition in cavity

Subscript 1 - condition at chamber end of orifice

Subscript 2 - condition at cavity end of orifice

Subscript 0 - mean chamber condition

Subscript * - mean cavity condition

B. EXPERIMENTAL LINER STUDIES

To supply further data for the liner models and to simulate the actual firing conditions experienced by an acoustic liner, an experimental program has been initiated. The background data for these liner studies is the history of both linear and nonlinear high-frequency transverse mode combustion instability that has been documented over the past years at Princeton.¹⁻¹³ The rocket hardware is the 9-inch diameter, heat-sink chamber using either 12 or 16 spuds of like-on-like or unlike-type doublets arranged on a 7 or 8 inch injection diameter with thrust levels ranging from 1000 to 1333 lbs. Chamber pressures have been nominally set at 150 psia through the choice of nozzle throat size and flow rates. Pulsing is achieved through the use of tangentially oriented pulse guns. The propellants are LOX/Ethanol.

Key to the acoustic liner studies is the array of individually adjustable acoustic resonating cavities which are arranged circumferentially in three rows (axially spaced .75, 2.0 and 3.25 inches from the injector face) on a four-inch long section of the 9-inch diameter test hardware. The test configuration is shown in Figure 22. Based on the environment present within the cavities, the screw-type length adjustment is made to achieve the desired frequency of this Helmholtz resonator. Each of the individual cavities has six .1 inch diameter orifices, $\frac{1}{2}$ inch long. The acoustic cavity itself is nominally $\frac{3}{4}$ inch diameter and is capable of length changes from zero to two inches. The zero length condition makes the cavity inactive and hence it does not affect events in the chamber. This point has been checked (i.e., with all cavities at the zero length setting) and no noticeable change in the "triggered" first tangential mode oscillation amplitudes was observed.

Of considerable importance in the early tests, as well as in some preliminary tests with a single active cavity, were the temperature measurements which were made to better determine the cavity environment that fixes the cavity lengths required for proper resonant tuning. Following the temperature variations with .005 inch diameter W 5% Re and W 26% Re thermocouples, one finds that, even with stable operation, temperatures of 1300°F are reached momentarily following ignition and then the temperature

exponentially returns to a few hundred degrees above ambient. Initially, an unstable run behaves much the same way, however, rather than the exponential fall off the pumping action of the hot gases causes the temperatures to reach temperatures as high as 2300°F . Little variation was found between the conditions in the first row cavities versus third row cavities (.75 vs. 3.25 inches from the injector face).

Tests were initiated on the like-on-like doublet injector configuration consisting of 16 spuds with .059 inch orifice diameters spaced evenly on a 7-inch injection diameter.³ Previous tests indicated that this injector, chamber combination was nonlinearly unstable to tangential pulses. Table I illustrates this fact, noting that the oscillations initiated in the chamber by the pulse gun fell in the range of 226-236 psi pk-pk, while the resulting instability maintained a 200-250 psi pk-pk amplitude. The frequency was in the 2900-3000 Hz range and damping did not occur.

In the first tests, only three resonating cavities were activated. These were grouped in a 72° sector and were located in the first row (i.e., .75 inch from the injector face). The noticeable change with these cavities present was the approximately 40% reduction in instability amplitude.

Moving the three active cavities to a 120° circumferential spacing (i.e., related to the tip positions of the highly effective 3-bladed baffle designs - protection to the 3T mode) caused the resulting 1T mode instability to momentarily exist at 74-76 psi pk-pk amplitude and then damp in 170-285 seconds to combustion noise (c.n.). As in previous experiences with lower amplitude oscillations the frequency was depressed to 2720 Hz, a result of reduced gas mixing and a lower speed of sound near the injector.

Increasing the number of cavities at the 120° location to 3 at each point (in three different rows) the damp time was reduced to a narrow time band of 28-30 milliseconds. See Figure 23 for damping trend.

Further proof that the 3 @ 120° (.75") resonator cavity grouping was a marginal damper, was shown by tests at the 2 inch location. Here the amplitude stayed at the 78-97 psi pk-pk amplitude level and damping never occurred.

Reductions of damping times to the minimum value would have required tests with all 53 cavities tuned for the 2800 Hz range, i.e., the .375 inch cavity length. However, these tests were missed in the concurrent survey with the unlike doublets (the tests that will be described next). The prime reason for the concurrent program was the relative ease of changing injectors as contrasted to the time required to reset and pressure check the cavities when considerable numbers were used. However, data on a mixed group of cavity settings is shown in Table I. The .141 inch length was designed to suppress the 2T mode. Shorter damp times 12-22 millisec. were indicated in these tests as was expected.

The next series of tests were conducted on spontaneously unstable injector designs. Here the injector consisted of 12 unlike doublets with .082 inch orifices. The propellant choice was again LOX/Ethanol primarily to eliminate carbon logging of the acoustic cavity orifices as well as to minimize collection of fuel in the cavities and thus cause possible difficulties in subsequent firings.

The stability behavior of the unlike doublet injector design was that of spontaneous 1T spinning mode instability on every test. The final amplitude reached, as noted in Table II, was nominally 340 psi pk-pk. The frequency was 3150 to 3185 Hz, an increase over the most unstable like-on-like tests.

Because this injector design was spontaneously unstable and to minimize the danger to the water-cooled Dynisco transducers, due to the associated high heat transfer environment, the liner studies were initiated with nine cavities open at the 120° spacing which had proved to be dynamically stable for the like-on-like injector. In these tests the resultant 1T spinning mode amplitude averaged 275 psi pk-pk (a 20% decrease).

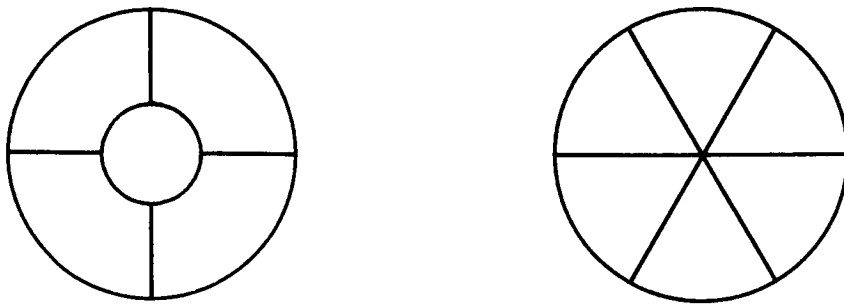
Seventeen* active cavities @ 120° produced similar results. Twenty-six* cavities produced noticeable amplitude reduction with several regions of distinctly different amplitudes being observed, a situation possibly attributed to the mixed mode behavior. With 52 active cavities tuned to the 1T mode frequency the mode within the chamber switched to the second

* Occasionally there were gaps in the orderly arrangement of the resonating cavities to allow for chamber pressure transducers and the pulse gun.

tangential and the amplitude was found to fluctuate between 50 and 150 psi pk-pk. In an attempt to eliminate both the 1T and 2T modes, 27 cavities were adjusted to resonate at the 2T mode and 26 at the 1T mode. Again spontaneous instability occurred, with 133 psi pk-pk amplitudes, this time returning to the 1T mode.

An attempt was made to tune the cavities for the 1T mode based on the "cold" cavity conditions associated with the start of a rocket firing. By coincidence this was the same cavity length required for the 2T mode. The instability again was spontaneous and amplitudes of 216-258 psi pk-pk were recorded. This test serves as an illustration of the effectiveness of cavity tuning although it was designed for another purpose.

Failing to reach dynamic stability with the liner capabilities associated with the 53 cavity configuration, two simple baffle designs were explored for instability suppression. Sketched below is a four-bladed baffle with hub and a six-bladed baffle. Both were two inches in length and fabricated from 1/8 inch thick copper.



Sketch Showing
Two Baffle Designs

The four-bladed baffle design experienced 2T mode oscillations of 190 psi pk-pk amplitude at 4650 Hz. With only two transducers @ 90° circumferential spacing it was not possible to differentiate whether this was a 2T standing or spinning mode, however, the location just downstream of the baffle tips suggests a 2T standing with the nodal lines fixed by the baffles. The six-bladed baffle limited the instability to primarily the 1T mode (evidence of higher modes, 2T, 3T, and combined modes 1T-1R are found in

the frequency analysis) with only 20 psi pk-pk oscillation amplitudes (@ only 2460 Hz).

This later approach was the most successful of those tried to suppress the spontaneous-type instability associated with this unlike doublet injector design.

Testing with the acoustic liner was resumed on the annular motor. This chamber design retained the 9-inch diameter chamber sections but added a 7-inch diameter center body, and replaced the conventional nozzle with a 24 multiple orifice design. The cylindrical length was increased to six inches (previously a 4-inch long chamber was used). The chamber Mach number at the point of nozzle entry was increased from .05 to .15. Chamber pressure was retained at the 150 psia level.

Although the annular chamber provided an opportunity to test the acoustic liner at reduced frequencies (1600 vs. 3000 Hz for the 1T mode), and with shock-type waves, the prime purpose for this hardware design was quite different. As outlined in Section B of Chapter V a theoretical model of combustion instability has recently been formulated by Professor Crocco which is based on an annular motor configuration and a simplified nozzle condition which can be represented by the multiple orifice design. The annular chamber will be used primarily in the experimental checkout of certain predictions of this theory.

From a combustion instability standpoint the annular chamber exhibited a noticeably different behavior than the conventional design. Elements that were dynamically stable in the conventional chamber (recessed like-on-like doublets with 40° impingement angles, again with .059 inch diameter orifices) were found to produce self-triggered instability in the annular motor. Nonlinearly unstable elements (the standard like-on-like doublet designs) were self-triggered into 1T standing mode instability in the annular chamber. The spontaneously unstable unlike doublets were not tested in this hardware.

Table III illustrates the stabilizing effect of the acoustic liner in the annular chamber with 53 and 26 cavities adjusted to a cavity length of 1.15 inches (i.e., the 1600 Hz range). Sources of popping, which are believed due to wall splashing and the presence of the centerbody causing local propellant accumulations, were present in the damped tests as well.

Summarizing the tests just described - it would appear that for this hardware and propellant combination (LOX/ALC) there are configurations which can be "triggered" into high frequency instability and such instability can also be suppressed with what are often relatively small increases in damping. Damp times were influenced by the number of active resonator cavities as shown in Figure 23. The placement of the damping was also shown to play a significant role. On the other hand, suppression of pressure oscillations in spontaneously unstable tests using unlike injector designs would appear to be a more difficult task. Amplitude decreases were found but stability could not be attained, at least within the limitations of the acoustic liner design tested. In those tests the tuning of the cavities switched the instability to another tangential mode rather than providing stability.

The nature of the energy distribution as measured from the radial variation in the pk-pk pressure oscillations was also investigated in the liner studies. Based on the unlike doublet tests one might conclude that the energy loss was primarily in the outer zone. Figure 24 illustrates this point. The instability prior to the addition of the liner was found to fit the theoretical distribution¹⁰ at the mid-radius location. Using the same injector, with the acoustic liner in place and all the cavities activated, the wall pk-pk pressure measurement was depressed 50% while the mid-radius point reading was lowered only 32%.

Complicating the picture, however, were the observations made with the like-on-like injector design, which provided wall pressure amplitudes close to the case just discussed. These tests also indicated a similar non-theoretical profile. Based on this later data it is difficult to interpret the results at this time.

The tests referred to here used a single Kistler 615 transducer in the two pressure measurement locations to eliminate any possibility of transducer error. Additional run to run monitoring was done with a Dynisco transducer located at the wall. Further testing of the radial energy profile is anticipated in the near future using the newly acquired tape recording system and employing Kistler 603A transducers.

Another experimental-analytic program, falling within the scope of the acoustic liner studies, involves the local phase conditions prevailing

between the chamber wall and the acoustic liner cavity. Using the model described in the previous section a brief survey was taken as to what values of phase might be anticipated under the conditions present in a typical rocket chamber. In an H shaped survey as shown in Figure 25 several important regions were investigated. First, the conditions representing the onset of instability (i.e., a cold resonator cavity) were surveyed over a range of amplitudes, to the point where orifice choking intervened ($M > 6$). A similar survey with fully-established instability (i.e., hot cavity) was also made with choking occurring at a higher value of ϵ . Linking these two surveys was the transient condition of rising cavity temperature. Moving from the cold to the hot cavity conditions would predict phase variations from 147° to 72° .

Although a number of preliminary rocket tests have already been performed to check these predictions it was felt that the data should be retaken using the new recording system prior to making final comparisons. Such tests are now in progress.

V. EXTENSIONS TO THE THEORY

A. SHOCK WAVE INSTABILITY IN THE AXIAL MODE

This topic is the subject of a Ph.D. dissertation that will soon be available as Technical Report 798.⁶ Consequently the complete analysis will not be presented in this yearly report, but rather a summary of the principal results of the work will be given.

In summary, the investigation has succeeded in developing an analytical method for predicting whether periodic finite amplitude axial oscillations may exist in a given liquid rocket combustion chamber if the combustion processes occurring there can be represented using Crocco's time-lag postulate. Both discontinuous (shock type) periodic waveforms and continuous periodic waveforms for the oscillations have been found. The dependence of the amplitude and the waveform of these periodic oscillations on n and τ , the combustion parameters, has been investigated. Two particular combustion distributions have been considered; the first being the limiting case of concentrated combustion, the second being the case where combustion is distributed throughout the chamber so that the steady-state velocity profile satisfies the equation $\frac{d\bar{u}}{dx} = 0(M_E)$. In general, it may be said that, in contrast to earlier expectations,^{5,8} the possibility of supporting both continuous and discontinuous finite amplitude pressure oscillations using a combustion model with a characteristic time that is of the order of the period of oscillation has been demonstrated.

Critical to the successful analysis of the problem was the selection of an expansion parameter proportional to, and of the same order as, the Mach number at the entrance to the supercritical nozzle. If a different expansion parameter, based on the difference between energy input and withdrawal from the chamber, was employed, it was found that discontinuous periodic oscillations could not be predicted when the combustion processes were represented by the time-lag model. It is to be noted that this latter kind of expansion parameter was used in all previous linear and nonlinear work which employed the time-lag postulate.

The Mach number at the entrance to the nozzle serves as a measure of

the total amount of combustion occurring in the chamber in the steady-state and also as a measure of the mean flow out of the nozzle under steady conditions. It can therefore be thought of as a measure of the deviation of the flow field in the chamber from a simple acoustic field with no mean flow. Picking the expansion parameter to be proportional to, and of the same order as, the Mach number in this analysis therefore caused the governing partial differential equations for the flow field to take the form of simple acoustic equations to lowest order. No energy or mass addition needed to be considered to this lowest order. The combustion (driving) terms and the nozzle (damping) term appeared only in the second order equations and boundary conditions. Because of this, standard techniques could be employed in order to relate the first order thermodynamic and gasdynamic dependent variables to an arbitrary function of order M (M is the Mach number). Application of the solid wall boundary conditions then showed that this first order function was periodic with period equal to the acoustic period for the fundamental mode of oscillation. A second order analysis then had to be pursued in order to find the form that the arbitrary first order function must take. The second order nozzle and combustion terms were found to appear only in the boundary conditions (concentrated combustion) or in the partial differential equations and the boundary condition (distributed combustion). In either case it was these terms, combined with the nonlinear wave propagation terms, that determined the form of the arbitrary first order function.

The second order partial differential equations that included the combustion terms and nonlinear effects were solved with relative ease, particularly in the case of concentrated combustion. However, the integration of the equations introduced two arbitrary second order functions. Thus, three arbitrary functions appeared in the second order expressions for the dependent variables. Three conditions therefore needed to be applied in order to find an equation determining the first order function. The three conditions available were the boundary conditions at $x = 0$ and $x = 1$, and the periodicity requirement. The boundary conditions were rather easily applied, though the fact that Riemann invariants are continuous to second order in shock strength through shocks of the proper family had to be used in order to apply the boundary conditions correctly

when discontinuous oscillations were considered. The application of the periodic condition, on the other hand, presented some difficulties because, in general, the period of the assumed oscillation had to be considered different from the period of the first order function. In other words, the period could not be taken a priori to be equal to the acoustic period but, rather, was taken to have a value within a correction of order M of it. The difficulties occurring because of this difference in periods were overcome by introducing a stretched time coordinate, θ , to replace the physical time coordinate, t . This insured that to all orders of approximation the period of oscillation in the stretched time variable would be equal to the acoustic period. When this transformation was made, the periodic condition was implicitly applied and, therefore, the application of the boundary conditions to the second order solutions in θ , x space produced a nonlinear equation determining if periodic solutions for the arbitrary first order function, f , were possible and, if so, what their form and dependence upon n and μ was. (μ is the stretched time-lag that enters when the time coordinate is stretched.) Also, the equation determined whether the periodic solutions were continuous or discontinuous.

For the case of concentrated combustion the equation determining the form of f was a nonlinear, first order ordinary differential equation with a retarded variable. For the general case of distributed combustion the equation was a nonlinear differential-integral equation with a retarded variable. However, for the special combustion distribution with $\frac{d\bar{u}}{dx} = M_E$, the governing equation could be transformed into the same equation as the one governing f for the case of concentrated combustion.

Only a little information on the behavior of the ordinary differential equation for the case of concentrated combustion could be found analytically, however these findings were of some importance in setting up the numerical procedure for the integration of the equation. The most important result of the analytical examination of the equation was probably the discovery that discontinuous solutions to the equation with the same n value, but with μ values displaced symmetrically from the line $\mu = 1$, could be related by a simple 180° rotation. Because of the relationship between solutions symmetrically displaced from $\mu = 1$, curves of amplitude as

functions of n and μ were found to be symmetric with respect to the line $\mu = 1$. This meant also that the nonlinear stability limit had to be symmetric with respect to the line $\mu = 1$. The periods of the oscillations that were solutions to the governing equation, on the other hand, were found to be antisymmetric with respect to $\mu = 1$. In particular, solutions along the line $\mu = 1$ had to be resonant oscillations, solutions with $\mu > 1$ below resonant oscillations and solutions with $\mu < 1$ above resonant oscillations. These symmetry characteristics of the equation meant that numerical integration of the nonlinear ordinary differential equation only had to be carried out for $\mu \leq 1$ in order to find all solutions in the interval $0 < \mu < 2$. This interval corresponds to the range of interest for the fundamental longitudinal mode of oscillation.

In addition to the symmetry properties of the solutions to the equation governing f for concentrated combustion (or distributed combustion with $\frac{d\bar{u}}{dx} = M_E$), two additional analytical findings are of interest. The first of these is the requirement that the integral of f over one period of oscillation is zero. This means that the deviation of the mean pressure from the steady-state value must be zero to first order, even when discontinuous pressure waves are present. Moreover, for the case of distributed combustion with $\frac{d\bar{u}}{dx} = M_E$, it implies that the value of the first order entropy variation is equal to zero, since this quantity is proportional to the mean pressure. It should be noted that the comments just made with respect to the mean pressure and first order entropy need not necessarily be true for general combustion distributions with $\frac{d\bar{u}}{dx} = O(M_E)$. However, it is likely that, because of the spreading of the combustion, the deviation in the entropy from its steady value should be small, and, since the two quantities are proportional, the mean pressure change should also be small.

The second additional analytical result was the finding the discontinuous solutions existed right up to the stability limit when $\mu = 1$. This agrees with a result of the analysis performed by Sirignano⁸ using a combustion model that did not consider phasing effects. He also found discontinuous solutions right up to the linear stability limit. Since the line $\mu = 1$ represents the line along which energy is added in phase with the pressure oscillations in the present analysis, the agreement

between the two investigations is obvious. Moreover, it was found that, as one moved along the line $\mu = 1$, away from the linear stability limit, the amplitude of the shocks increased linearly with the distance from the linear limit. The same result was found by Sirignano using his different combustion model.

As far as the actual numerical integration of the ordinary nonlinear differential equation resulting from the study of concentrated combustion is concerned, little can be said without going into great detail. However, a method of functional iteration had to be used because of the appearance of retarded variable, μ , in the equation. This method converged rapidly to a proper periodic solution, if one existed at all, for the n and μ values considered. This numerical technique was used to find both continuous and discontinuous solutions. However, a convenient method of finding approximate continuous solutions valid close to the linear stability limit was also developed. In order to find these approximate solutions the governing ordinary differential equation was treated by a Fourier analysis technique in which the quantity f/M (or f/M_E) was taken to be a small quantity that vanished at the stability limit, in agreement with earlier linear analyses. The agreement between the approximate solutions and the numerical solutions for continuous oscillations close enough to the linear stability limit was found to be very good. However, at larger distances from the stability limit, considerable divergence between the two methods of solution was observed.

Numerical integration of the equation in question for a wide range of values of n and μ permitted the construction of a nonlinear stability limit for discontinuous solutions as shown in Figure 26. Inside this curve it is possible to find stable, periodic discontinuous solutions. Outside the curve no periodic discontinuous solutions at all could be found. Comparison of the nonlinear stability limit with the linear stability limit shows that three regions with different stability characteristics exist. The largest region is the region where the area inside the linear stability limit is also inside the nonlinear stability limit. Since, by linear analysis, the growth of small perturbations was predicted here, while, at the same time, discontinuous periodic pressure waves are also predicted by the present nonlinear analysis, the conclusion is reached that

the predicted discontinuous oscillations in this region are the final form that pressure oscillations would take in a rocket engine that was intrinsically unstable because of its n and μ values being in this region of linear instability. In other words, the discontinuous periodic oscillations are taken to be the regime form of instability in this region. It should be noted that much of this region is far from the linear stability limit, in regions where f/M can be quite large. However, the analysis is still asymptotically valid for small enough M , even when this is the case. In contrast to this, the validity of the nonlinear work of Sirignano,⁸ which predicted only continuous finite amplitude oscillations using the time-lag model, was restricted to regions very close to the linear stability limit.

The second region of interest was found to be the region that is inside the linear stability limit but outside the nonlinear stability limit for discontinuous oscillations. The situation here is found to be really quite similar to the one just mentioned, except that the final form that intrinsic instability takes in this region is found to be characterized by periodic continuous oscillations of finite amplitude, rather than by periodic discontinuous oscillations.

The final region of interest is the area that is outside the linear stability limit (in a region of linear stability) but inside the nonlinear stability limit. It can be argued that this is a region where the possibility of triggering discontinuous periodic pressure oscillations exists. This is because, for a given n and μ in this region, two periodic solutions are found, (see Figure 27), a large amplitude discontinuous solution and a smaller amplitude solution that was either discontinuous or continuous, depending on the normal displacement of the n, μ point under consideration from the linear stability limit. The smaller amplitude solutions are interpreted as being unstable solutions and thus as representing a triggering limit, in the sense that a disturbance with an amplitude smaller than that of the small amplitude solution at a given n and μ would decay to zero, in agreement with the predictions of linear analysis, while a disturbance with an amplitude greater than that of the small amplitude solution would grow in time and have the large amplitude discontinuous solution as its limit cycle. In other words, though

combustors with n and μ in this region should be intrinsically stable, it should be possible to trigger a discontinuous periodic oscillation by the introduction of a disturbance with large enough pressure amplitude. Note that the final form that triggered instability takes is predicted in the present analysis. Earlier work by Sirignano⁸ predicted that triggering was possible, but, because of the restriction of his analysis to continuous waveforms, the final form and amplitude of the oscillations so triggered could not be predicted.

In the last two regions of the n, μ plane mentioned, continuous periodic oscillations were found. In the region where no triggering was possible, but where linear instability was predicted, the continuous oscillations were found to be stable. In the other region, where triggering was possible, the oscillations were taken to be unstable. In both cases the question of how well the continuous solutions matched the discontinuous solutions arises. In the former situation the matching occurs at the boundary of the region, in the latter it occurs inside the region under investigation. The correspondence between the amplitude and period of the continuous and discontinuous periodic oscillations was found to be very good in both cases. The matching of the amplitudes of oscillation between the continuous and discontinuous solutions is shown in Figures 27 and 28 for two regions on the n, μ plane where, respectively, triggering is possible and impossible. The matching of the first order periods of oscillation for discontinuous and continuous oscillations in the same two regions is shown in Figures 27 and 30. In both cases the matching point occurs at a normal displacement from the linear stability limit where the amplitude of g becomes asymptotically equal to T_1 . This corresponds to the point where the nonlinear ordinary differential equation passes from a region where singular behavior is possible to one in which no such behavior is possible. The former is true for amplitudes of g greater than T_1 , the latter for amplitudes less than T_1 . Therefore, it is found that a natural transition from discontinuous to continuous waveforms is inherent in the governing ordinary differential equation.

The wave shapes themselves were found to be strongly dependent on

the parameters n and μ . This is true for both continuous and discontinuous oscillations. The continuous oscillations exhibited pressure waveforms, generally of a sinusoid nature, with a steep, sharp positive peak followed by a shallower negative peak. The sharpness and steepness of the positive peak was observed to increase (as well as the amplitude of the oscillation) as the normal displacement from the linear stability limit was increased. The wave had an arbitrarily steep slope arbitrarily close to the value of the normal displacement where the amplitude of g became equal to T_1 . This behavior is shown in Figure 31.

The salient feature of all the discontinuous waveforms that were found was the negative infinite slope at μ time units after the shock. This can be seen for the particular waveform shown in Figure 32. This reflects the fact that a discontinuity in pressure occurring at a given instant has an effect on the mass release and therefore on the waveform exactly μ time units later. Because the combustion term, or mass generation term, is one order of magnitude smaller ($O(M^2)$ vs. $O(M)$) than the shock itself, the delayed effect is not felt as a discontinuity in f but rather as an infinitely rapid continuous change in f .

Another characteristic of the discontinuous waveforms was their change in shape as the normal displacement from the linear stability limit was varied. In general, as the displacement from the linear stability limit was increased, the waveforms tended toward the classical "sawtooth" form found in one dimensional cavities with no combustion.²⁷ As the distance from the linear stability limit became small, on the contrary, the wave shapes tended to have a more sinusoid nature (except, of course, for the infinite slope at μ time units after the shock), similar to those predicted by Chester²⁶ for driven oscillations near resonance. This changing character of the waveforms is shown in Figure 33.

In conclusion, it should be emphasized that the possibility of predicting discontinuous oscillations which represent the form that regime oscillations in a liquid rocket motor with the combustion processes represented in a gross way by the time-lag model, has been demonstrated.

B. NONLINEAR TRANSVERSAL INSTABILITY

In addition to the nonlinear study of axial mode instability described in Section A, work is proceeding on the investigation of nonlinear instability for the transversal modes of oscillation.

The general mathematical techniques used in the study of longitudinal oscillations are also employed in the transversal mode investigation. The Mach number is used as the expansion parameter in the power series representations of the dependent variables necessary for the solution of the governing system of nonlinear partial differential equations. The combustion chamber is taken to be a thin annulus and the oscillations assumed to be purely transversal. Under these conditions the lowest order partial differential equations are simply the linear equations of acoustics, as was the case for the longitudinal mode of oscillation. This equation is solved in terms of an arbitrary function representing the fundamental spinning mode of oscillation. An equation determining the wave shape of this first order function is found by solving the second order partial differential equations and by applying the injector and nozzle boundary conditions as well as the conditions at the travelling shock wave and the periodicity requirement.

In order to avoid secular terms in the equations and in order to properly apply the periodic condition it is necessary to stretch the independent variables in the form of a power series in the Mach number. The expansion of the independent variables is analogous to the expansion of the time coordinate in the longitudinal study.

Two combustion models are considered in the case of transversal oscillations. The first uses the heuristic representation of combustion provided by the time-lag model.^{4,5} The second employs a simplified droplet evaporation model.

When the time-lag model is used the equation controlling the waveform of the first order function for the fundamental spinning mode is of the same form as the corresponding equation controlling the form of the waveform for the fundamental longitudinal mode. In fact, through the use of a simple transformation the two equations can be made identical. Thus all the results found for the case of concentrated combustion in the longitudinal mode can be used directly for the fundamental spinning mode. These results will, of course, include the prediction of the waveforms for both discontinuous and continuous

oscillations. It should be remarked that, though a distributed combustion zone is considered in the transversal investigations, the fact that the addition of mass is distributed in the axial direction and not in the transversal direction means that no integral terms appear in the governing equation for the spinning mode of oscillation as they did in the governing equation for longitudinal oscillations when distributed combustion was considered.

The simplified droplet evaporation model mentioned earlier as the second combustion model which is considered is defined by the following assumptions:

- 1) The transformation into burned gases immediately follows the evaporation of the propellants, so that the rate of combustion coincides with the rate of evaporation.
- 2) The rate of evaporation is determined in a quasi-steady fashion by the well known empirical expression used by other authors (i.e., Priem and Heidmann, NASA TR-R67)²⁸ with the conduction term neglected with respect to the convection term.
- 3) The drag of the droplet is considered negligible.

With a few additional assumptions, the terms can be ordered in such a way that for vanishing injection flux the combustion stays distributed and that the first nonlinear terms of the gasdynamical equations, as well as the effects of the pressure oscillations and of the transversal velocity oscillations on the combustion rate are all contained in the second order equations.

The solution then can proceed in a way similar to that used for the time-lag model, with the result that instability is possible only if the quantity

$$\frac{\gamma V_f^{*} p^{*} u_\ell^{*2}}{c^{*4} m_i^{*}}$$

is smaller than a certain value, under which waves of a very sharp type are possible independently of the frequency of the system.

The fact that the result is independent of the frequency can be attributed to certain of the assumptions used in the treatment. More sophisticated assumptions should bring in evidence the effects of the frequency.

C. DROPLET BURNING UNDER OSCILLATORY CONDITIONS

A linear analysis for the dynamic behavior of droplet vaporization process in a rocket combustion chamber with transverse acoustic waves is developed. Small perturbation of the oscillation components of all the physical quantities is assumed in this study. The dynamic response shows a strong dependence on the oscillation frequency. The characteristic curve of the response reaches a peak positive value at a particular frequency and becomes negative when the frequency is larger than a certain value. The effects of combustor conditions (pressure, temperature, and gas exit velocity) and initial conditions of the liquid drop (temperature, size and velocity) are shown. Comparison with the nonlinear numerical result is discussed.

Inside a rocket combustion chamber, acoustic mode instability takes place when the energy of the combustion is generated in some particular manner that amplifies the acoustic oscillations. A combustion process can be considered to consist of several processes in parallel or in sequence: atomization, vaporization, mixing and chemical reactions. Certain assumptions and approximations must be made in order to simplify the problem for analytical treatment. Droplet vaporization is one of the processes to be suggested as rate-controlling. That means, the vaporization of liquid drop is the controlling factor for the rates of heat release and mass addition. In the work of Priem and Guentert,²⁹ variations in vaporization rate were shown to be able to affect combustion stability significantly. This vaporization process was studied more thoroughly by Heidmann and Wieber³⁰ from a nonlinear numerical analysis by using a model predicting the vaporization rate for the entire drop life. In their work, acoustic oscillations of pressure and velocity are superimposed on the mean vaporization process. Each drop's history is considered for different boundary conditions and summation of all the drops is made to obtain the time variation of vaporization rate in the combustion chamber. This nonlinear numerical analysis motivates the investigation of a linear approach based on the same combustion model. A more rigorous mathematical treatment with the assumption of small perturbations is developed for the case with transverse oscillations.

It is assumed that the mixing and chemical reaction rates are much

higher than the vaporization rate. So the combustion rate is vaporization controlled. Several assumptions are made in the derivation:

- 1) The mean steady flow is one dimensional.
- 2) The mean combustion gas pressure and temperature are essentially constants.
- 3) All droplets have the same initial radius, temperature and velocity (i.e., at the injection face).
- 4) Mass transfer results from a driving force of concentration gradient only.
- 5) The droplet temperature is considered to be uniform over the whole droplet.

Details of the derivation can be found in the work by Priem and Heidmann.²⁸

The vaporization rate of a single droplet is

$$W^* = F^* H \text{ Num} \quad (1)$$

where

$$F^* = 2\pi r^* D^* \frac{M_v^* p^*}{R^* T^*} \quad (2)$$

$$H = \ln \left(\frac{p^*}{p^* - p_v^*} \right) \quad (3)$$

and Num is the Nusselt number for mass transfer and is related to the Reynolds number by the semi-empirical relation:

$$\text{Num} = 2. + 0.6 \text{ Sc}^{*\frac{1}{3}} \text{ Re}^{*\frac{1}{2}} \quad (4)$$

and Reynolds number is defined by:

$$\text{Re}^* = \frac{2 r^* \rho^* |g_s^* - g_g^*|}{\mu^*} \quad (5)$$

The heat which is transferred from the gas to the droplet is:

$$Q_v^* = 2 \pi r^* k^* N_{uh} (T^* - T_e^*) Z \quad (6)$$

where N_{uh} is the Nusselt number for heat transfer:

$$N_{uh} = 2. + 0.6 Pr^{*\frac{1}{3}} Re^{*\frac{1}{2}} \quad (7)$$

Z is the correction factor for heat transfer. It represents the ratio of heat that is conducted with mass transfer to that without mass transfer. The value of Z is always less than unity since the mass transfer reduces the heat transferred to the surface of the droplet.

$$Z = \frac{\delta^*}{e^{\delta^*} - 1.0} \quad (8)$$

and

$$\delta^* = \frac{W^* C_{pv}^*}{2 \pi r^* k^* N_{uh}} \quad (9)$$

Q_e^* is the heat received by the droplet and causes the droplet heat-up.

$$Q_e^* = Q_v^* - W^* \lambda^* \quad (10)$$

The mass of the droplet is:

$$m^* = \frac{4}{3} \pi r^{*3} \rho_e^* \quad (11)$$

The vaporization rate per unit volume is:

$$W_T^* = n^* W^* \quad (12)$$

The equation of state is:

$$\rho^* = \frac{p^* M_g^*}{R^* T^*} \quad (13)$$

Five differential equations are needed for the five unknowns: drop temperature, mass, velocity, number density and combustion gas velocity. The change in drop temperature is related to the heat received by the drop:

$$\frac{DT_e^*}{Dt^*} = \frac{Q_e^*}{m^* C_{pe}^*} \quad (14)$$

The decrease of drop mass is equal to the vaporization rate:

$$\frac{Dm^*}{Dt^*} = -W^* \quad (15)$$

The change of drop velocity is

$$\frac{D\vec{g}_e^*}{Dt^*} = C_D \frac{\pi r^{*2}}{m^*} \frac{\rho^* |\vec{g}^* - \vec{g}_e^*|}{2} (\vec{g}^* - \vec{g}_e^*) \quad (16)$$

where C_D is the drag coefficient and is chosen to be

$$C_D = \frac{27}{Re^*} \quad (17)$$

The number of droplets is conserved, so we have:

$$\frac{\partial n^*}{\partial t^*} + \nabla \cdot n^* \vec{g}_e^* = 0 \quad (18)$$

The combustion gas continuity equation gives the relation for gas velocity and the mass addition:

$$\frac{\partial \rho^*}{\partial t^*} + \nabla \cdot \rho^* \vec{g}^* = n^* W^* \quad (19)$$

With proper initial and boundary conditions, this set of equations can be solved by numerical integration.

In order to take a closer look at the effects of all the physical parameters, a dimensionless formulation is more valuable. The reference values of pressure and temperature are chosen to be the mean gas pressure and temperature, respectively - and the reference gas density is:

$$\rho_{\infty} = \frac{p_{\infty} M_g^*}{R^* T_{\infty}} \quad (20)$$

$C_{p\infty}$, μ_{∞} , D_{∞} , k_{∞} and $C_{pv\infty}$ are evaluated at p_{∞} , T_{∞} .
The specific heat ratio is:

$$\gamma = C_{p\infty} / (C_{p\infty} - R^* / M_g^*) \quad (21)$$

The speed of sound is:

$$c_{\infty} = \sqrt{\gamma R^* T_{\infty} / M_g^*} \quad (22)$$

The reference length and velocity are chosen to be the chamber length and speed of sound, respectively and the reference time is defined as:

$$t_{\infty} = \frac{L_{\infty}}{c_{\infty}} \quad (23)$$

The initial drop radius is used to normalize the drop radius.

Also, the reference quantities of the droplet $C_{p\infty}$, ρ_{∞} , and λ_{∞} are evaluated at the initial temperature of the droplet. The initial drop number density is used to normalize the drop number density.

Define the dimensionless quantities:

$$\begin{aligned} p &\equiv \frac{p^*}{p_{\infty}}, & T &\equiv \frac{T^*}{T_{\infty}}, & \rho &\equiv \frac{\rho^*}{\rho_{\infty}} \\ x &\equiv \frac{x^*}{L_{\infty}}, & t &\equiv \frac{t^*}{t_{\infty}}, & g &\equiv \frac{g^*}{c_{\infty}} \\ C_p &\equiv \frac{C_p^*}{C_{p\infty}}, & \mu &\equiv \frac{\mu^*}{\mu_{\infty}}, & D &\equiv \frac{D^*}{D_{\infty}} \\ C_{pv} &\equiv \frac{C_{pv}^*}{C_{pv\infty}}, & k &\equiv \frac{k^*}{k_{\infty}} \end{aligned}$$

$$r \equiv \frac{r^*}{r_\infty}, \quad T_e \equiv \frac{T_e^*}{T_\infty}, \quad C_{pe} \equiv \frac{C_{pe}^*}{C_{pe\infty}}$$

$$\rho_e \equiv \frac{\rho_e^*}{\rho_\infty}, \quad \lambda \equiv \frac{\lambda^*}{\lambda_\infty}, \quad n \equiv \frac{n^*}{n_\infty}$$

For convenience, we separate Re^* into two parts:

$$Re^* = Re_\infty Re$$

where

$$Re_\infty = 2 r_\infty \rho_\infty c_\infty / \mu_\infty$$

and

$$Re = r \rho |q - q_e| / \mu \quad (24)$$

Assume that:

$$Sc^* = Sc_\infty = \text{constant}$$

$$Pr^* = Pr_\infty = \text{constant}$$

We have Num and Nuh :

$$Num = 2. + 0.6 \phi Re^{\frac{1}{2}}$$

$$Nuh = 2. + 0.6 \psi Re^{\frac{1}{2}}$$

where

$$\phi = Re_\infty^{\frac{1}{2}} Sc_\infty^{\frac{1}{3}} \quad (25)$$

$$\psi = Re_\infty^{\frac{1}{2}} Pr_\infty^{\frac{1}{3}} \quad (26)$$

The p_v^* is related to T_e^* by such relations:

$$p_v^* = \exp \left(d_1^* + \frac{d_2^*}{T_e^* + d_3^*} \right) \quad (27)$$

where d_1^* , d_2^* and d_3^* are empirical constants.

In dimensionless form:

$$p_v = \frac{e^{d_1^*}}{p_\infty} \exp \left(\frac{d_2^*}{T_e + d_3^*} \right)$$

where

$$d_2 \equiv \frac{d_2^*}{T_\infty}, \quad d_3 \equiv \frac{d_3^*}{T_\infty}$$

Certain dimensional and dimensionless groups are defined as follows:

$$F^* = F_\infty F$$

$$F_\infty = 2\pi r_\infty \rho_\infty D_\infty \frac{M_v^*}{M_g^*}, \quad F = r \rho D \quad (28)$$

$$W^* = W_\infty W$$

$$W_\infty = F_\infty, \quad W = F H \text{Num} \quad (29)$$

$$Z^* = Z_\infty Z$$

$$Z_\infty = \frac{W_\infty C_{pv\infty}}{2\pi k_\infty r_\infty}, \quad Z = H \frac{\text{Num}}{\text{Nu}k} \quad (30)$$

$$Q_v^* = Q_{v\infty} Q_v$$

$$Q_{v\infty} = 2\pi k_\infty r_\infty T_\infty, \quad Q_v = k r \text{Nu}h \cdot (T - T_e) Z \quad (31)$$

$$Q_e^* = Q_{v\infty} (Q_v - Q_{e\infty} W \lambda)$$

$$Q_{e\infty} = \frac{W_\infty \lambda_\infty}{Q_{v\infty}}, \quad Q_e = Q_v - Q_{e\infty} W \lambda \quad (32)$$

$$m^* = m_\infty m$$

$$m_\infty = \frac{4}{3} \pi r_\infty^3 \rho_\infty, \quad m = r^3 \rho_l \quad (33)$$

$$W_T = n W \quad (34)$$

The differential equations for drop temperature, drop mass, drop velocity, number density and gas velocity take the following forms:

$$\frac{DT_e}{Dt} = \alpha \frac{Q_l}{m C_{pl}} \quad (35)$$

$$\frac{Dm}{Dt} = -W\beta \quad (36)$$

$$\frac{D\vec{g}_l}{Dt} = \delta \frac{\mu r}{m} (\vec{g} - \vec{g}_l) \quad (37)$$

$$\frac{\partial n}{\partial t} + \nabla \cdot n \vec{g}_l = 0 \quad (38)$$

$$\frac{\partial \rho}{\partial t} + \nabla \cdot \rho \vec{g} = \eta n W \quad (39)$$

where α , β , δ , η are dimensionless quantities which are fixed for a particular problem:

$$\alpha = \frac{2 \pi k_\infty r_\infty}{m_\infty C_{pl_\infty}} t_\infty \quad (40)$$

$$\beta = 2 \pi \rho_\infty D_\infty \frac{r_\infty}{m_\infty} \frac{M_o^*}{M_g^*} t_\infty \quad (41)$$

$$\delta = \frac{13.5 \pi \rho_\infty L_\infty}{Re_\infty} \frac{r_\infty^2}{m_\infty} \quad (42)$$

$$\eta = \frac{n_{\infty} W_{\infty}}{p_{\infty}} \dot{t}_{\infty} \quad (43)$$

A numerical example of the normal heptane with gaseous oxygen case has been obtained for the steady mean flow; some of the physical quantities are given here:

$$\begin{aligned} p_{\infty} &= 20.0 \text{ atm} \\ T_{\infty} &= 3000.0 \text{ }^{\circ}\text{K} \\ L_{\infty} &= 25.0 \text{ cm} \\ u_F^* &= 250.0 \text{ m/sec} \\ r_{\infty} &= 75 \times 10^{-4} \text{ cm/sec} \\ T_{e_{\infty}} &= 300.0 \text{ }^{\circ}\text{K} \\ u_{e_0}^* &= 30.0 \text{ m/sec} \end{aligned}$$

Figures 34-38 show the variations of drop temperature, drop radius and mass, gas velocity and drop velocity, vaporization rate per drop and vaporization rate per unit volume along the axial direction of the combustion chamber. Discussion of the results can be found in Ref. 28.

By using the vaporization model just described, a quasi-steady linear analysis with transverse waves is developed. A small parameter ϵ is introduced here. This parameter is assumed to be the amplitude of pressure oscillation at a specific radial and angular position.

We have

$$\begin{aligned} p &= 1 + \epsilon p_1, & T &= 1 + \epsilon T_1, \\ \rho &= 1 + \epsilon \rho_1, \\ u &= \bar{u} + \epsilon u_1, & u_r &= \bar{u}_r + \epsilon u_{r1}, \\ v &= \epsilon v_1, & v_r &= \epsilon v_{r1}, \\ & \dots \end{aligned}$$

and so on.

It is assumed that μ_1 , $\rho_1 D_1$, k_1 , λ_1 , β_1 , $C_{pl,1}$, can be neglected and also it is assumed that

$$\frac{Num}{Nuh} = \frac{\bar{Num}}{\bar{Nuh}}$$

Assume the isentropic relation for the gas

$$\begin{aligned} (1 + \epsilon p_1) &= (1 + \epsilon p_1)^{\frac{1}{\delta}} \\ (1 + \epsilon T_1) &= (1 + \epsilon p_1)^{\frac{\delta-1}{\delta}} \end{aligned}$$

Neglect the higher order terms, we obtain

$$p_1 = \frac{1}{\delta} p_1 \quad (44)$$

$$T_1 = \frac{\delta-1}{\delta} p_1 \quad (45)$$

With the assumption of pure transverse mode, (i.e., $u_1 \equiv u_e \equiv 0$), the velocity perturbation enters into the problem in higher order terms only. This makes the linear analysis possible.

After some algebraic manipulation, the following perturbation quantities are obtained:

$$Re_1 = \left(\frac{r_1}{r} + \frac{p_1}{\delta} \right) \quad (46)$$

$$Num_1 = 0.3 \phi Re_1 \quad (47)$$

$$Nuh_1 = 0.3 \psi Re_1 \quad (48)$$

$$F_1 = r_1 \quad (49)$$

$$p_{v1} = - \frac{d_2 \bar{p}_v}{(\bar{T}_e + d_3)^2} T_{e1} \quad (50)$$

$$H_1 = \frac{-\bar{p}_v}{1-\bar{p}_v} \left[p_1 + \frac{d_2}{(\bar{T}_e + d_3)^2} T_{e1} \right] \quad (51)$$

The perturbation of vaporization rate is

$$W_1 = C_1 T_{e1} + C_2 M_1 + C_3 p_1 \quad (52)$$

where

$$C_1 = \bar{r} \bar{N}_{um} \left(\frac{-\bar{p}_v}{1-\bar{p}_v} \right) \frac{d_2}{(\bar{T}_e + d_3)^2} \quad (53)$$

$$C_2 = \frac{\bar{H}}{3 \bar{r}^2 \bar{\rho}_e} \left[\bar{N}_{um} + 0.3 \phi \bar{Re}^{\frac{1}{2}} \right] \quad (54)$$

$$C_3 = \bar{r} \left[\left(\frac{-\bar{p}_v}{1-\bar{p}_v} \right) \bar{N}_{um} + \frac{\bar{H}}{\delta} 0.3 \phi \bar{Re}^{\frac{1}{2}} \right] \quad (55)$$

they are functions of the steady solution only.

The perturbation of the vaporization rate per unit volume is

$$W_{T1} = W_1 \frac{\bar{u}_{e0}}{\bar{u}_e} \quad (56)$$

Other perturbation quantities are:

$$z_1 = \frac{\bar{N}_{um}}{\bar{N}_{ueh}} \left(\frac{-\bar{p}_v}{1-\bar{p}_v} \right) \left[p_1 + \frac{d_2}{(\bar{T}_e + d_3)^2} T_{e1} \right] \quad (57)$$

$$z_1 = \frac{\bar{z}}{\bar{\delta}} (1 - \bar{z} e^{\bar{\delta}^*}) z_1 \quad (58)$$

$$\begin{aligned}
 Q_{v1} = & \bar{Z} (1 - \bar{T}_e) [\bar{N}_{uL} + 0.3 \psi \bar{R}e^{\frac{1}{2}}] r_1 \\
 & + \bar{r} \bar{Z} \left[\left(\frac{1 - \bar{T}_e}{\delta} \right) 0.3 \psi \bar{R}e^{\frac{1}{2}} + \frac{\delta - 1}{\delta} \bar{N}_{uL} \right. \\
 & \left. + (1 - \bar{T}_e) \frac{\bar{N}_{um}}{\bar{\delta}} (1 - \bar{z} e^{\bar{\delta}^*}) \left(\frac{-\bar{p}_v}{1 - \bar{p}_v} \right) \right] p_1 \\
 & + \bar{r} \bar{Z} \left[-\bar{N}_{uL} + (1 - \bar{T}_e) \frac{\bar{N}_{um}}{\bar{\delta}} (1 - \bar{z} e^{\bar{\delta}^*}) \right. \\
 & \left. \cdot \left(\frac{-\bar{p}_v}{1 - \bar{p}_v} \right) \frac{d_2}{(\bar{T}_e + d_3)^2} \right] T_{e1}
 \end{aligned} \tag{59}$$

$$\begin{aligned}
 Q_{e1} = & \left\{ \bar{Z} (1 - \bar{T}_e) [\bar{N}_{uL} + 0.3 \psi \bar{R}e^{\frac{1}{2}}] \right. \\
 & \left. - Q_{e\infty} \bar{\lambda} \bar{H} [\bar{N}_{um} + 0.3 \phi \bar{R}e^{\frac{1}{2}}] \right\} r_1 \\
 & + \left\{ \bar{r} \bar{Z} \left[\frac{\delta - 1}{\delta} \bar{N}_{uL} + (1 - \bar{T}_e) \left(\bar{N}_{um} \frac{1 - \bar{z} e^{\bar{\delta}^*}}{\bar{\delta}} \frac{-\bar{p}_v}{1 - \bar{p}_v} \right. \right. \right. \\
 & \left. \left. + \frac{1}{\delta} 0.3 \psi \bar{R}e^{\frac{1}{2}} \right) \right] - Q_{e\infty} \bar{\lambda} \bar{r} \left[\bar{N}_{um} \left(\frac{-\bar{p}_v}{1 - \bar{p}_v} \right) \right. \right. \\
 & \left. \left. + \frac{\bar{H}}{\delta} 0.3 \phi \bar{R}e^{\frac{1}{2}} \right] \right\} p_1 + \bar{r} \left\{ \bar{Z} [-\bar{N}_{uL} \right. \\
 & \left. + (1 - \bar{T}_e) \bar{N}_{uL} \frac{1 - \bar{z} e^{\bar{\delta}^*}}{\bar{\delta}} \left(\frac{-\bar{p}_v}{1 - \bar{p}_v} \right) \frac{d_2}{(\bar{T}_e + d_3)^2} \right] \\
 & \left. - Q_{e\infty} \bar{\lambda} \left[\bar{N}_{um} \left(\frac{-\bar{p}_v}{1 - \bar{p}_v} \right) \frac{d_2}{(\bar{T}_e + d_3)^2} \right] \right\} T_{e1}
 \end{aligned} \tag{60}$$

$$\gamma_1 = \frac{1}{3 \bar{r}^2 \bar{\rho}_e} m_1 \quad (61)$$

Only two partial differential equations remain to be considered here: one for the perturbation drop mass and one for the perturbation drop temperature. They take the form of:

$$\frac{\partial T_{e1}}{\partial t} + \bar{u}_e \frac{\partial T_{e1}}{\partial z} = A_1 T_{e1} + A_2 m_1 + A_3 p_1 \quad (62)$$

$$\frac{\partial m_1}{\partial t} + \bar{u}_e \frac{\partial m_1}{\partial z} = B_1 T_{e1} + B_2 m_1 + B_3 p_1 \quad (63)$$

where

$$\begin{aligned} A_1 = \frac{\alpha \bar{r}}{\bar{m} \bar{C}_{pe}} \left\{ \bar{Z} \left[-\bar{N}_{ueh} + (1-\bar{T}_e) \bar{N}_{ueh} \frac{1-\bar{Z} e^{\bar{Z}^*}}{\bar{Z}} \right. \right. \\ \cdot \left. \left(\frac{-\bar{p}_v}{1-\bar{p}_v} \right) \frac{d_2}{(\bar{T}_e + d_3)^2} \right] - Q_{e\infty} \bar{\lambda} \left[\bar{N}_{um} \left(\frac{-\bar{p}_v}{1-\bar{p}_v} \right) \right. \\ \cdot \left. \left. \frac{d_2}{(\bar{T}_e + d_3)^2} \right] \right\} \end{aligned} \quad (64)$$

$$\begin{aligned} A_2 = \frac{\alpha}{\bar{m} \bar{C}_{pe}} \left[\left\{ \bar{Z} (1-\bar{T}_e) [\bar{N}_{ueh} + 0.3 \psi \bar{Re}^{\frac{1}{2}}] \right. \right. \\ \left. \left. - Q_{e\infty} \bar{\lambda} \bar{H} [\bar{N}_{um} + 0.3 \phi \bar{Re}^{\frac{1}{2}}] \right\} \frac{1}{3 \bar{r}^2 \bar{\rho}_e} \right. \\ \left. - \frac{\bar{Q}_e}{\bar{m}} \right] \end{aligned} \quad (65)$$

$$\begin{aligned}
 A_3 = & \frac{\alpha}{m \bar{C}_{pe}} \left\{ \bar{r} \bar{z} \left[\frac{\delta-1}{\delta} \bar{N}_{ul} \right. \right. \\
 & + (1-\bar{T}_e) \left(\bar{N}_{um} \frac{1-\bar{z} e^{\bar{z}^*}}{\bar{z}} \left(\frac{-\bar{p}_v}{1-\bar{p}_v} \right) \right. \\
 & \left. \left. + \frac{0.3}{\delta} \psi \bar{Re}^{\frac{1}{2}} \right) \right] - Q_{e\infty} \bar{\pi} \bar{r} \\
 & \cdot \left[\bar{N}_{um} \left(\frac{-\bar{p}_v}{1-\bar{p}_v} \right) + \frac{\bar{H}}{\delta} 0.3 \phi \bar{Re}^{\frac{1}{2}} \right] \left. \right\} \quad (66)
 \end{aligned}$$

$$B_1 = -\beta C_1 \quad (67)$$

$$B_2 = -\beta C_2 \quad (68)$$

$$B_3 = -\beta C_3 \quad (69)$$

All A_1 , A_2 , A_3 , B_1 , B_2 and B_3 are functions of the steady-state solution only.

A dimensionless frequency is introduced so that

$$f \equiv f^* t_\infty \quad (70)$$

and the angular frequency is:

$$\omega = 2\pi f \quad (71)$$

The acoustic mode pressure oscillation has this form:

$$p_1 = P(x, r, \theta) \sin \omega t$$

where P is a function of position. However, in the case of transverse oscillation and with the consideration of fixed radial and angular position, the pressure perturbation can be simplified to:

$$p_1 = \sin \omega t \quad (72)$$

P is absorbed in the ϵ because it is a constant here. All other quantities will have the same transverse behavior since the velocity effect is of higher order. Therefore, only x and t dependence will be considered.

We expect solution of these forms:

$$T_{e1} = T_{es}(x) \sin \omega t + T_{ec}(x) \cos \omega t \quad (73)$$

$$m_1 = m_s(x) \sin \omega t + m_c(x) \cos \omega t \quad (74)$$

Thus, the space dependent part and time dependent part can be separated and we obtain four ordinary differential equations for T_{es} , T_{ec} , m_s , m_c .

$$\bar{u}_e \frac{dT_{es}}{dx} = A_1 T_{es} + A_2 m_s + A_3 + \omega T_{ec} \quad (75)$$

$$\bar{u}_e \frac{dT_{ec}}{dx} = A_1 T_{ec} + A_2 m_c - \omega T_{es} \quad (76)$$

$$\bar{u}_e \frac{dm_s}{dx} = B_1 T_{es} + B_2 m_s + B_3 + \omega m_c \quad (77)$$

$$\bar{u}_e \frac{dm_c}{dx} = B_1 T_{ec} + B_2 m_c - \omega m_s \quad (78)$$

This set of differential equations is ready to solve with proper initial conditions.

It is assumed that the droplet initial condition is not affected by the oscillation in the combustion chamber, therefore, the initial condition for the perturbation quantities T_{es} , T_{ec} , m_s , m_c can be taken as zero.

So we have

$$T_{es}(0) = T_{ec}(0) = m_s(0) = m_c(0) = 0 .$$

The vaporization rate perturbations are:

$$W_i = W_s \sin \omega t + W_c \cos \omega t \quad (79)$$

$$W_{Ti} = W_{Ts} \sin \omega t + W_{Tc} \cos \omega t \quad (80)$$

where

$$W_s = C_1 T_{es} + C_2 m_s + C_3 \quad (81)$$

$$W_c = C_1 T_{ec} + C_2 m_c \quad (82)$$

$$W_{Ts} = \frac{\bar{u}_{e0}}{\bar{u}_e} W_s \quad (83)$$

$$W_{Tc} = \frac{\bar{u}_{e0}}{\bar{u}_e} W_c \quad (84)$$

Because numerical integration is required for the steady solution, the solution of the perturbation equations requires the result from the steady solution, therefore, numerical integration should be conducted simultaneously for both steady-state and perturbation equations.

The idea of response factor is based on the Rayleigh criterion for acoustic amplification by heat or mass addition. Reinforcement of acoustic oscillation takes place when an excess amount of heat or mass is added while the pressure is above the mean value. The response factor is defined as the integral value of such mass addition over a given period

of time and in a finite volume normalized by the magnitude of the pressure perturbation.

$$N \equiv \frac{\int_V \int_0^{\tilde{\tau}} W_T, p_i dt dV}{\int_V \int_0^{\tilde{\tau}} p_i^2 dt dV} \quad (85)$$

where $\tilde{\tau}$ is the period of oscillation

$$\tilde{\tau} = \frac{2\pi}{\omega} = \frac{1}{f} \quad (86)$$

This response factor is positive when both vaporization rate perturbation and pressure perturbation have the same signs and is negative when they have different signs. We can say that this response factor is an indication of the degree of driving or damping which the vaporization process gives a feedback to the system.

At a specific radial and angular position the response is:

$$N = \int_0^{1.0} W_{Ts} dx \quad (87)$$

A typical response curve is given in Figure 39 with the same physical condition as in that steady-state solution.

At very low frequency, the response factor is nearly a positive constant. As the frequency increases, the response factor increases and reaches a peak value. Beyond that the response factor decreases and goes into the region of negative response. The critical frequency is defined when the response factor is zero. If the acoustic frequency of the combustor is in the range of positive response, particularly near the peak, the operation of such a combustor is most likely unstable.

Several physical quantities which can affect the response factor are shown in Figures 40-45.

Figure 40 shows the effect of combustor pressure. The higher the pressure, the larger positive response factor is obtained. Figure 41 shows that the higher the combustor temperature the smaller the positive response factor. Figure 42 shows the effect of gas exit velocity. The effect on the peak is small but the critical frequency increases as the

gas exit velocity increases. Figure 43 shows that the higher the drop initial temperature, the lower the peak will become. This effect is important because the variation of drop initial temperature can be large. The effect of drop initial radius is shown in Figure 44 . Decrease of drop radius shifts the response curve to the right. Such effect is very important because the drop radius varies in quite a large range. Figure 45 shows the effect of drop initial velocity. The larger positive response corresponds to higher drop initial velocity.

The result of linear analysis is similar to that of the nonlinear numerical analysis in Ref. 30 , as far as the response is concerned. The reason for these two different approaches giving approximately the same result is that the vaporization rate depends on the absolute velocity difference of the gas and the droplet. During a period of oscillation, the vaporization rate perturbation has two peak values and the effect of pressure gives nonlinear behavior of vaporization. However, such nonlinear effects will be canceled in the evaluation of response factor. Therefore, the velocity difference effect can be neglected as an approximation, that makes the linearization possible.

In applying the vaporization mechanism as the combustion model, we must be aware of the limitations of the assumptions we have made. For instance, the uniform temperature over the whole droplet is quite questionable because the heat conductivity of the liquid droplet is not infinite and the intensity of the internal circulation of the droplet is not known.

Let us examine the heat conduction equation for spherical symmetric case:

$$\frac{\partial T^*}{\partial t^*} = \frac{k^*}{\rho^* c_p^*} \frac{1}{r^{*2}} \frac{\partial}{\partial r^*} \left(r^{*2} \frac{\partial T^*}{\partial r^*} \right) \quad (88)$$

in dimensionless form:

$$\frac{\frac{\rho_\infty c_{p_\infty}}{k_\infty} r_\infty^2}{\tilde{t}_\infty} \frac{\partial T}{\partial \tilde{t}} = \frac{k}{\rho c_p} \frac{1}{r^2} \frac{\partial}{\partial r} \left(r^2 \frac{\partial T}{\partial r} \right) \quad (89)$$

$\tilde{\tau}_\infty$ is taken to be the period of oscillation here. The parameter

$\frac{\rho_\infty c_{p\infty}}{k_\infty} r_\infty^2$ has a dimension of time and is the characteristic time for heat diffusion. The uniform temperature assumption can be made only when

$$\frac{\rho_\infty c_{p\infty} r_\infty^2}{k_\infty \tilde{\tau}_\infty} \ll 1 \quad (90)$$

We can see that this assumption is good only for small drop radius and low frequency oscillation. We can expect that the response factor we have obtained is not valid for large drop size and for high frequency oscillation.

Finally, the response factor is not a criterion for combustor stability. A complete dynamic analysis of the whole combustion system is needed to acquire such stability information, further study in this direction will be conducted.

NOMENCLATURE

A_1, A_2, A_3	defined by Equation (64)-(66)
B_1, B_2, B_3	defined by Equations (67)-69)
c	speed of sound
C_1, C_2, C_3	defined by Equations (53)-(55)
C_D	drag coefficient
C_p	specific heat at constant pressure
D	diffusivity
d_1, d_2, d_3	empirical constants in Equation (27)
f	frequency
F	defined by Equation (2)
H	defined by Equation (3)
h	thermal conductivity
L	length
m	drop mass
M	molecular weight
n	drop number density
N	response factor
N_{uh}	Nusselt number for heat transfer
N_{um}	Nusselt number for mass transfer
p	pressure
p_v	vapor pressure
P	defined by Equation (72)
Pr	Prandtl number
q	velocity
Q_e	defined by Equation (10)
Q_v	defined by Equation (6)
r	radial coordinate

r	drop radius
R	gas constants
Re	Reynolds number
Sc	Schmidt number
t	time
$\tilde{\tau}$	period of oscillation
T	temperature
u	velocity component in axial direction
v	velocity component in transverse direction
W	vaporization rate per drop
W_T	vaporization rate per unit volume
x	axial distance from injector
\bar{z}	defined by Equation (9)
Z	correction factor
α	defined by Equation (40)
β	defined by Equation (41)
γ	specific heat ratio
δ	defined by Equation (42)
ϵ	amplitude of oscillation
η	defined by Equation (43)
θ	angular coordinate
λ	latent heat
μ	viscosity
ρ	density
ϕ	defined by Equation (25)
ψ	defined by Equation (26)
ω	angular frequency

$()_{\infty}$	reference value
$(-)$	steady mean value
$()^*$	dimensional value
$()_l$	liquid or drop
$()_v$	vapor
$()_g$	gas
$()_c$	coefficient of cosine component
$()_s$	coefficient of sine component
$()_o$	at injector face
$()_F$	at nozzle entrance

D. NUMERICAL CALCULATION OF WAVE PHENOMENA IN CHAMBERS

One of the interesting questions about nonlinear gasdynamic phenomena in rocket chambers is whether or not shock waves may form in the transverse mode. Usually experimental evidence indicates continuous waves except in the longitudinal mode; however, in certain cases shocks have been observed.

The problem of nonlinear transverse waves in a circular cylinder has been analyzed by Maslen and Moore who found solutions without shocks. There is, however, no indication that those solutions are unique. One way to determine if other solutions exist is to numerically integrate the equations of motion and see what the limiting behavior is after a long time. A variety of amplitudes and wave shapes could be used in the initial conditions and it would be seen if any of these resulted in the formation of shock waves.

It is expected that shock waves would form in a thin circular annular chamber. Here the flow field is essentially one-dimensional (azimuthal) and centrifugal effects are negligible. One wonders how "thick" the annular chamber may be before shocks no longer form. An interesting parameter, therefore, is the ratio of the inner radius to outer radius which varies between zero and unity.

The problem remains as to how to write the difference equations to study transverse travelling waves. A popular technique for solving steady-state gasdynamic problems is to solve an initial-condition problem which yields the steady-state solution as its limiting behavior for large time. Note that for travelling waves a steady-state exists if one moves with the wave. This means that, if one were to observe the travelling wave from a coordinate system which rotates about the center of the cylindrical chamber at the same frequency as that of the oscillation, he would, after a long time, see a steady-state situation.

It has been intended to employ this technique for studying the wave motion in the chamber. In order to insure rapid convergence and stability with this type of difference scheme, certain terms which have no physical meaning are added to the difference equations. In the steady-state limit the effect of these terms disappear and they only affect the transient

behavior. For this reason, the transient behavior is not accurately predicted by this method.

In order to gain a better understanding of the advantages and disadvantages of this method, it was decided to compare it with the Lax-Wendroff scheme. The Lax method contains no artificial terms so that the transient behavior should be accurately predicted. Although the two-dimensional transverse case is of prime interest, it was decided to compare the two difference methods in the one-dimensional case for the initial attempt. Note that a travelling wave in a thin annulus is approximately a one-dimensional phenomenon, however.

In these one-dimensional cases a steady-state solution could only be found if we observed from a frame of reference which was in translational motion at the same velocity as the wave. Actually, in either the one or two dimensional cases, the continuous wave would distort until either a steady continuous waveform is obtained or a shock forms. If the shock forms no steady solution can really ever be achieved (in the absence of combustion) since dissipation occurs with a shock. After the shock is fully formed, its amplitude would decrease due to this dissipation. For weak shocks, however, this decay in amplitude is sufficiently slow that a steady-state would be approximated.

The equations of motion for the isentropic* flow of a perfect gas written in a frame of reference moving at constant velocity k are as follows

$$\frac{\partial \rho}{\partial t} + (u - k) \frac{\partial \rho}{\partial x} + \rho \frac{\partial u}{\partial x} = 0$$

$$\frac{\partial p}{\partial t} + (u - k) \frac{\partial p}{\partial x} + \gamma p \frac{\partial u}{\partial x} = 0$$

$$\frac{\partial u}{\partial t} + (u - k) \frac{\partial u}{\partial x} + \frac{1}{\gamma \rho} \frac{\partial p}{\partial x} = 0$$

Here, the gas velocity u is measured with respect to the original frame of reference but the time derivatives are taken in the moving coordinate

* This is only strictly valid if no shocks are present. Once shocks form, the isentropic assumption remains a good approximation as long as the shocks are weak.

system. p is pressure, ρ is density, x is position, and t is time.

The finite difference form of these equations are written as follows:

$$\rho_i^{n+1} - \rho_i^n = - (u_i^n - k) \left[(1 + \Gamma)(\rho_{i+1}^n - \rho_{i-1}^n) - \Gamma(\rho_{i+1}^{n-1} - \rho_{i-1}^{n-1}) \right] \frac{\Delta t}{2 \Delta x} \\ - \rho_i^n \left[(1 + \Gamma)(u_{i+1}^n - u_{i-1}^n) - \Gamma(u_{i+1}^{n-1} - u_{i-1}^{n-1}) \right] \frac{\Delta t}{2 \Delta x}$$

$$p_i^{n+1} - p_i^n = - (u_i^n - k) \left[(1 + \Gamma)(p_{i+1}^n - p_{i-1}^n) - \Gamma(p_{i+1}^{n-1} - p_{i-1}^{n-1}) \right] \frac{\Delta t}{2 \Delta x} \\ - \gamma p_i^n \left[(1 + \Gamma)(u_{i+1}^n - u_{i-1}^n) - \Gamma(u_{i+1}^{n-1} - u_{i-1}^{n-1}) \right] \frac{\Delta t}{2 \Delta x}$$

$$u_i^{n+1} - u_i^n = - (u_i^n - k) \left[(1 + \Gamma)(u_{i+1}^n - u_{i-1}^n) - \Gamma(u_{i+1}^{n-1} - u_{i-1}^{n-1}) \right] \frac{\Delta t}{2 \Delta x} \\ - \frac{1}{\gamma \rho_i^n} \left[(1 + \Gamma)(p_{i+1}^n - p_{i-1}^n) - \Gamma(p_{i+1}^{n-1} - p_{i-1}^{n-1}) \right] \frac{\Delta t}{2 \Delta x}$$

where Δt and Δx are the step-sizes in the difference scheme, i and n are integers which denote the x and t positions, respectively, and Γ is a factor between zero and unity.

Whenever Γ is zero, we have a simple difference scheme whereby the space derivative is represented by a centered difference. In other cases, that derivative is evaluated by averaging its value at two different times and Γ is a weighting factor in this averaging process.

Also, the equations were written in conservation form in the original coordinate system. Then, the Lax-Wendroff two-step difference scheme was employed.

The same initial conditions were provided for both schemes. In particular, sinusoidal waveforms of linear theory were provided as initial conditions. In addition to waves travelling in one Cartesian direction, the case of travelling waves in an annulus was considered. In the latter

case, periodic conditions (in space) were applied.

Figures 46 and 47 show pressure versus the azimuthal dimension in a thin annular chamber at fixed times. The first figure shows the results of the Γ -method and the second figure shows the results of the Lax-Wendroff method. Both figures indicate a steepening of the waveform and a tendency towards shock formation. Qualitatively, the agreement between the two methods is good; there are, however, quantitative differences.

It can be shown by means of Riemann invariants that, prior to shock formation, the minimum and maximum values of pressure will not change with time as the wave distorts. This is found with the Γ -method but not with the Lax method so that in this regard the Γ -method is superior. Furthermore, it indicates that, for the present purposes, the Lax method may not be entirely reliable as a standard for comparison.

No essential differences were found between the processes of shock formation for waves travelling in one Cartesian direction and waves travelling in a thin annulus.

It was concluded that the Γ -method provides a good prediction of the wave phenomenon even for the transient behavior. The difference equations were not written in a form which could account for shock waves so that a steady-state was never actually achieved. Since the ultimate purpose of this endeavor is to determine whether shocks form in the two-dimensional transverse case, it was decided not to spend any time to include the capability of handling discontinuities in the computer program until their formation became evident in the two-dimensional case. (Of course, in that event, a technique such as the pseudo-viscosity method may be employed.) For this reason, the one-dimensional calculations ended after considerable distortion of the wave but before discontinuities formed.

This endeavor is continuing with the programming of the two-dimensional case in annular and "full" chambers with both difference schemes.

REFERENCES

1. Crocco, L., Harrje, D.T., Sirignano, W.A., et al, "Nonlinear Aspects of Combustion Instability in Liquid Propellant Rocket Motors", Department of Aerospace and Mechanical Sciences Report 553-f, 1 June 1967.
2. Ibid, Report 553-e, 1 June 1965.
3. Ibid, Report 553-d, 1 June 1964.
4. Crocco, L., and Cheng, S.I., Theory of Combustion Instability in Liquid Propellant Rocket Motors, AGARD Monograph No. 8, Butterworths Scientific Pub., Ltd., London, 1956.
5. Crocco, L., "Theoretical Studies on Liquid Propellant Rocket Instability", 10th Symposium (International) on Combustion, Combustion Institute, Pittsburgh, Penn., June 1965, pg. 1101.
6. Mitchell, C.E., "Axial Mode Shock Wave Combustion Instability in Liquid Propellant Rocket Engines", Department of Aerospace and Mechanical Sciences Technical Report No. 798, July 1967. (Ph.D. Thesis) (NASA CR-72259)
7. Zinn, B.T., "A Theoretical Study of Nonlinear Transverse Combustion Instability in Liquid Propellant Rocket Motors", Technical Report No. 732, Department of Aerospace and Mechanical Sciences, Princeton University, May 1966 (Ph.D. Thesis).
8. Sirignano, W.A., "A Theoretical Study of Nonlinear Combustion Instability: Longitudinal Mode", Technical Report No. 677, Department of Aerospace and Mechanical Sciences, Princeton University, March 1964, (Ph.D. Thesis).
9. Strahle, W.C., "A Theoretical Study of Unsteady Droplet Burning: Transients and Periodic Solutions", Princeton University Aeronautical Engineering Laboratory Report No. 671, December 1963. (Ph.D. Thesis)
10. Reardon, F.H., "An Investigation of Transverse Mode Combustion Instability in Liquid Propellant Rocket Motors", Princeton University Aeronautical Engineering Report No. 550, 1 June 1961. (Ph.D. Thesis)
11. Crocco, L., Grey, J., and Harrje, D.T., "Theory of Liquid Propellant Rocket Combustion Instability and its Experimental Verification", ARS Journal, Vol. 30, No. 2, February 1960, pp. 159-168.
12. Crocco, L., Harrje, D.T., Reardon, F.H., and Strahle, W.C., "Combustion Instability in Liquid Propellant Rocket Motors", (Thirty-fifth Progress Report), Princeton University Aeronautical Engineering Report No. 216-ii, June 1961.

13. Harrje, D.T. and Crocco, L., "Axial Energy Distribution Studies in a Liquid Propellant Rocket Motor", ICRPG 3rd Combustion Conference, CPIA Publication No. 138, Vol. 1, February 1967, pg. 581.
14. Agosta, V.D., Hammer, S.S., Peschke, W.T., "High Frequency Combustion Instability and Scaling of Liquid Propellant Rocket Motors", Proceedings of the 1st Combustion Instability Conference, 16-20 Nov. 1964, CPIA Publication No. 68, pp. 153-164, Jan. 1965.
15. Nicholls, J.A., Dehora, E.K., Ragland, K.W., Ranger, A.A., "Two Phase Detonations and Drop Shattering Studies", University of Michigan NASA CR-72225, April 1967.
16. Clayton, R.M. and Rogero, R.S., "Experimental Measurements on a Rotating Detonation-Like Wave Observed During Liquid Rocket Resonant Combustion", Jet Propulsion Laboratory Technical Report No. 32-788, 15 August 1965.
17. Williams, R.M. Jr., "Experimental Investigations of Liquid Propellant Combustion Processes Using Streak Photography", Department of Aerospace and Mechanical Sciences Technical Report No. 800, July 1967.
18. Combs, L.P., Hoehn, F.W., Webb, S.R., et al, "Combustion Stability Rating Techniques - Final Report", Rocketdyne AFRPL-TR-66-229, September 1966.
19. Harrje, D.T., "Fundamental Problems of Injector Design", 25th AGARD Colloquium on Advances in Tactical Rocket Propulsion, University of California, San Diego, California, April, 1965.
20. Valentine, R.S., Dean, L.E., and Pieper, J.L., "An Improved Method for Rocket Performance Prediction", Aerojet-General Corp., Sacramento, California.
21. Rupe, J.H., "Experimental Studies of the Hydrodynamics of Liquid Propellant Injection, External Publication No. 388, Jet Propulsion Laboratory, June 7, 1957.
22. Guttman, I., Wilks, S.S., Introductory Engineering Statistics, John Wiley & Sons, Inc., New York, 1965, pp 109-114.
23. Housner, G.W., Hudson, D.D., Applied Mechanics Dynamics, D. Van Nostrand Co., Inc., Princeton, N.J., 1959, pp 88-92.
24. Jaivin, G.I., Clayton, R.M., and Rupe, J.H., "An Experimental Correlation of the Non-reactive Properties of Injection Schemes and Combustion Effects in a Liquid-Propellant Rocket Engine: Part IV", Jet Propulsion Laboratory, Pasadena, California.

25. Newman, J.A., "A Preliminary Study of the Effects of Vaporization and Transverse Oscillations on Liquid Jet Breakup", Department of Aerospace and Mechanical Sciences Technical Report No. 785, July 1967 (NASA CR-72258).
26. Chester, W., "Resonant Oscillations in Closed Tubes", Journal of Fluid Mechanics, 18 (1964).
27. Chu, B.T., "Analysis of a Self-Sustained Nonlinear Vibration in a Pipe Containing a Heater", AFOSR-TN-1755, September 1961.
28. Priem, R.J. and Heidmann, M.F., "Propellant Vaporization as a Design Criterion for Rocket-Engine Combustion Chambers", NASA TR R-67, 1960.
29. Priem, R.J. and Guentert, D.C., "Combustion Instability Limits Determined by a Nonlinear Theory and a One-Dimensional Model", NASA TN D-1409, 1962.
30. Heidmann, M.F. and Wieber, P.R., "An Analysis of n-Heptane Vaporization in an Unstable Combustor with Traveling Transverse Oscillations", NASA TN D-3424, 1966.

JP21 P57 GT



Streak photograph of pulse

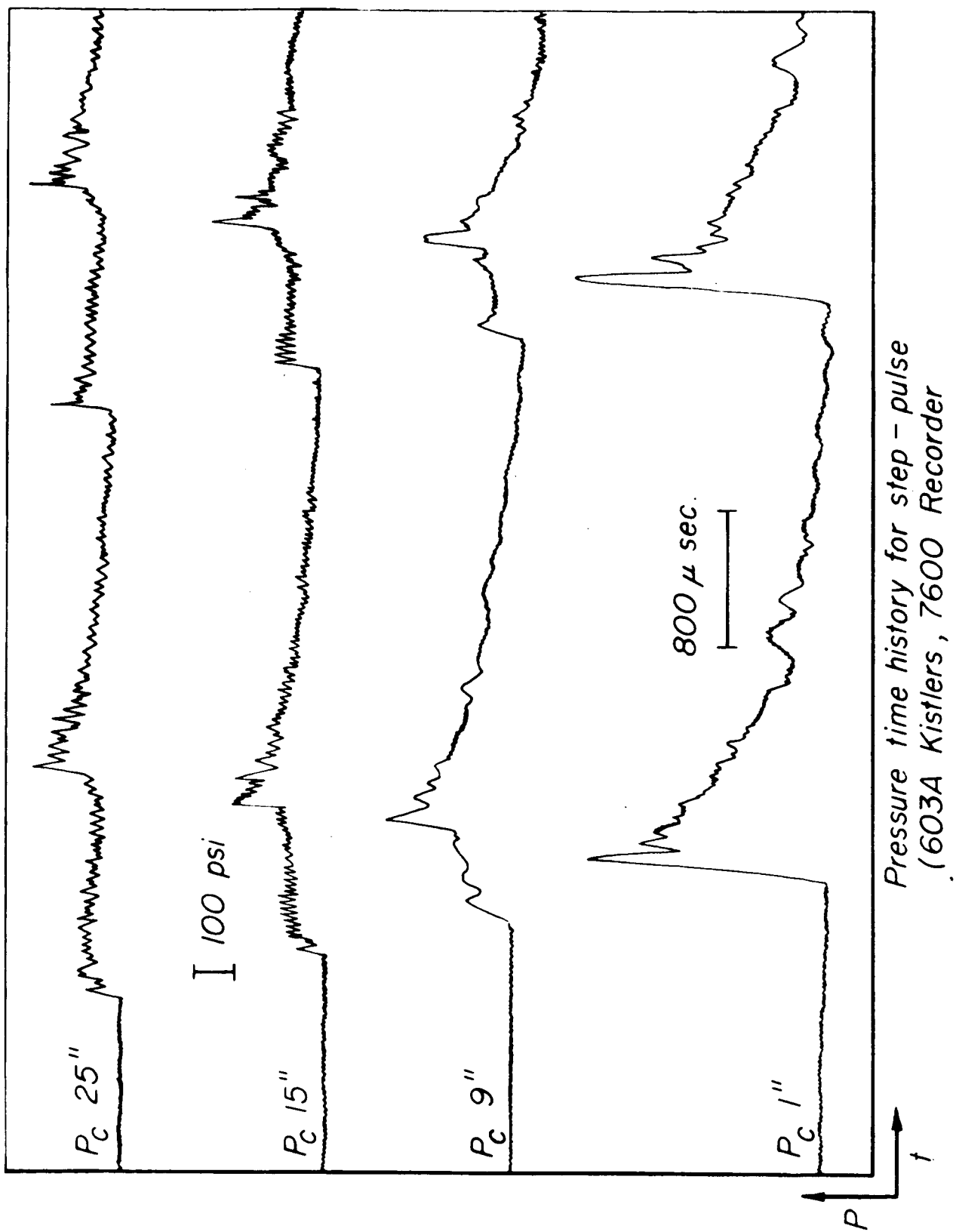


Figure 2

Type II, 4x4

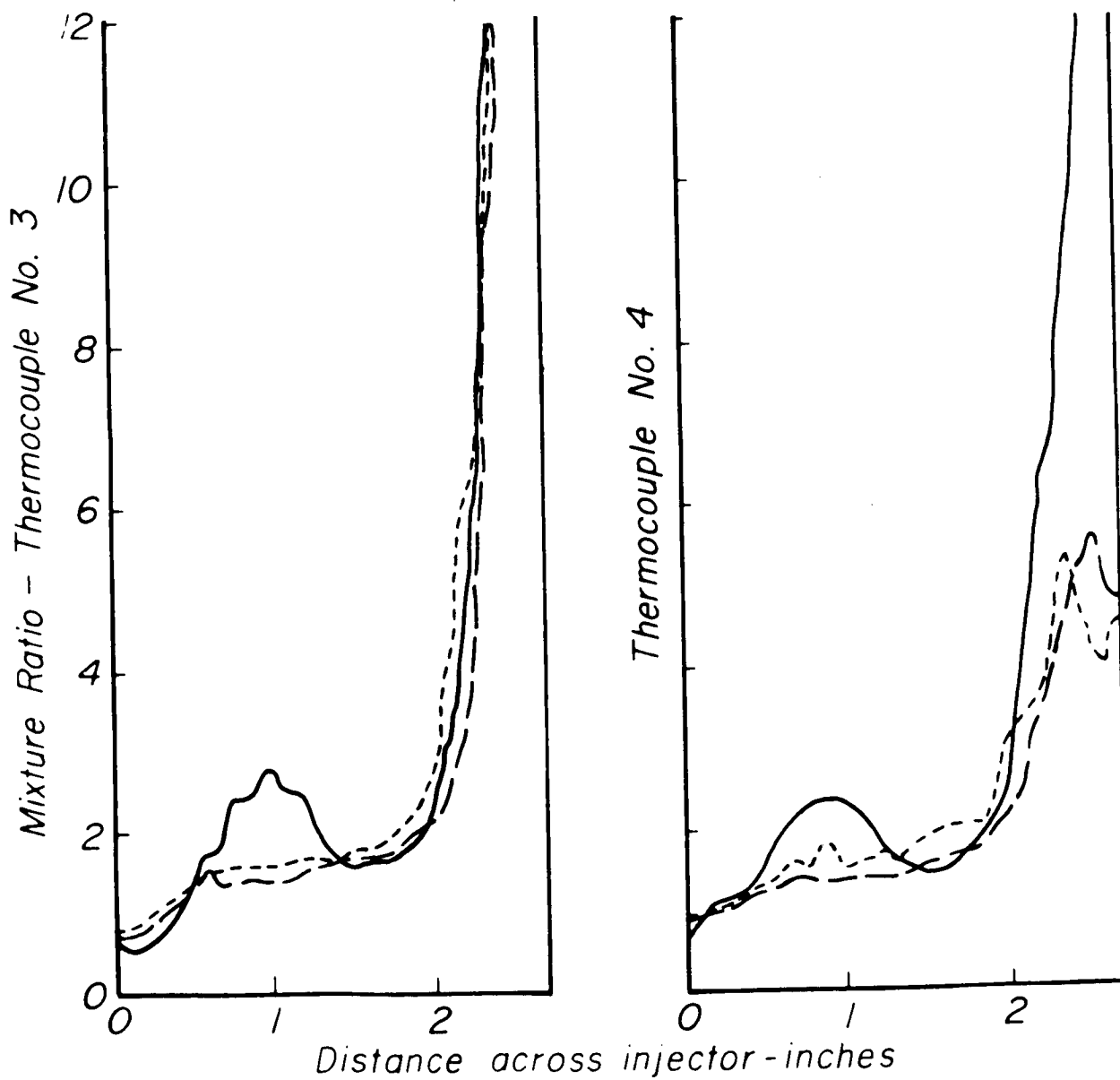
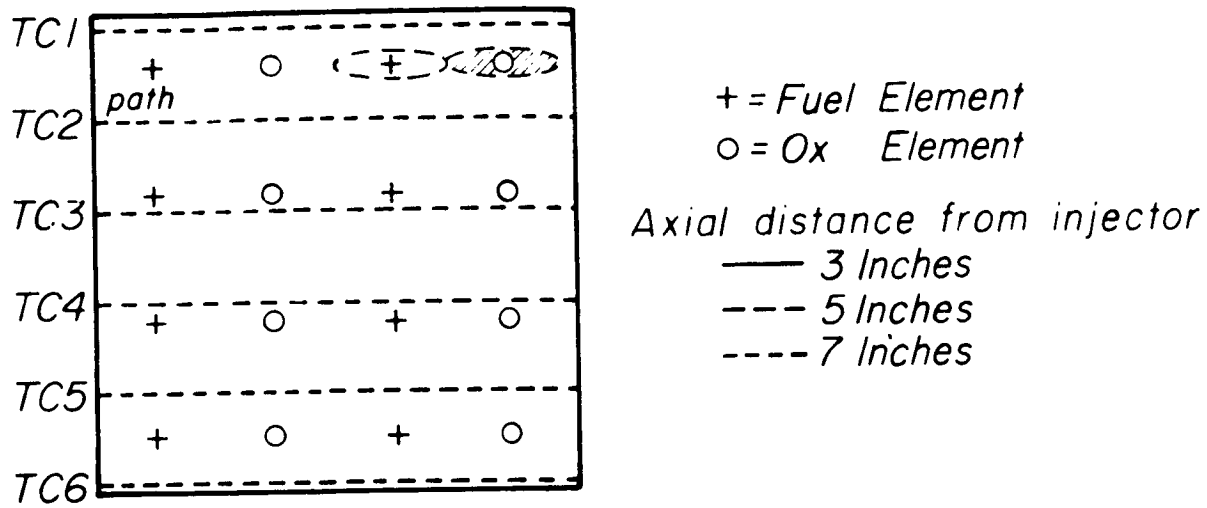


Figure 3

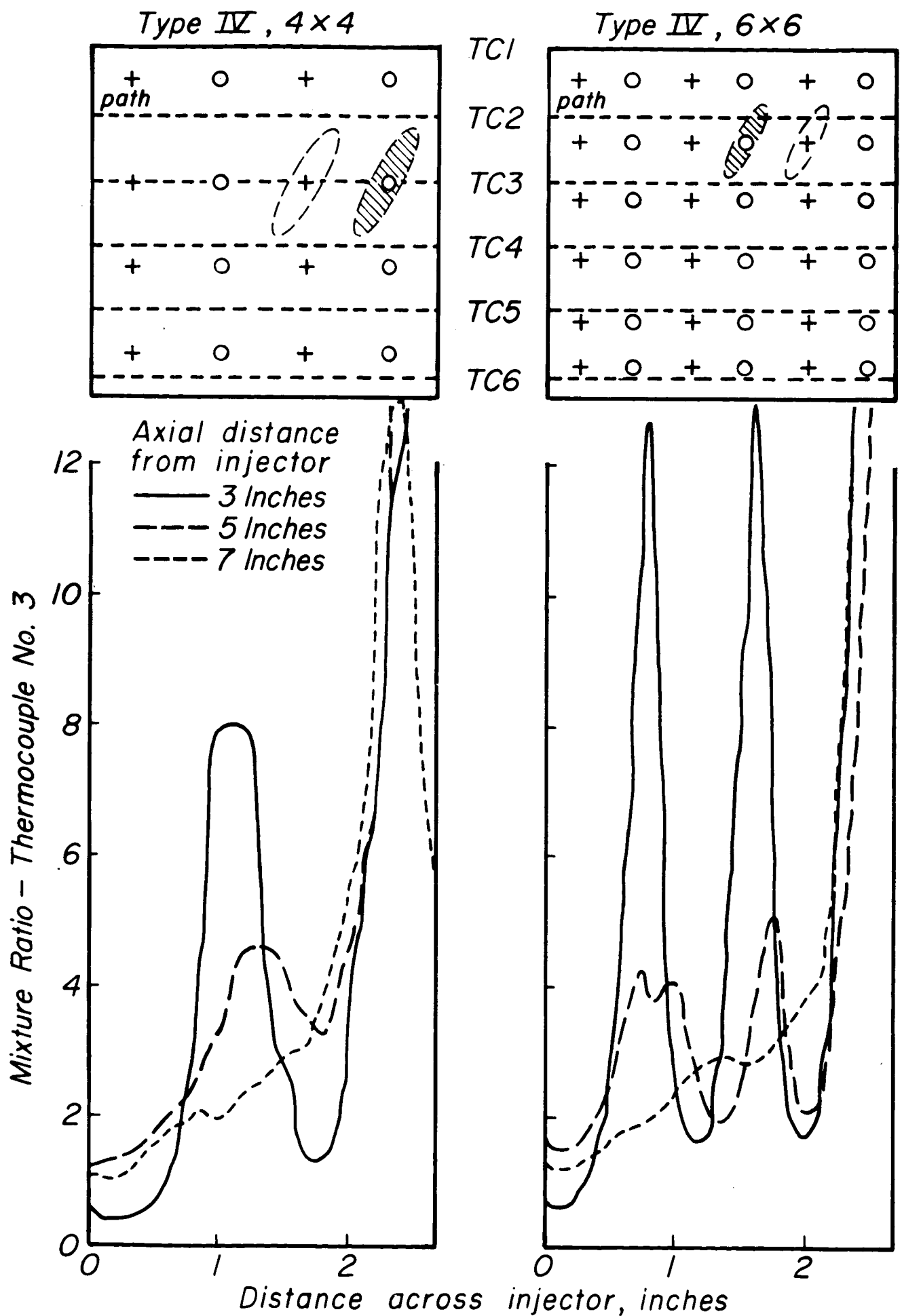
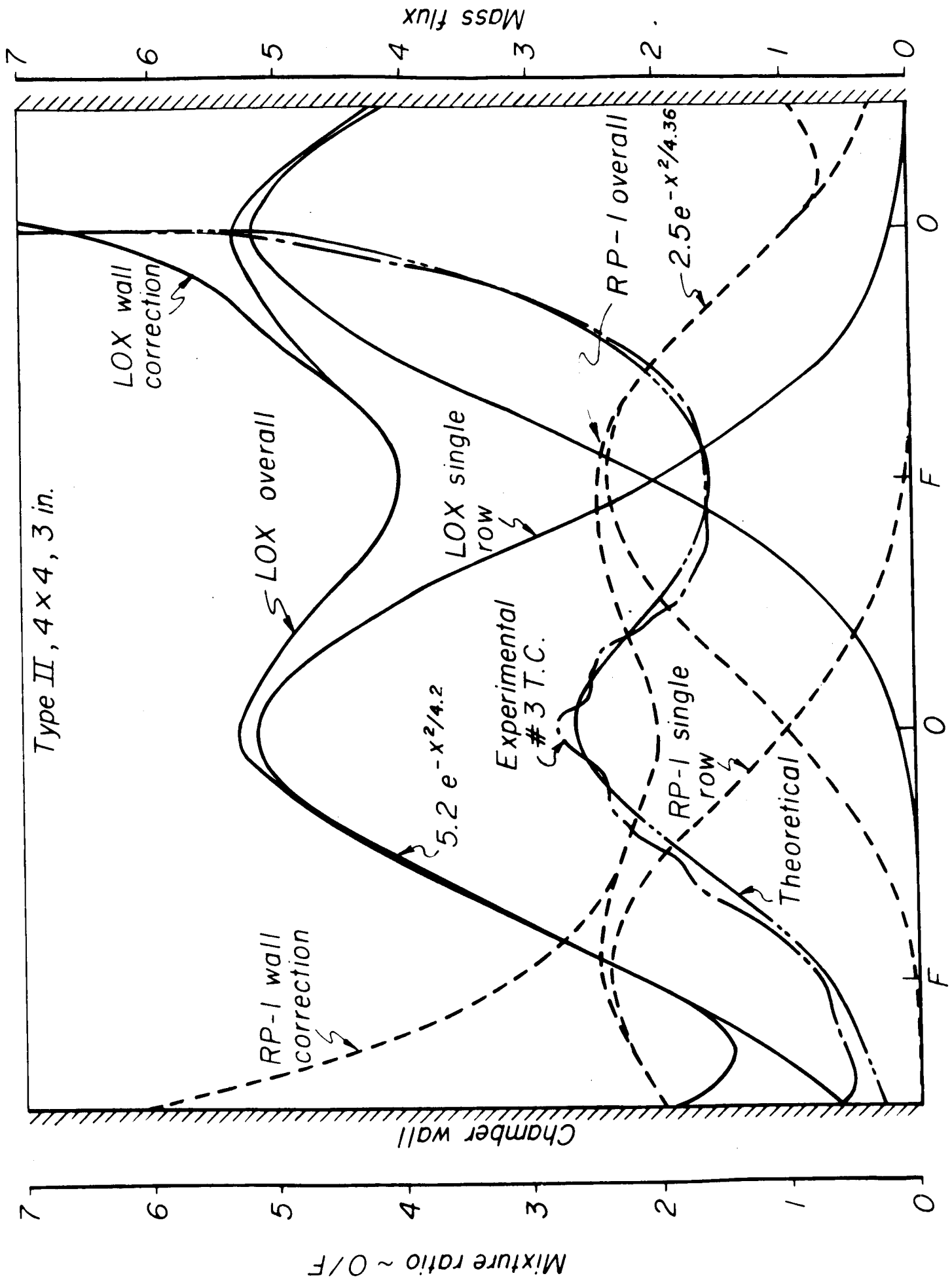


Figure 4



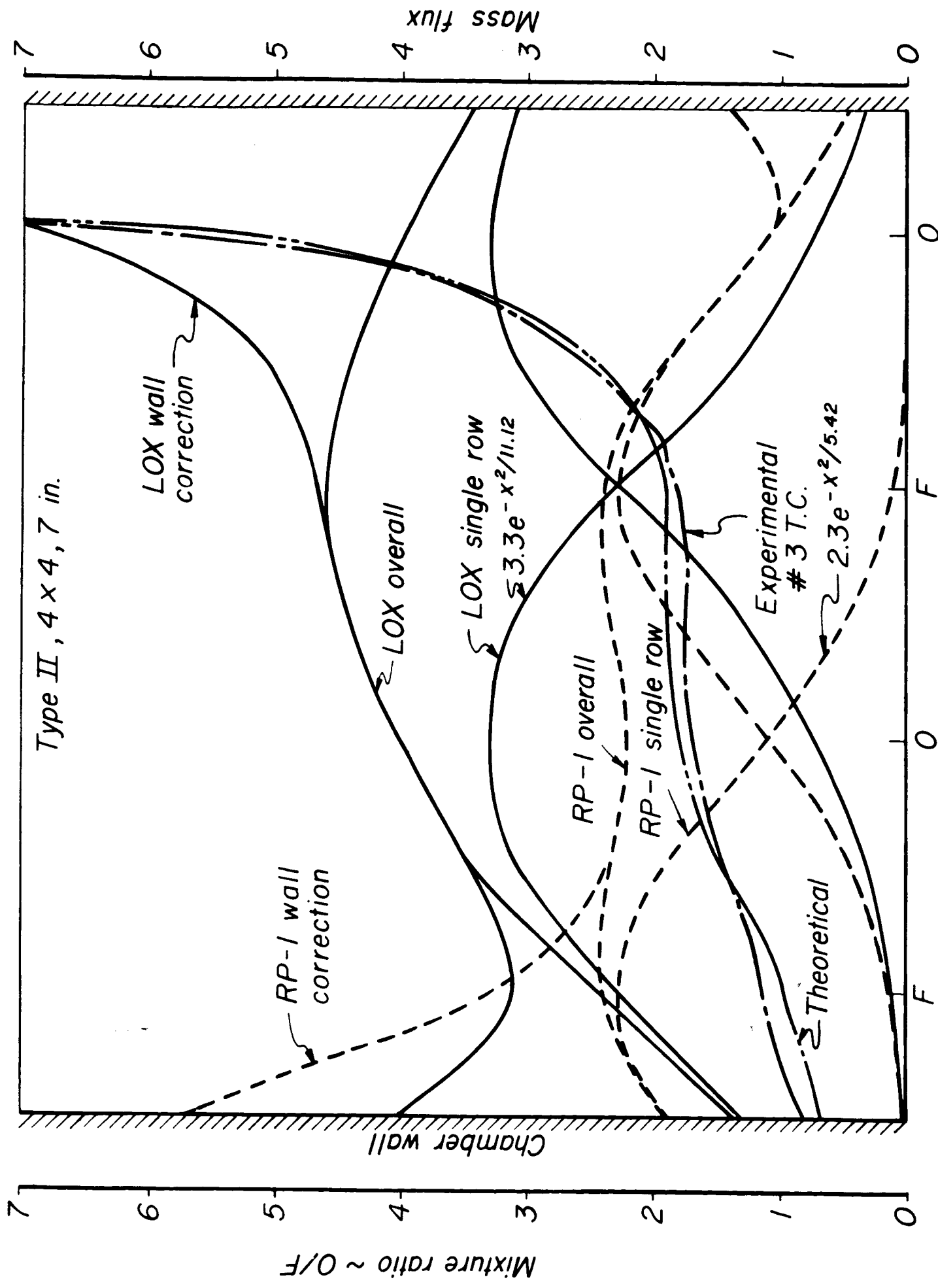


Figure 6

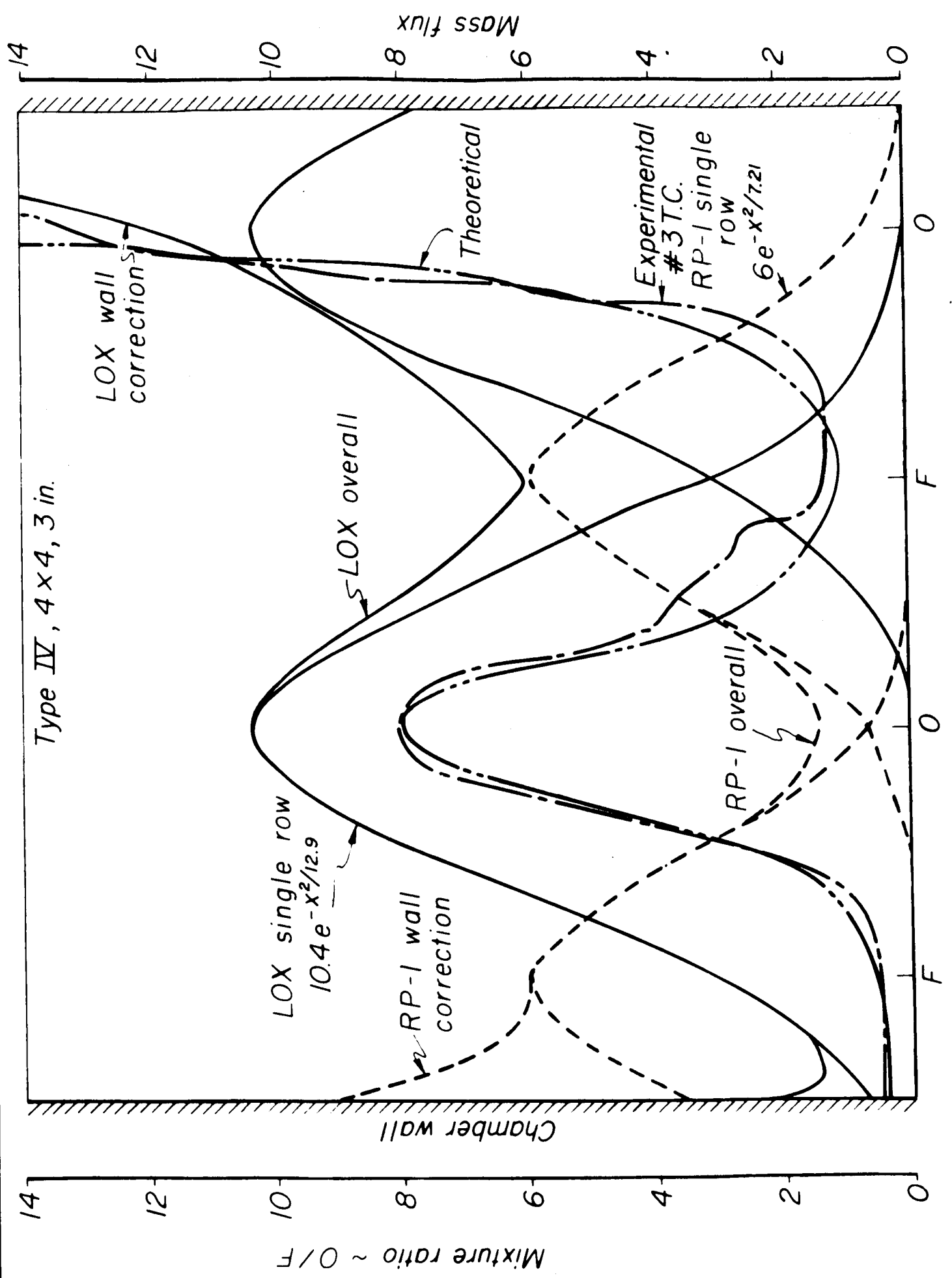


Figure 7

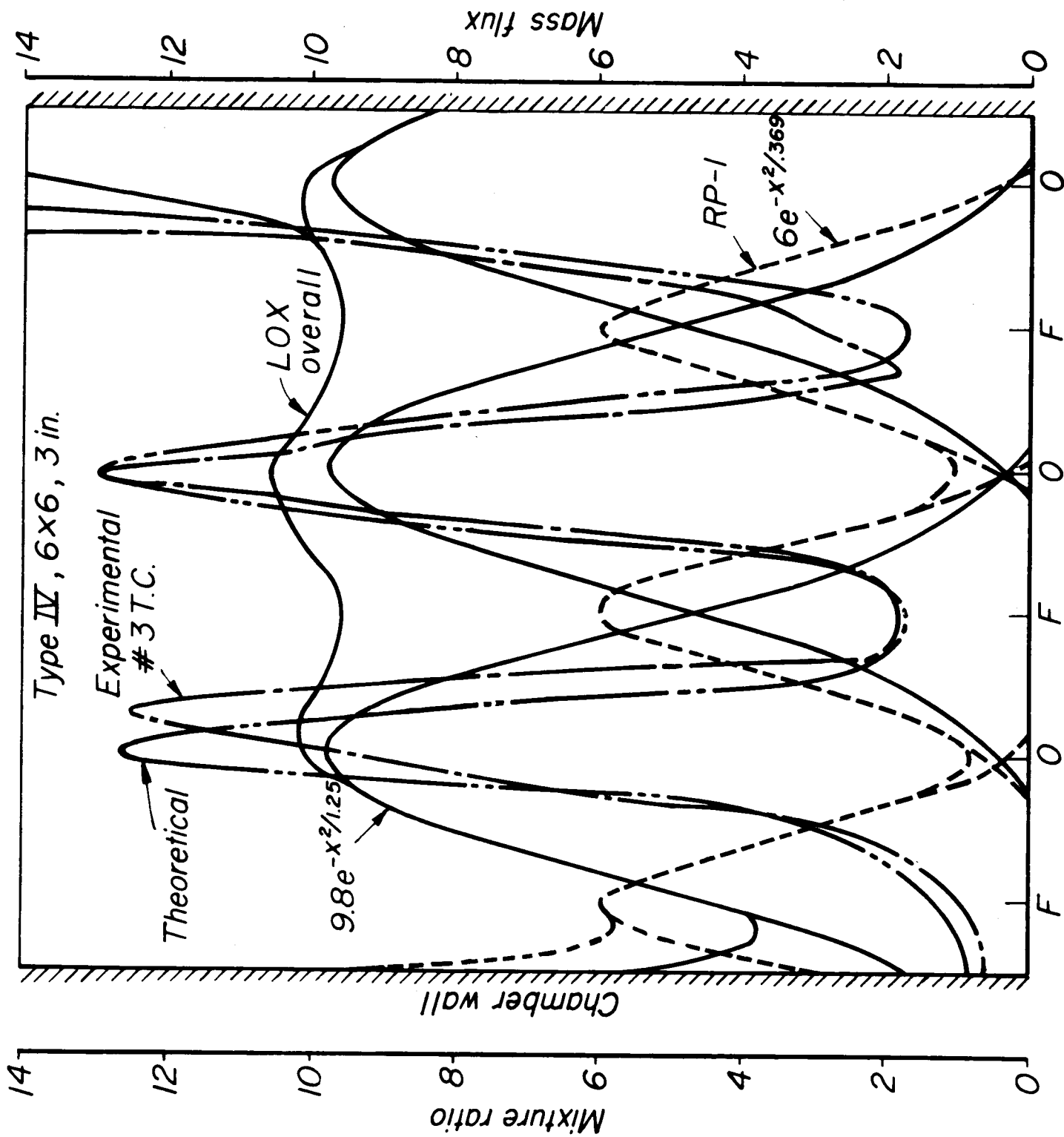
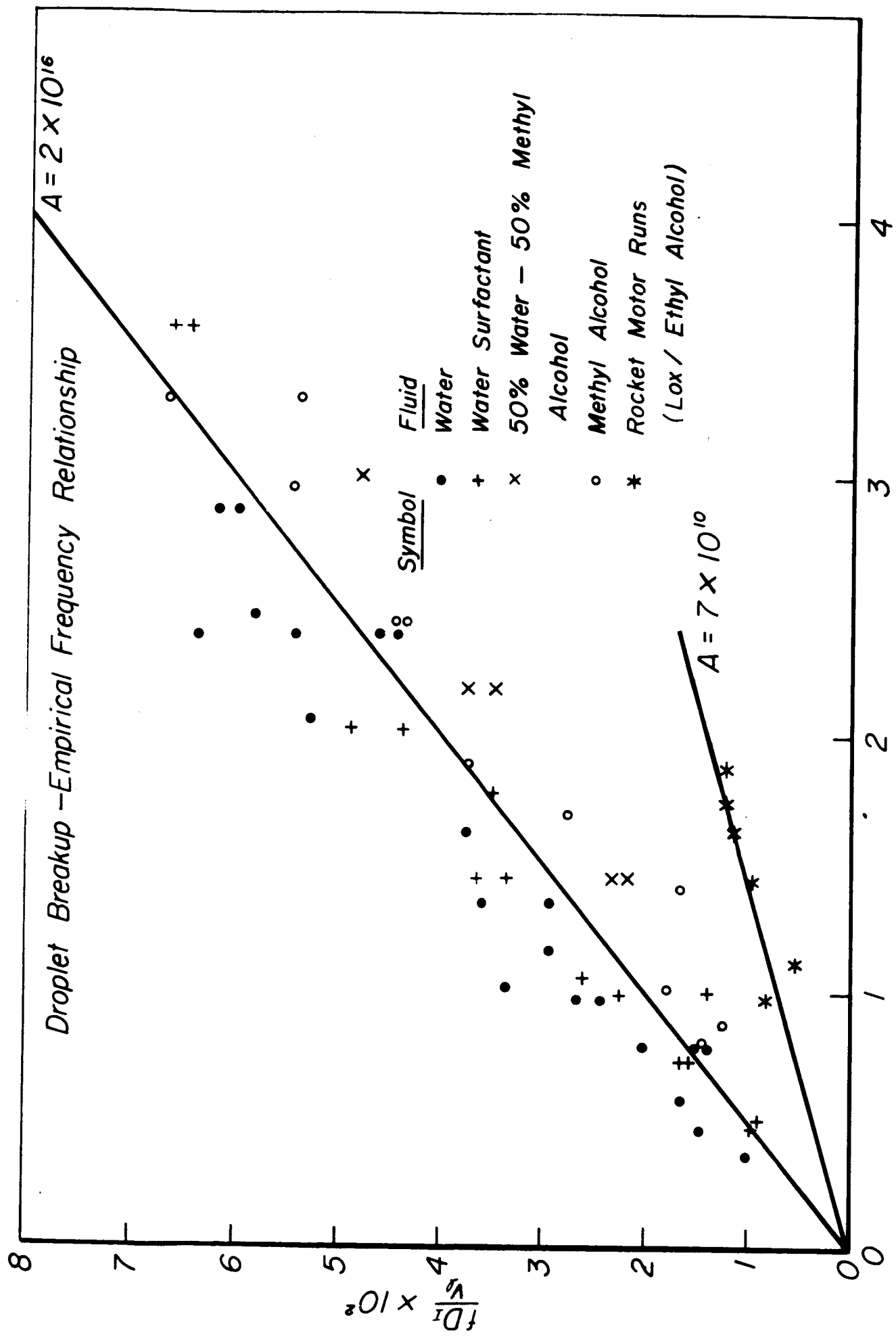


Figure 8



$$\left(\frac{\mu_g}{\mu_l} \right)^{2.9} \left(\frac{\sigma_l}{D_I \rho_l} v_l^2 \right)^{-2.25} \left(\frac{\mu_l}{D_I \rho_l v_l} \right)^{3.25} \left(\frac{\rho_l v_l^2}{p_c} \right)^{0.8} \times 10^{18} \text{ (Hot Runs } \times 10^{13} \text{)}$$

Figure 10

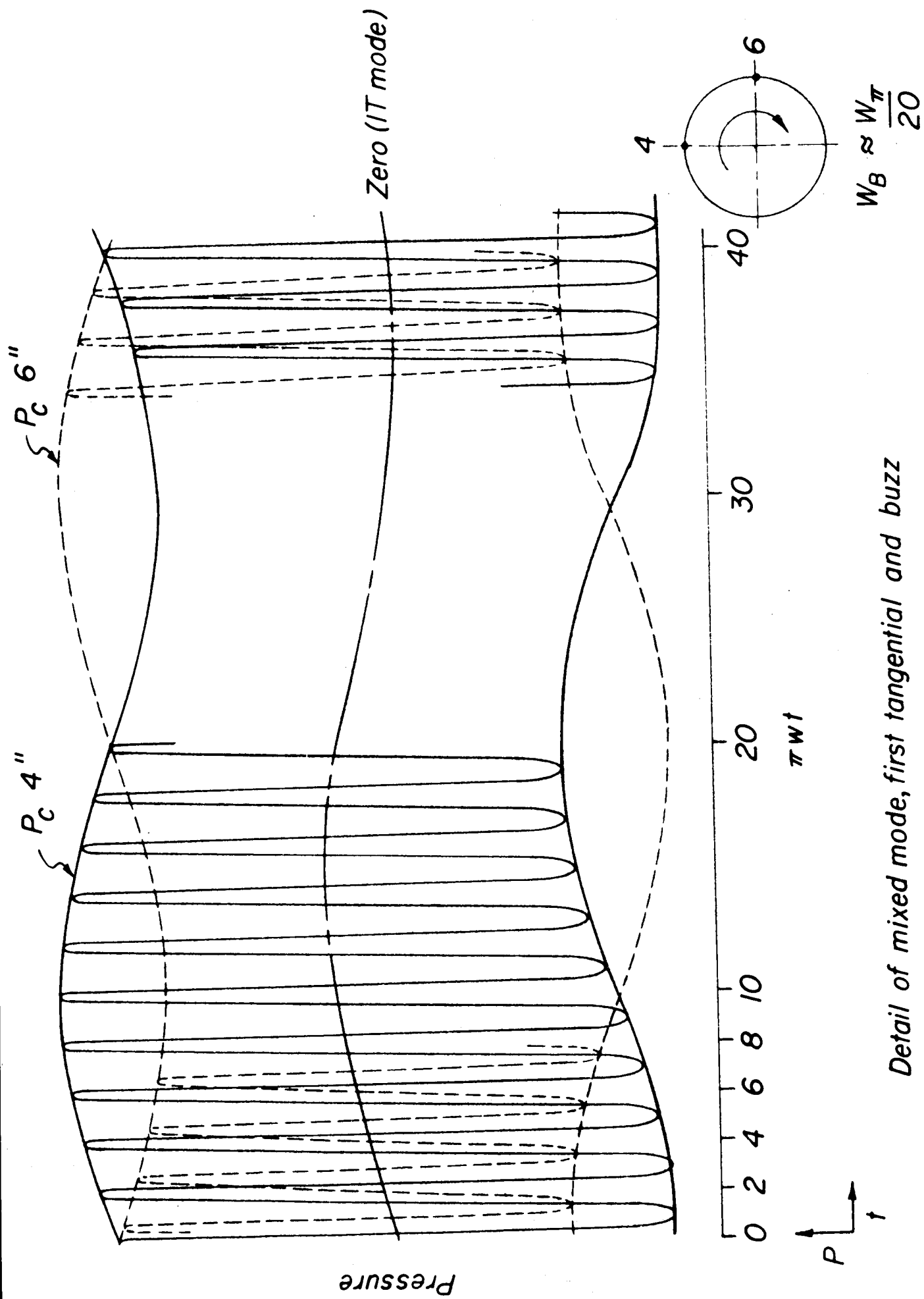
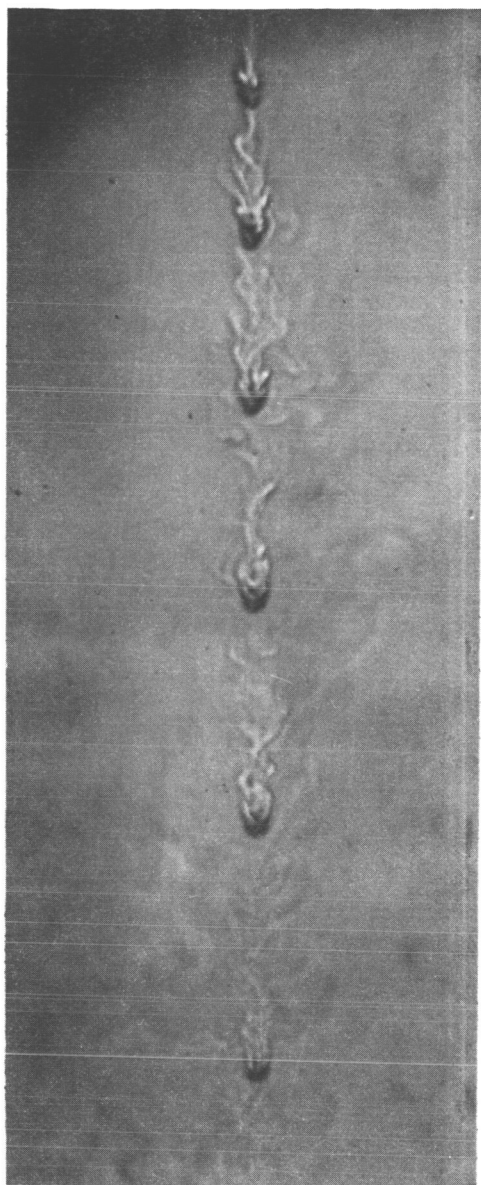
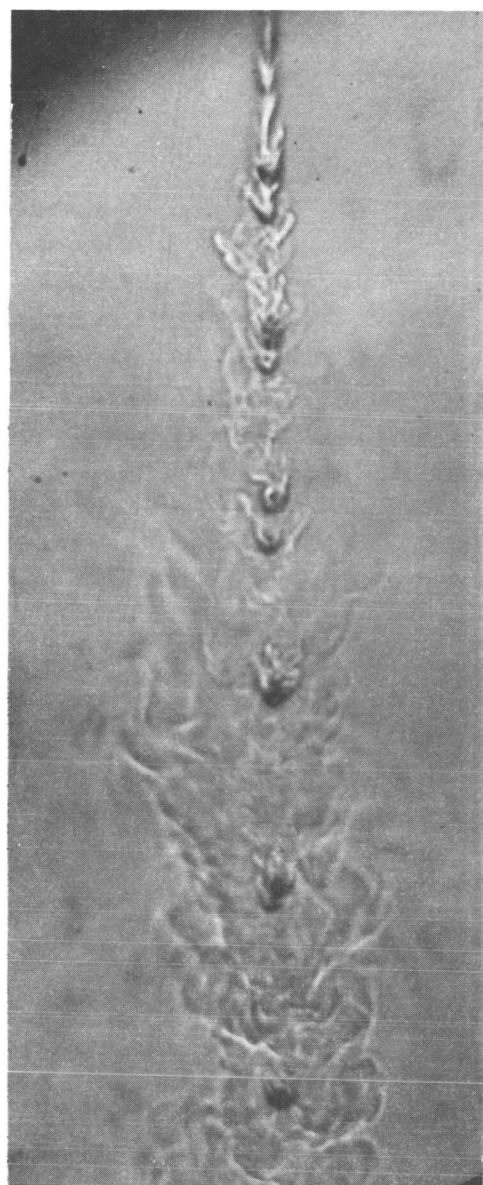


Figure 11



Stable

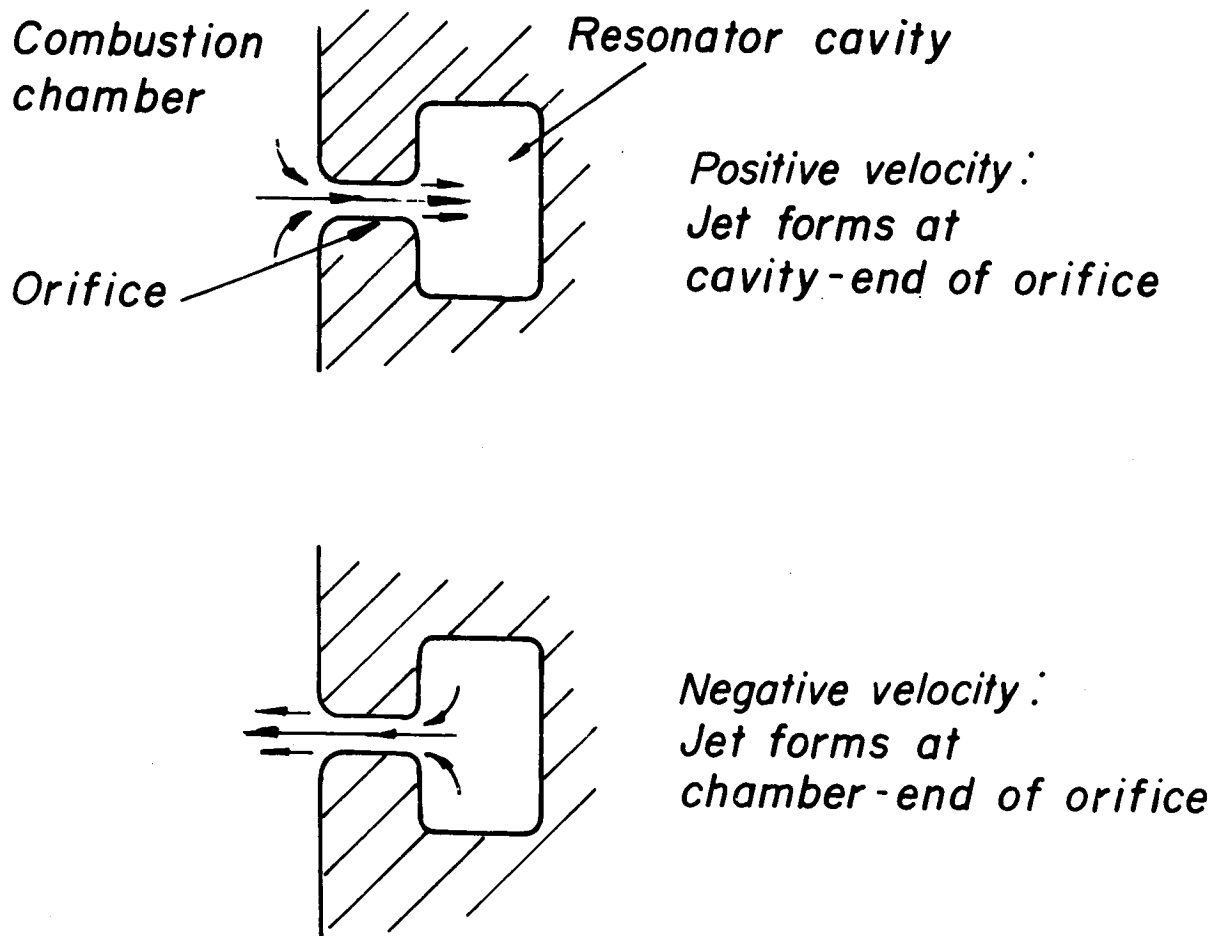


*At velocity maximum
in 1T standing
mode oscillations
($\tilde{V} \approx 50$ ft/sec , @ 900 cps)*

Photographs of droplet vapor sheaths

Figure 12

Nonlinear model of acoustic liner operation



Entrance losses are neglected

Exit jet losses are 100% of kinetic energy

JP21-R4156-66

Figure 13

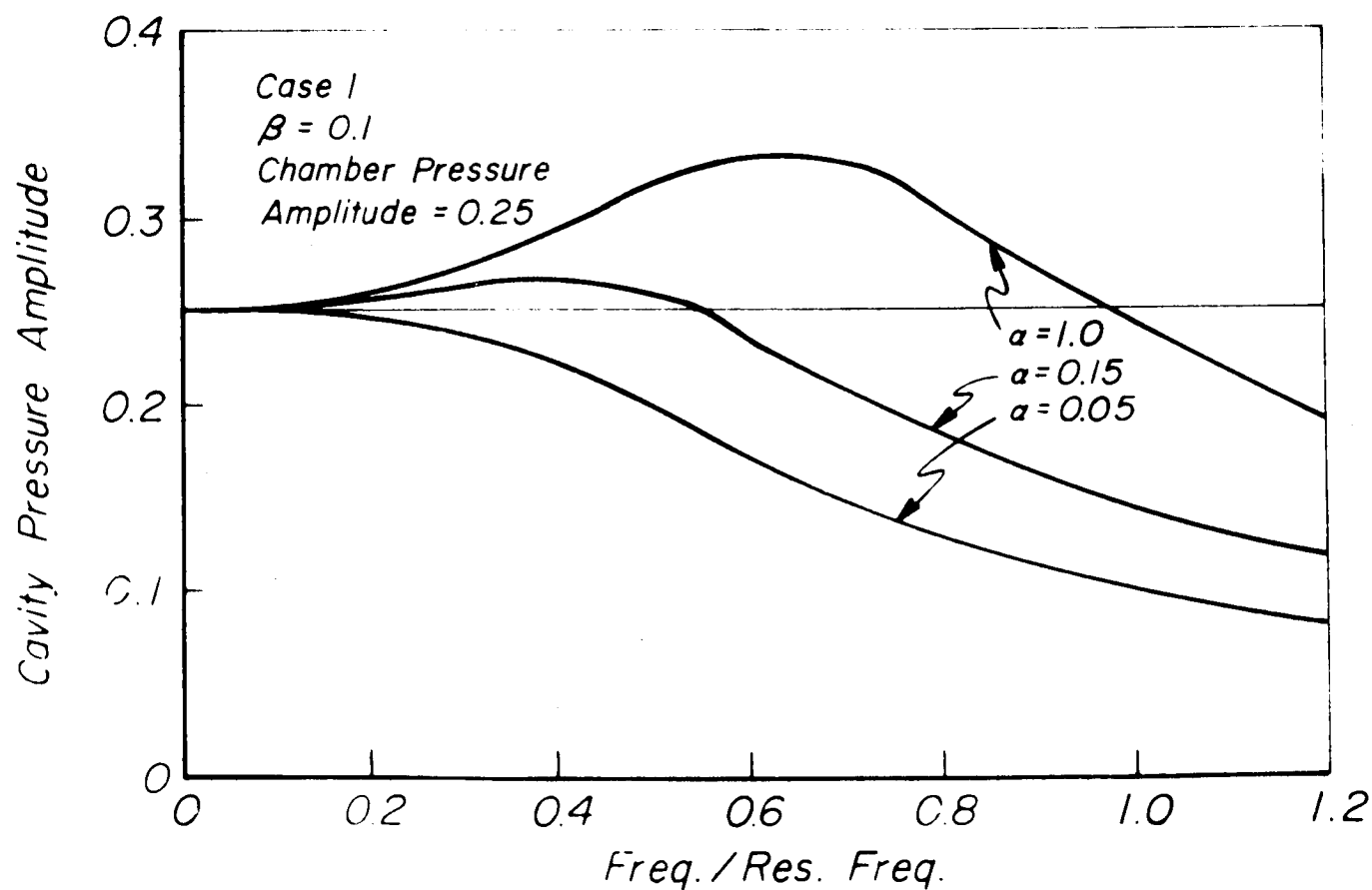
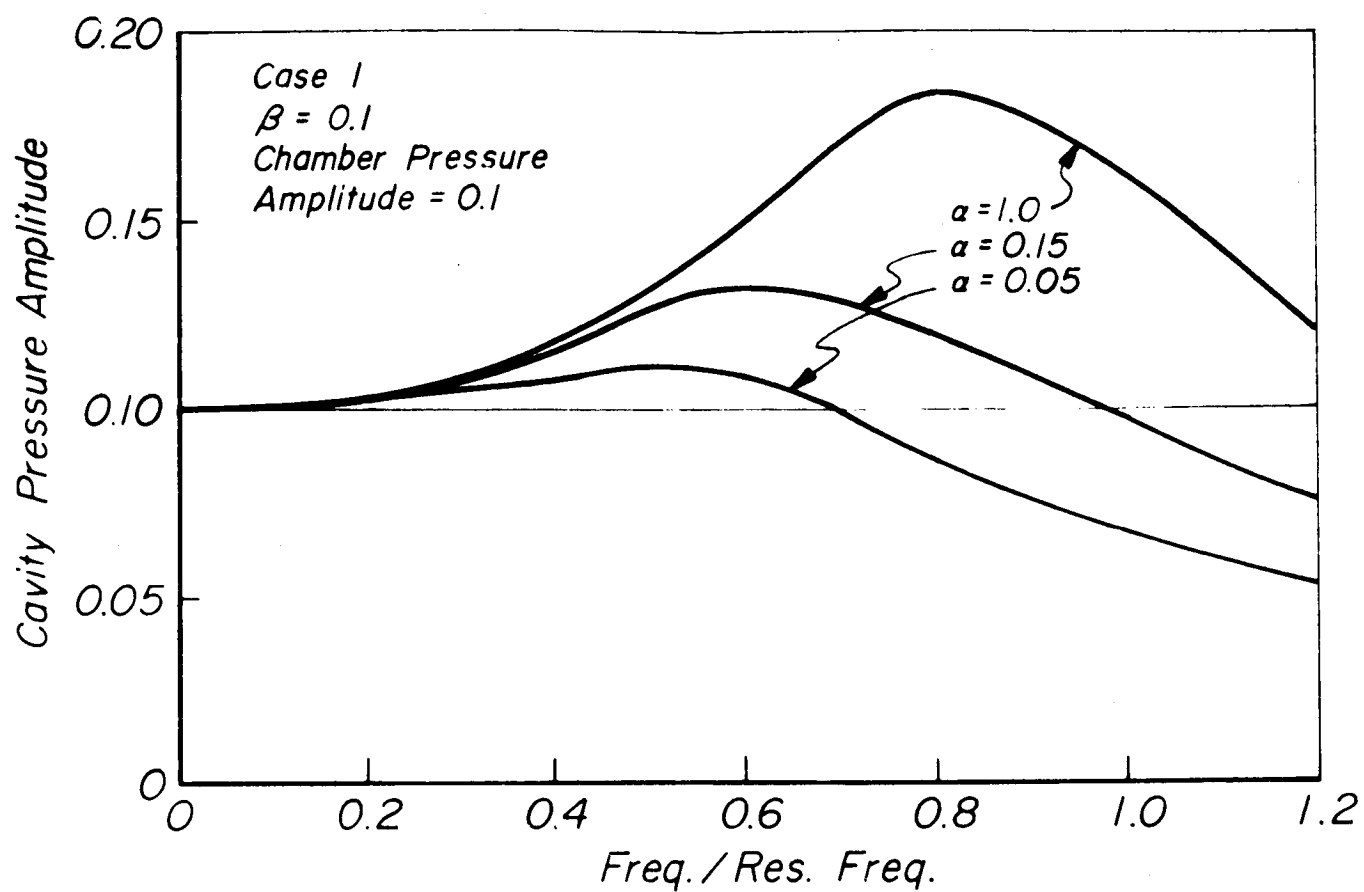


Figure 14

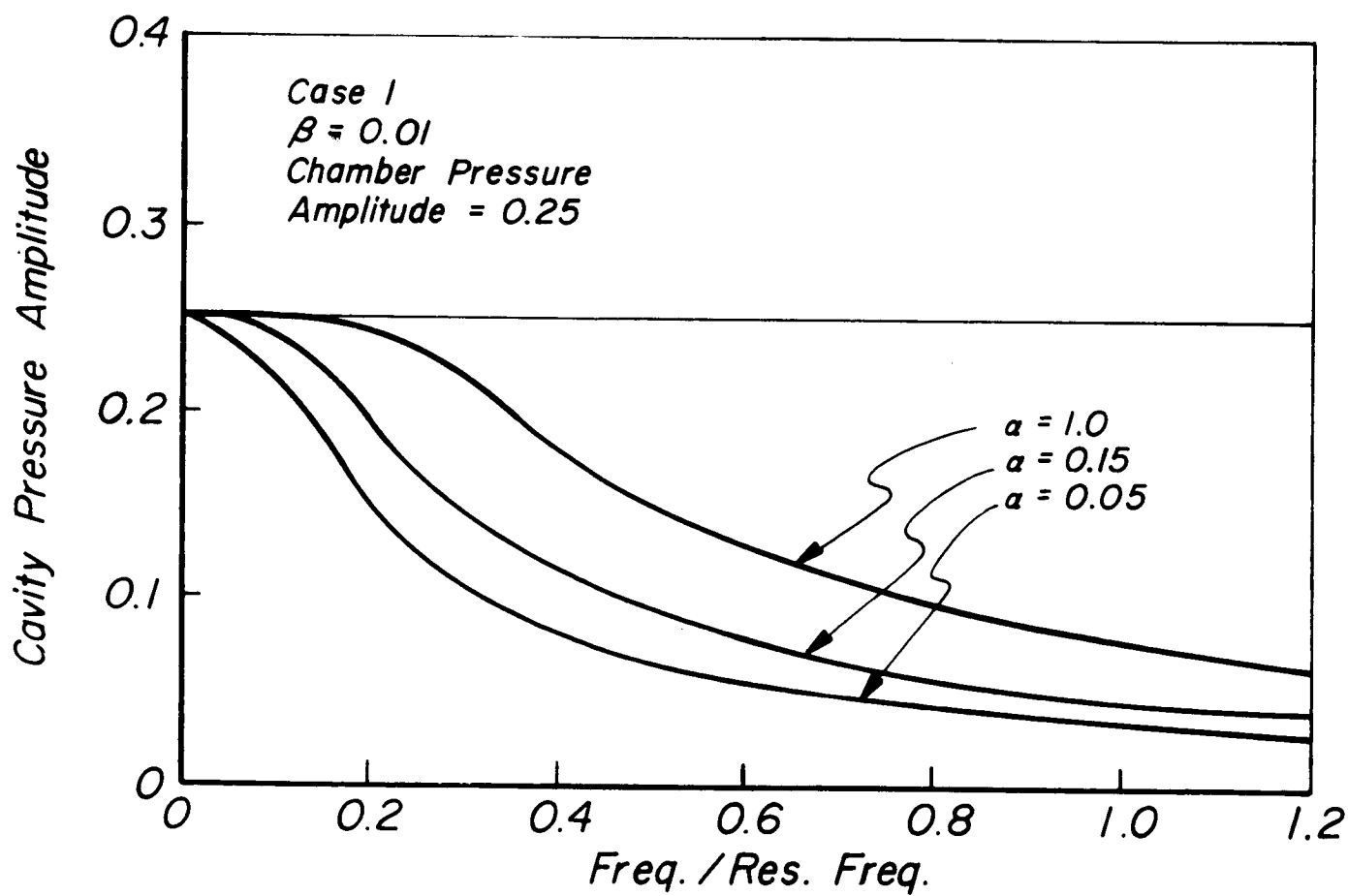
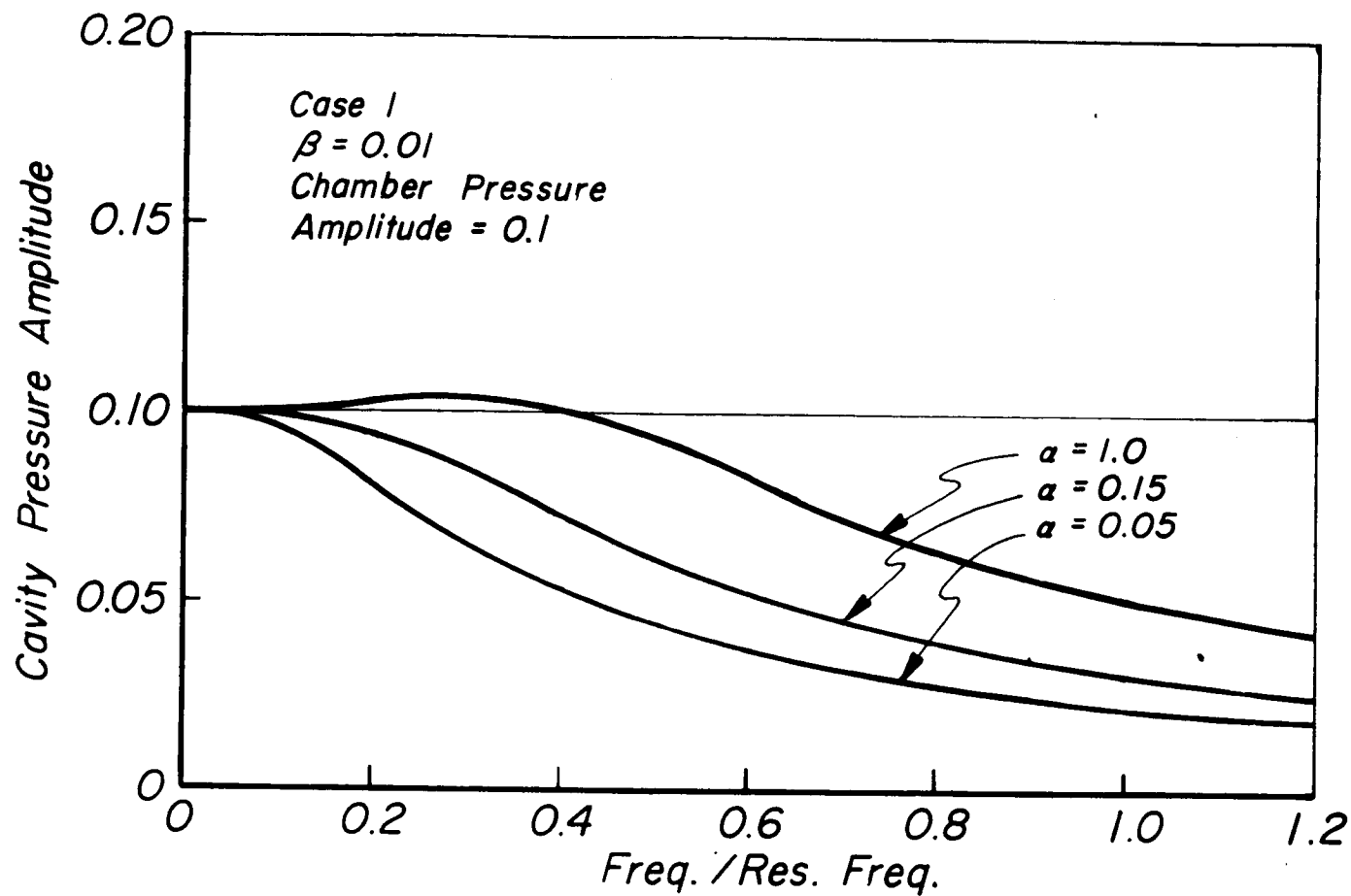


Figure 15

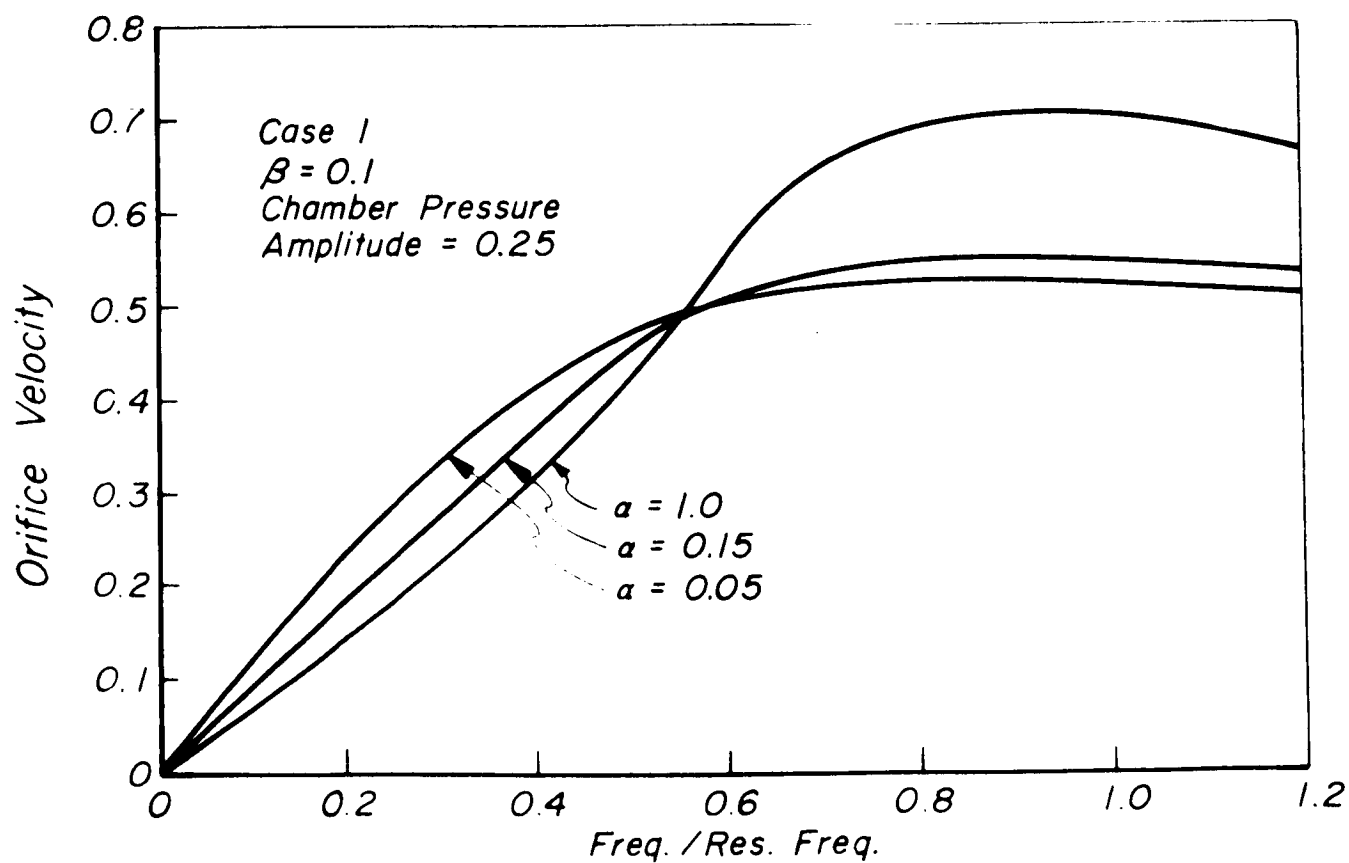
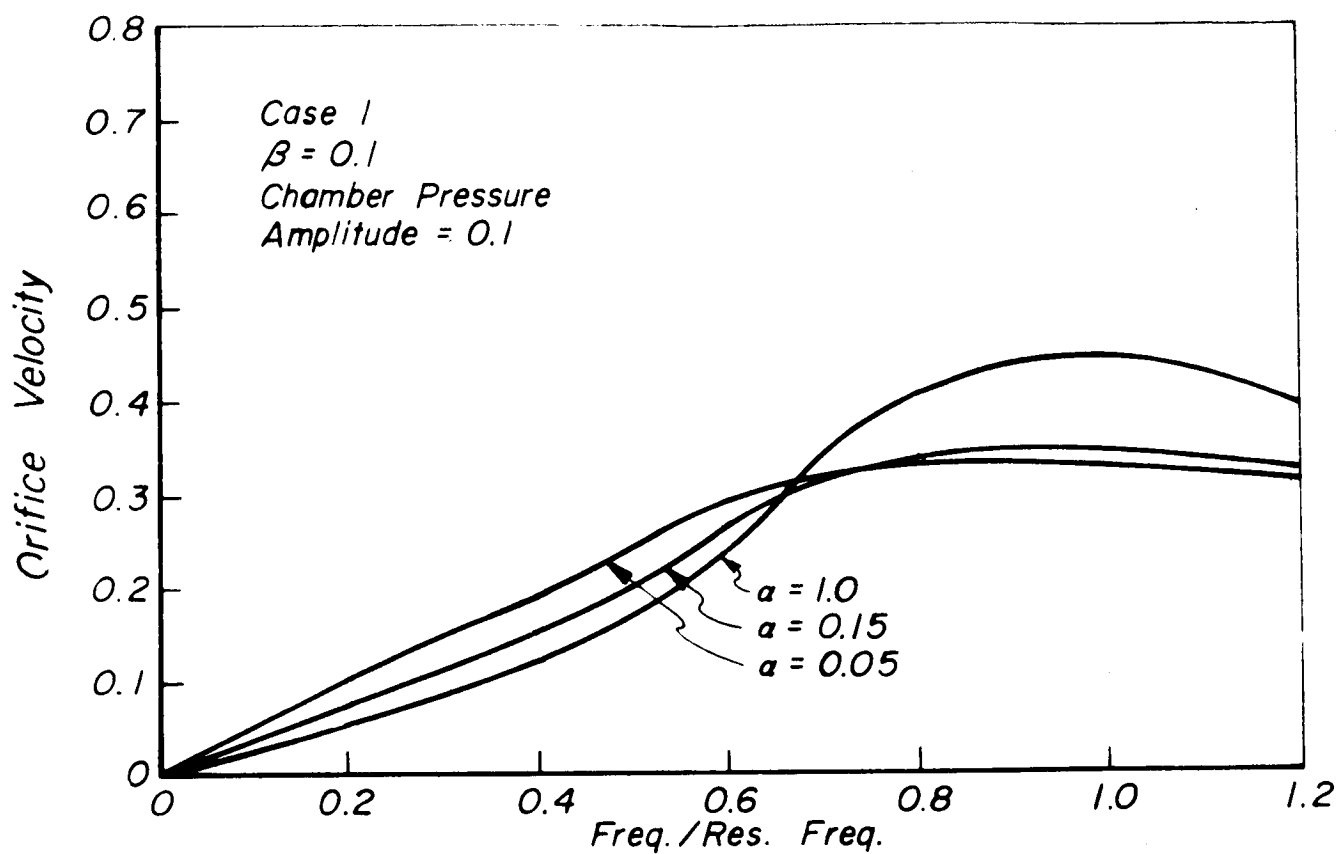


Figure 16

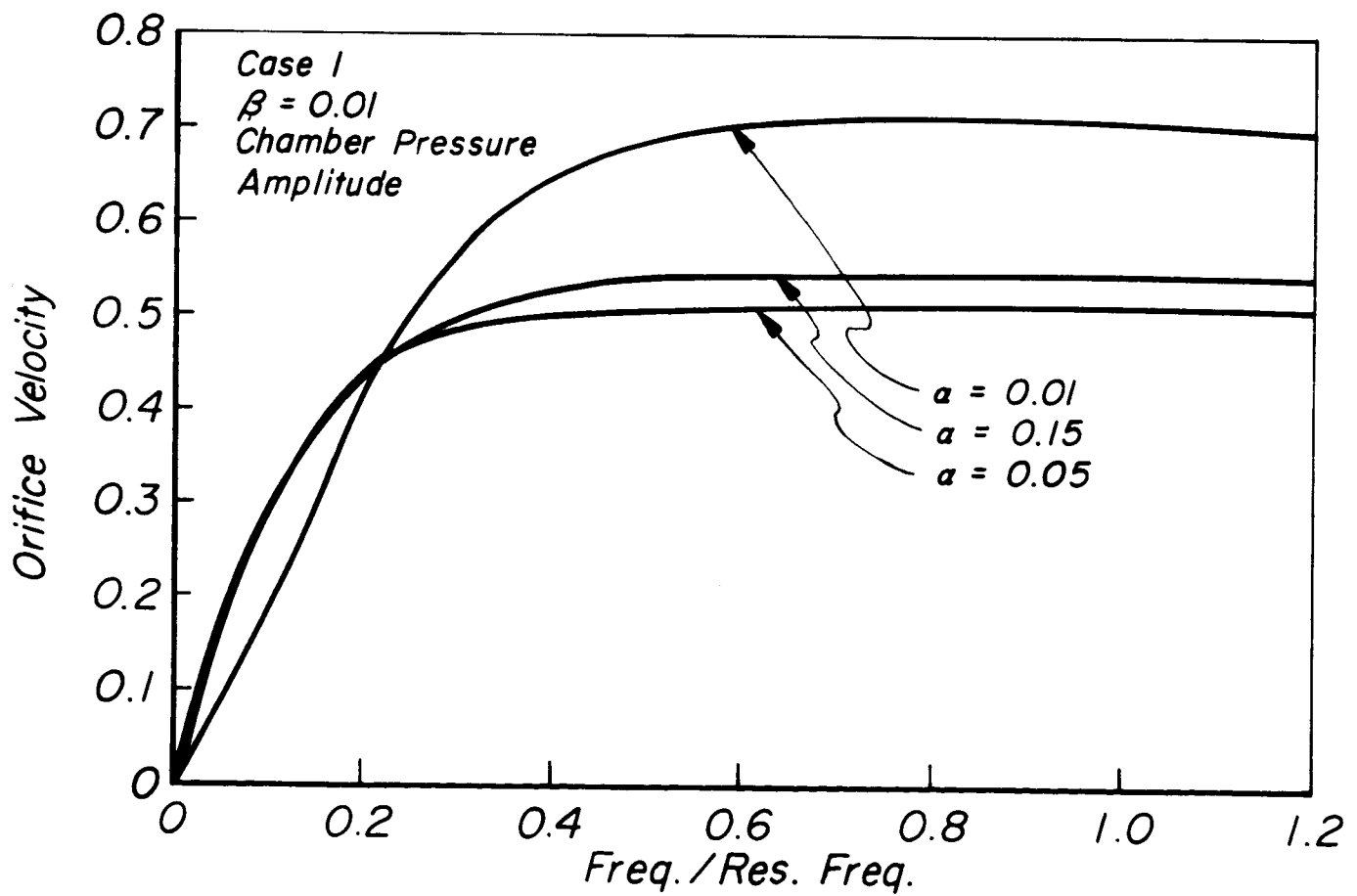
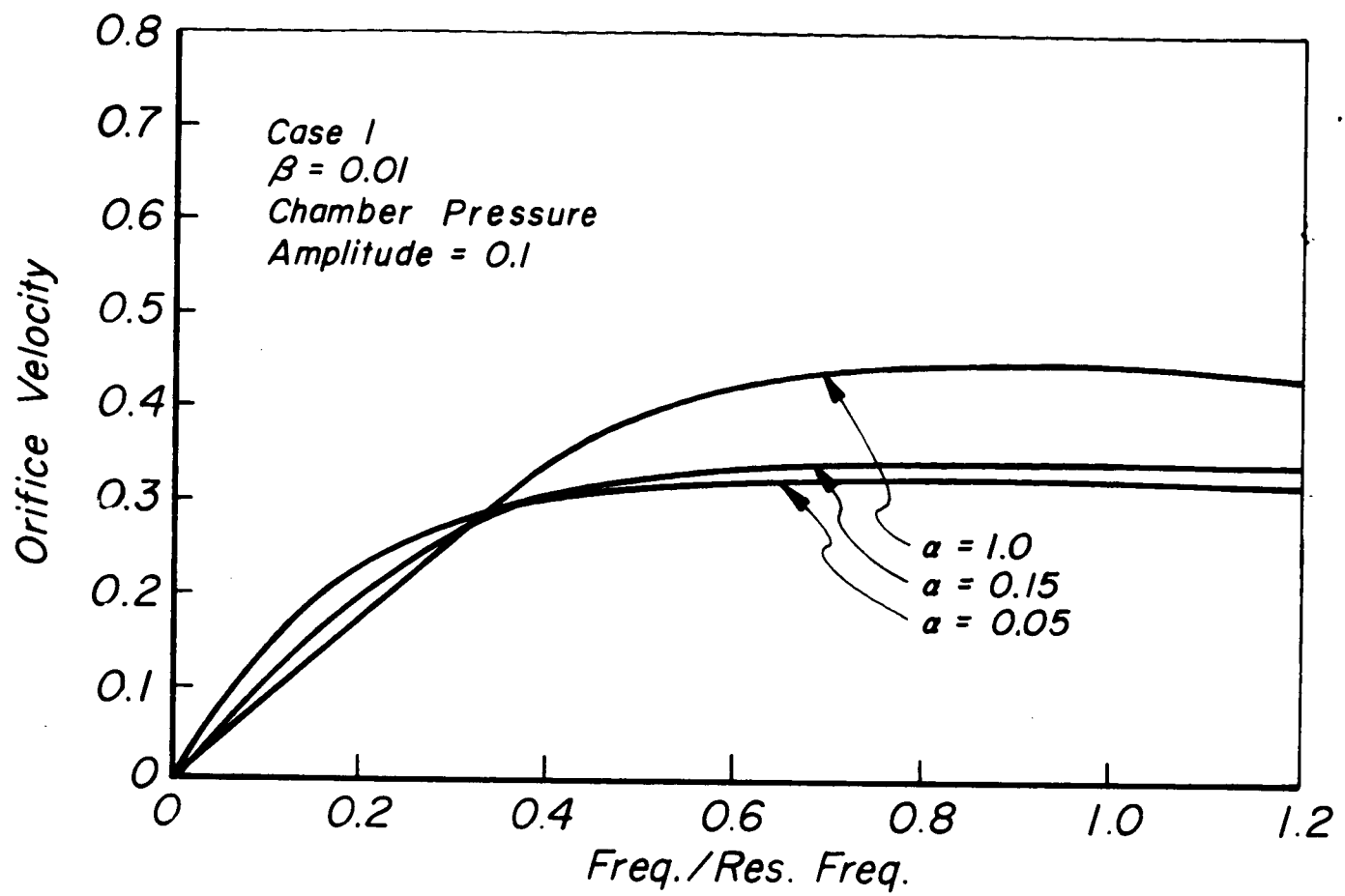


Figure 17

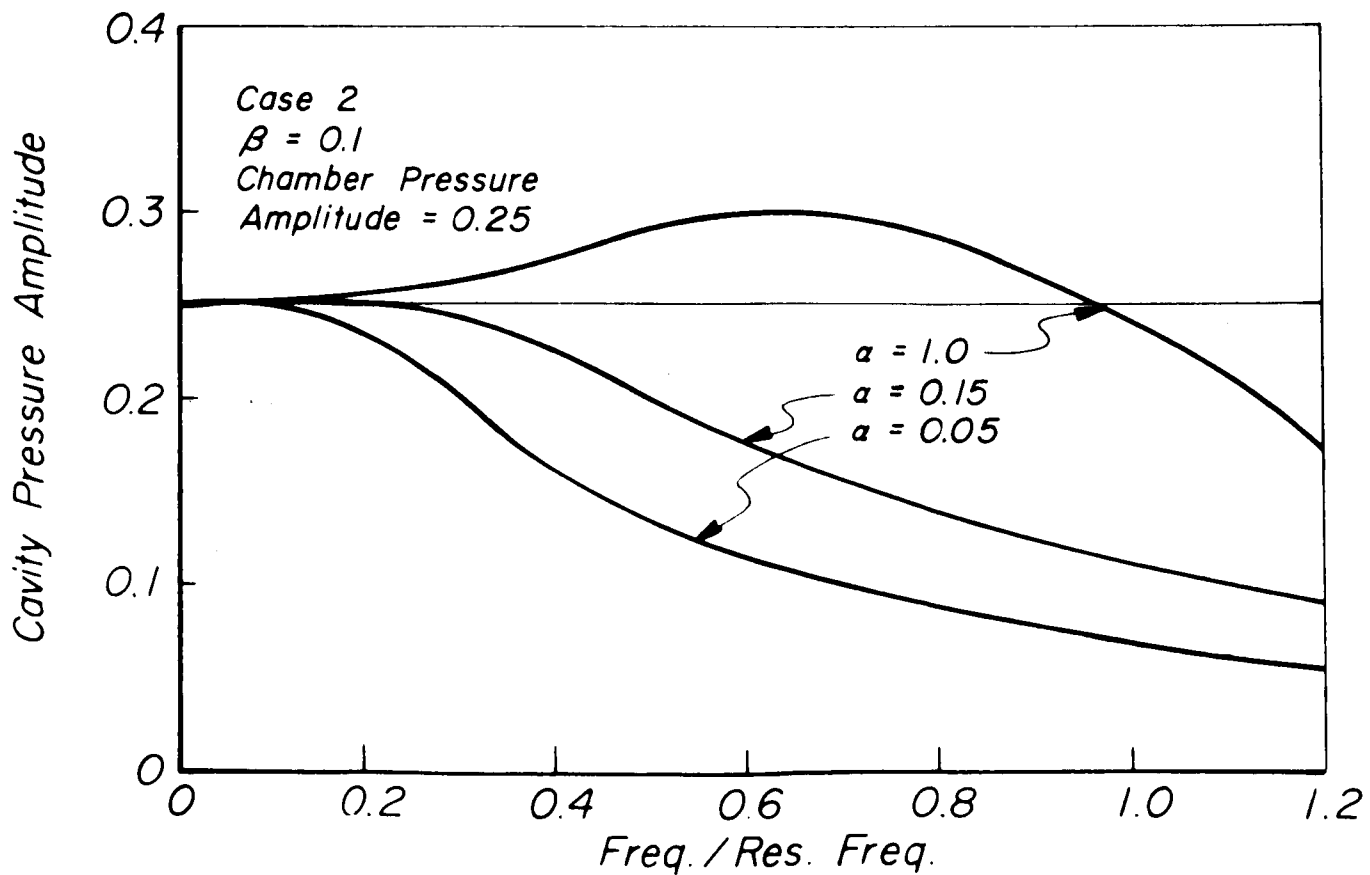
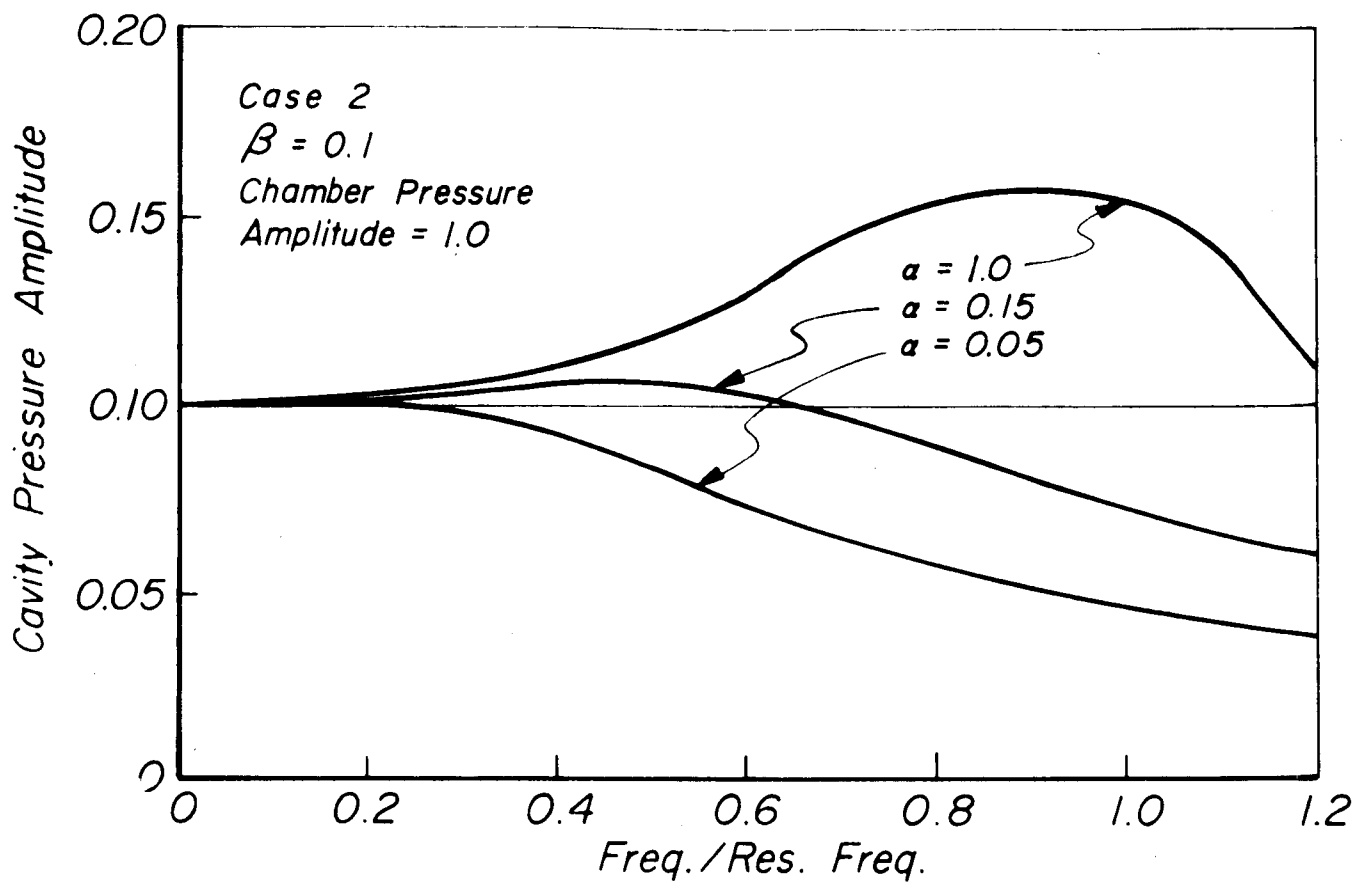


Figure 18

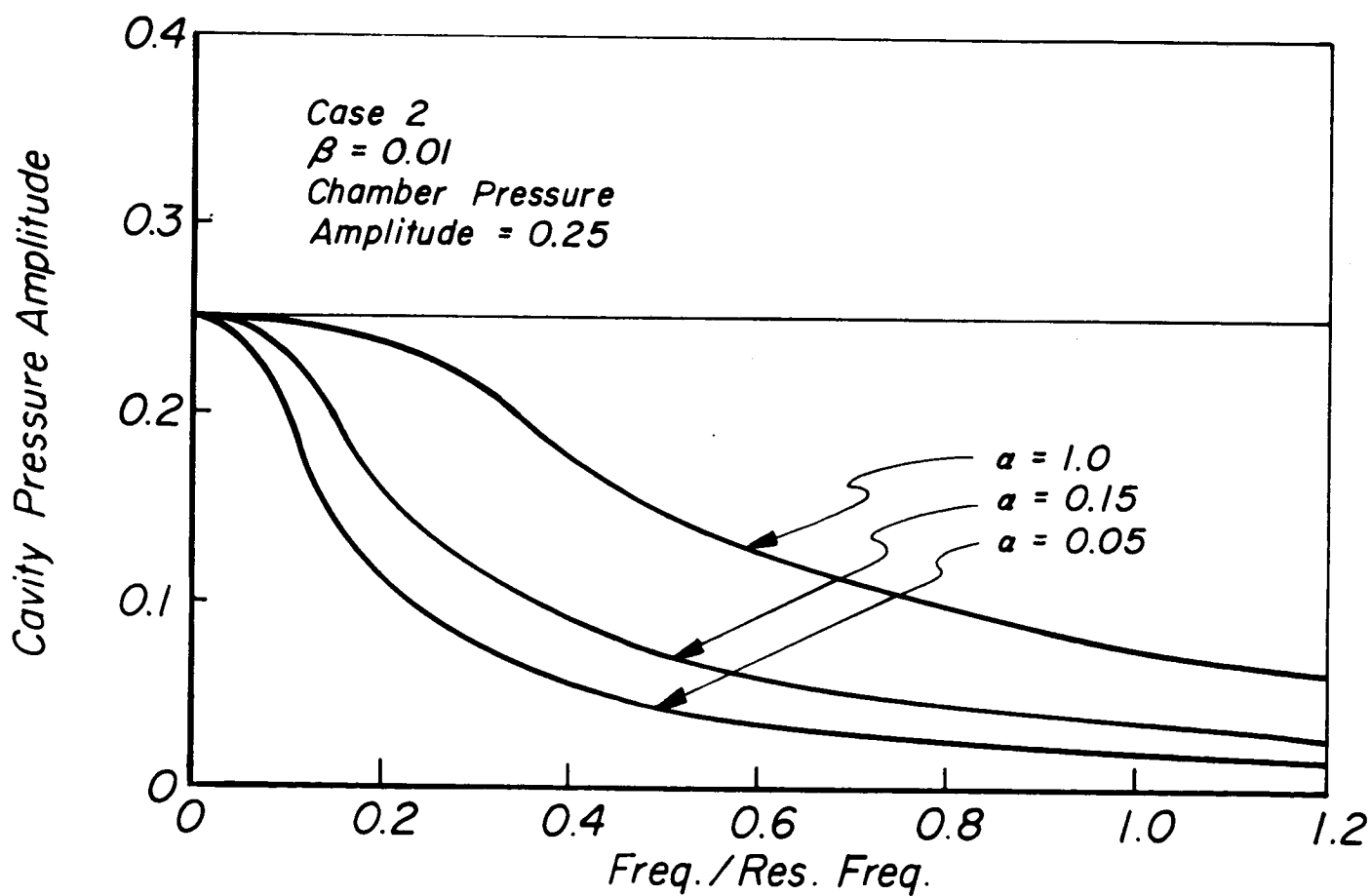
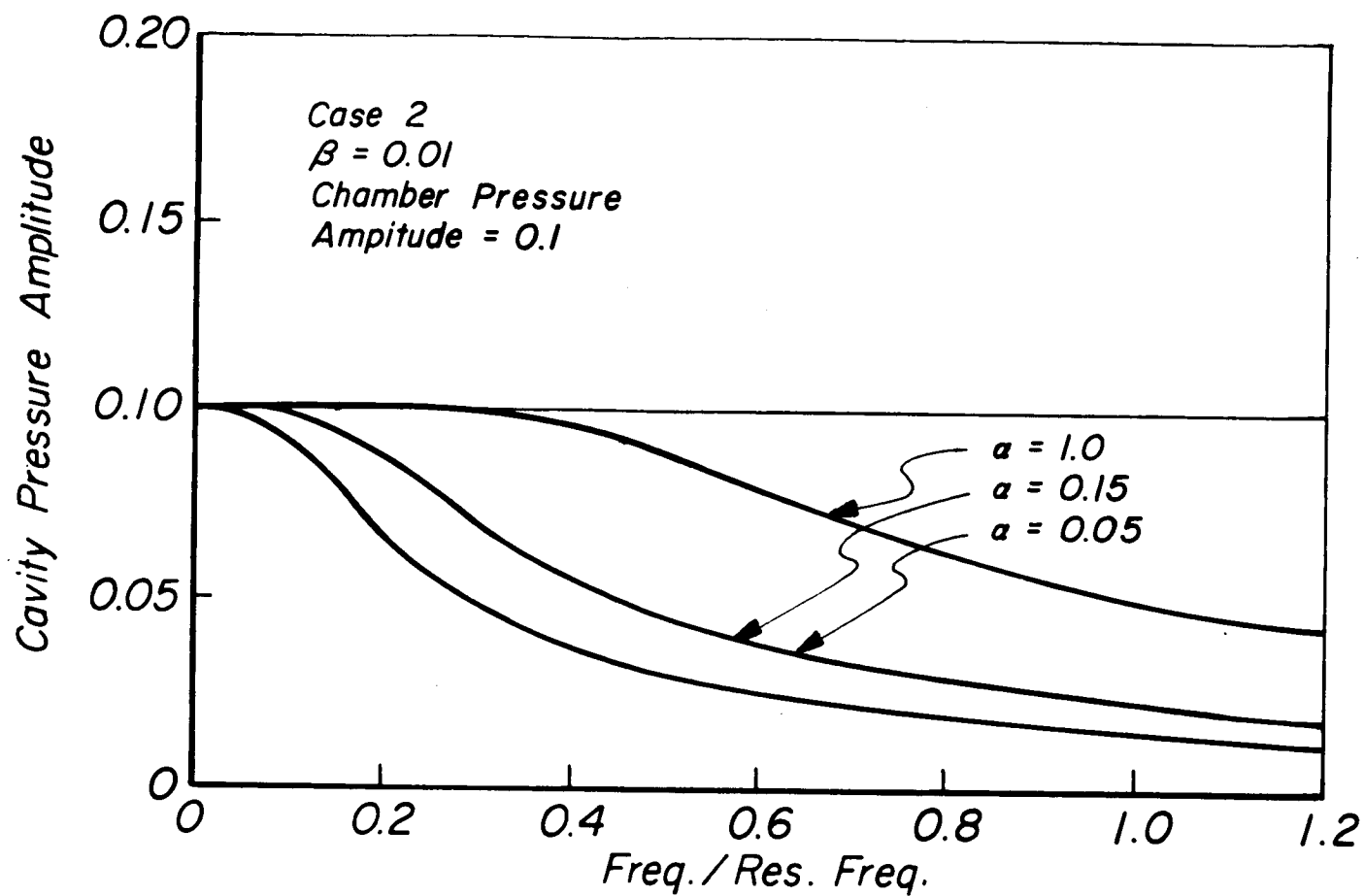


Figure 19

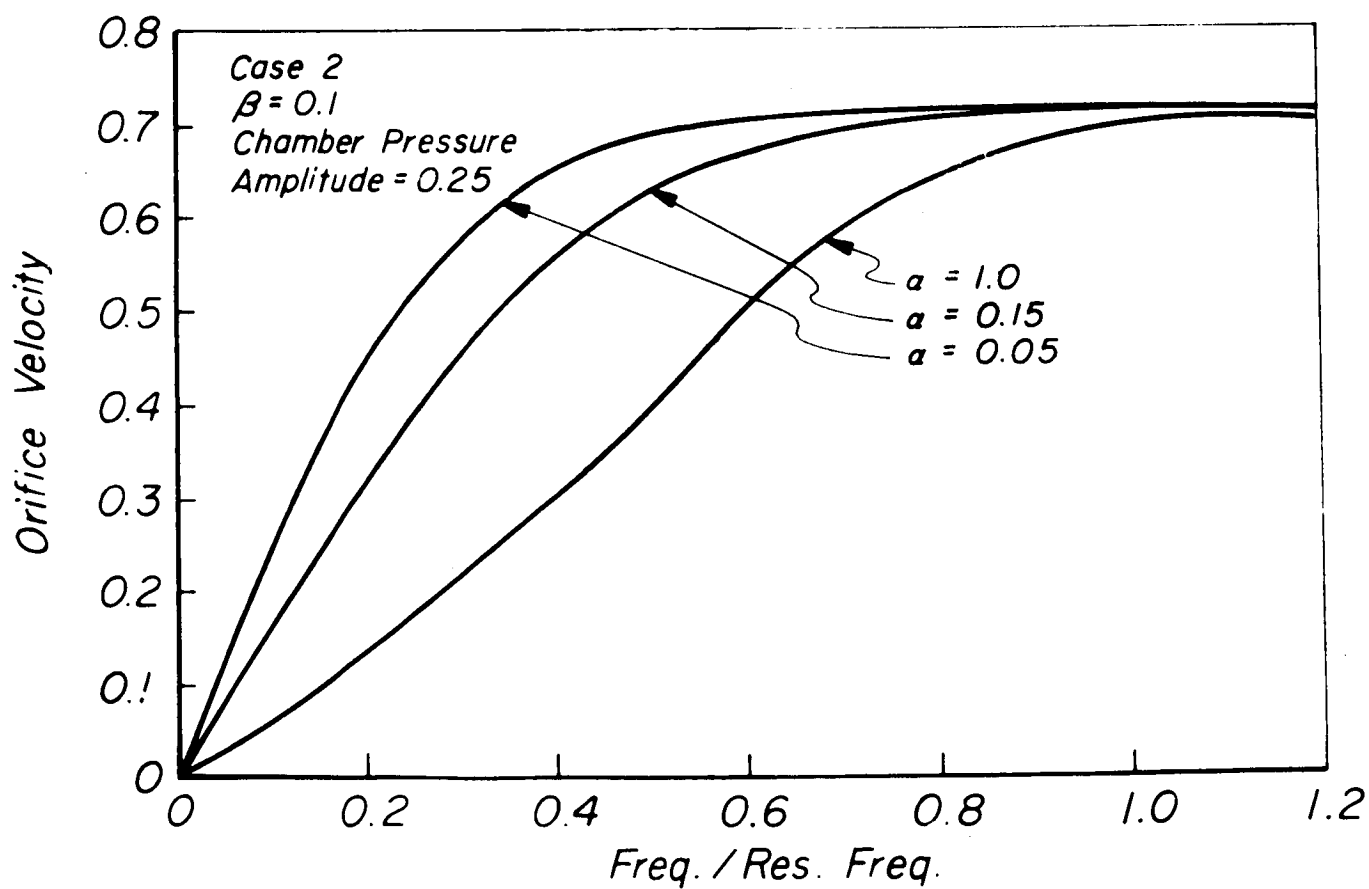
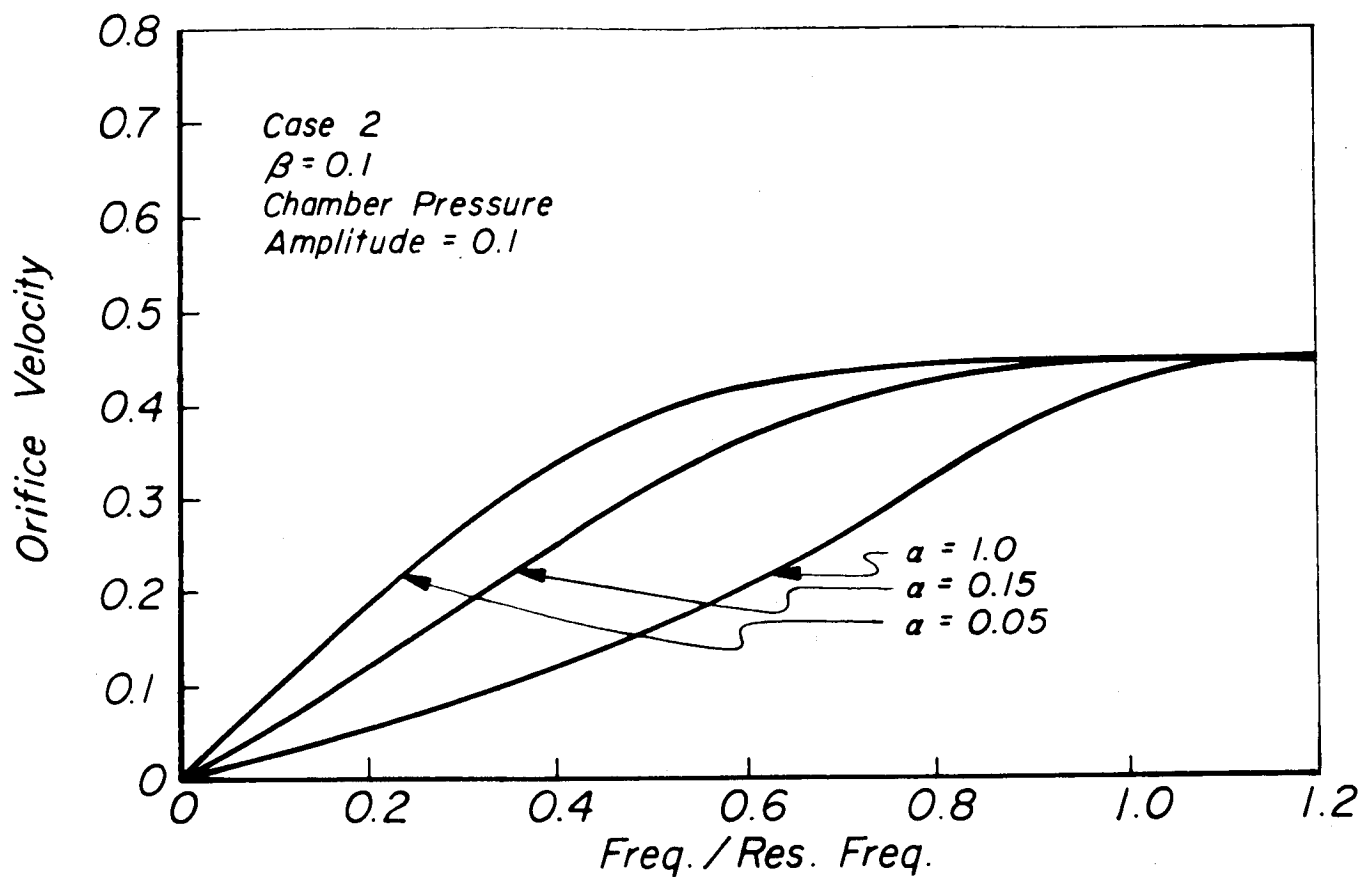


Figure 20

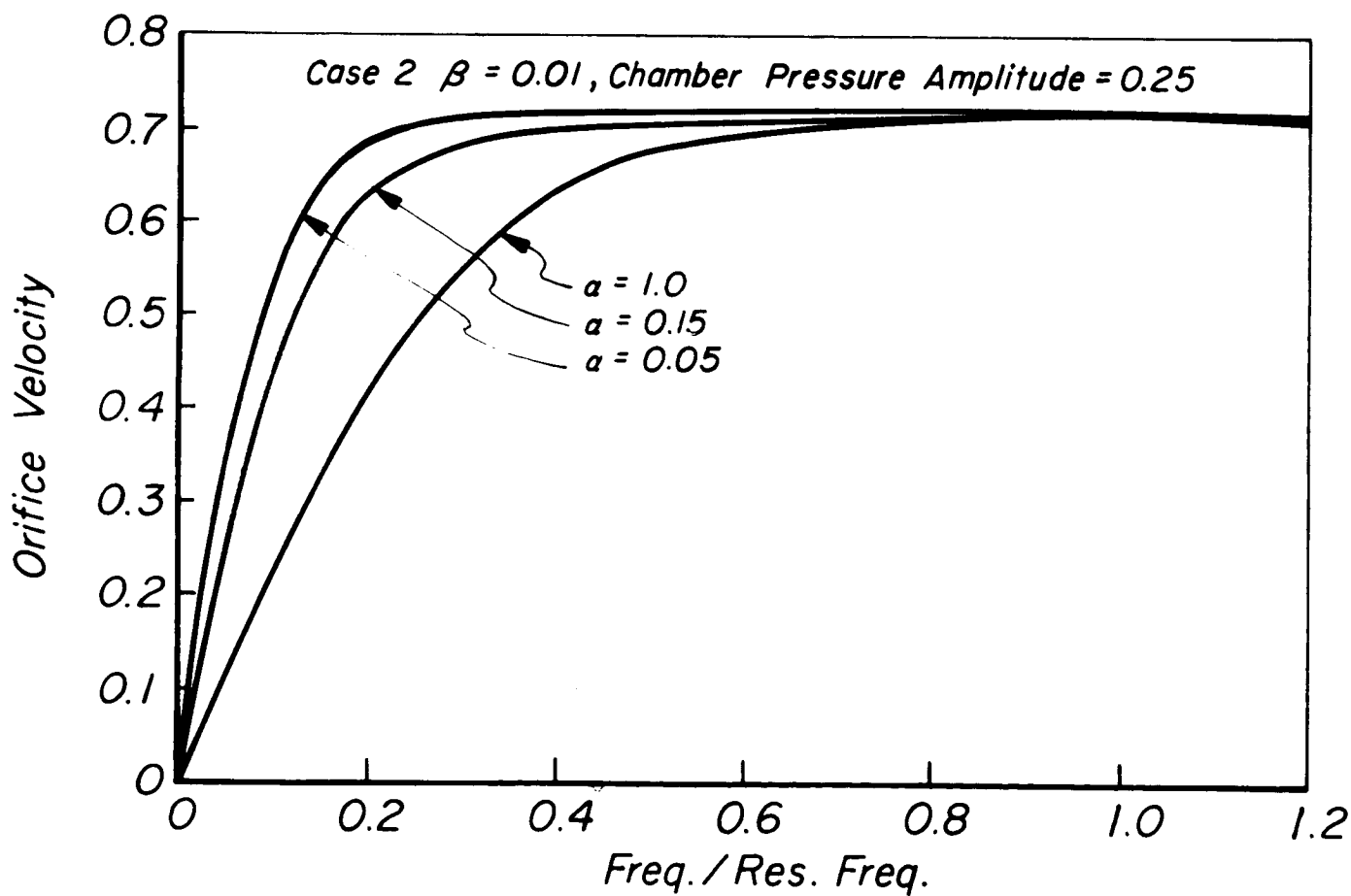
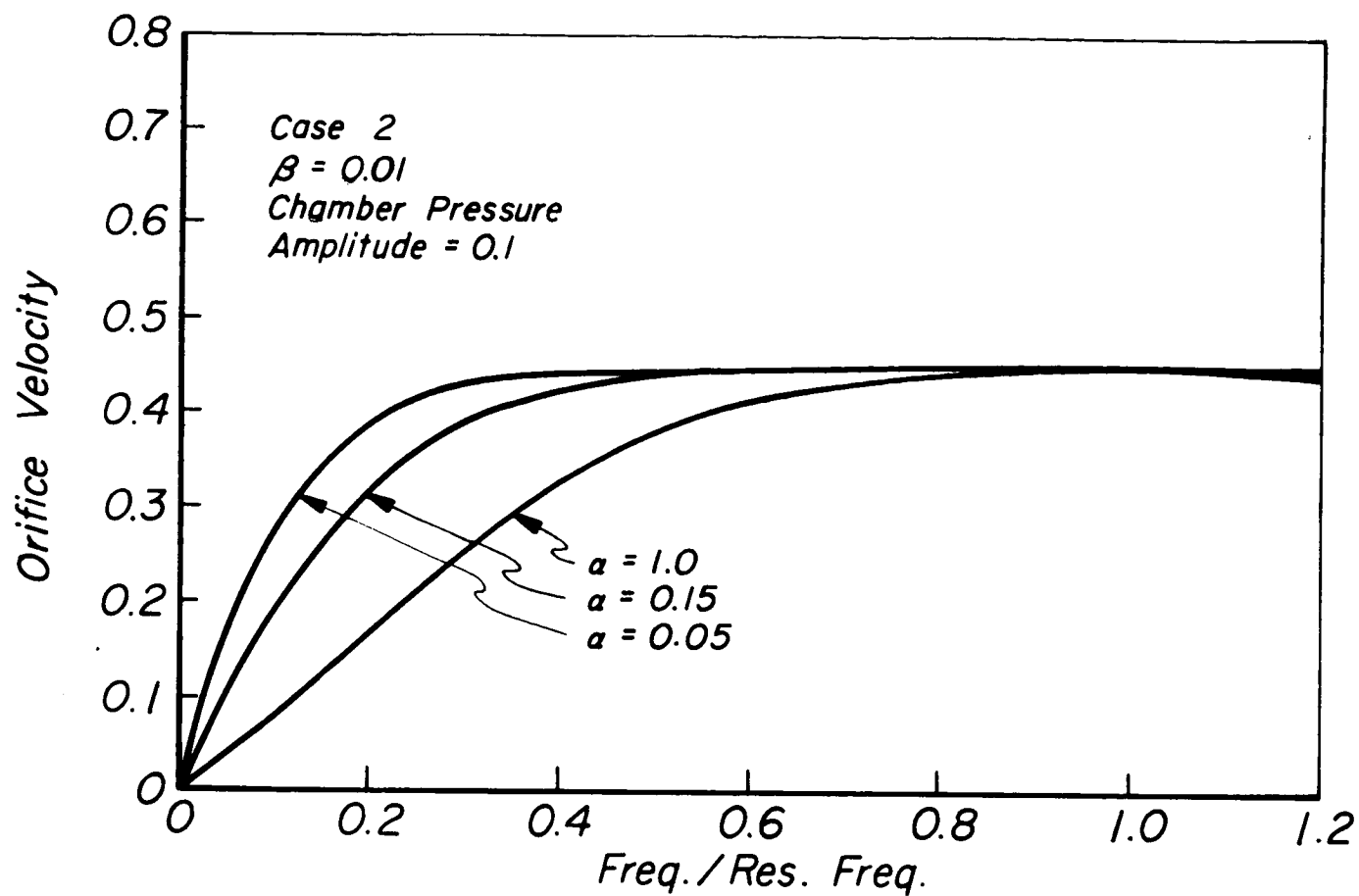
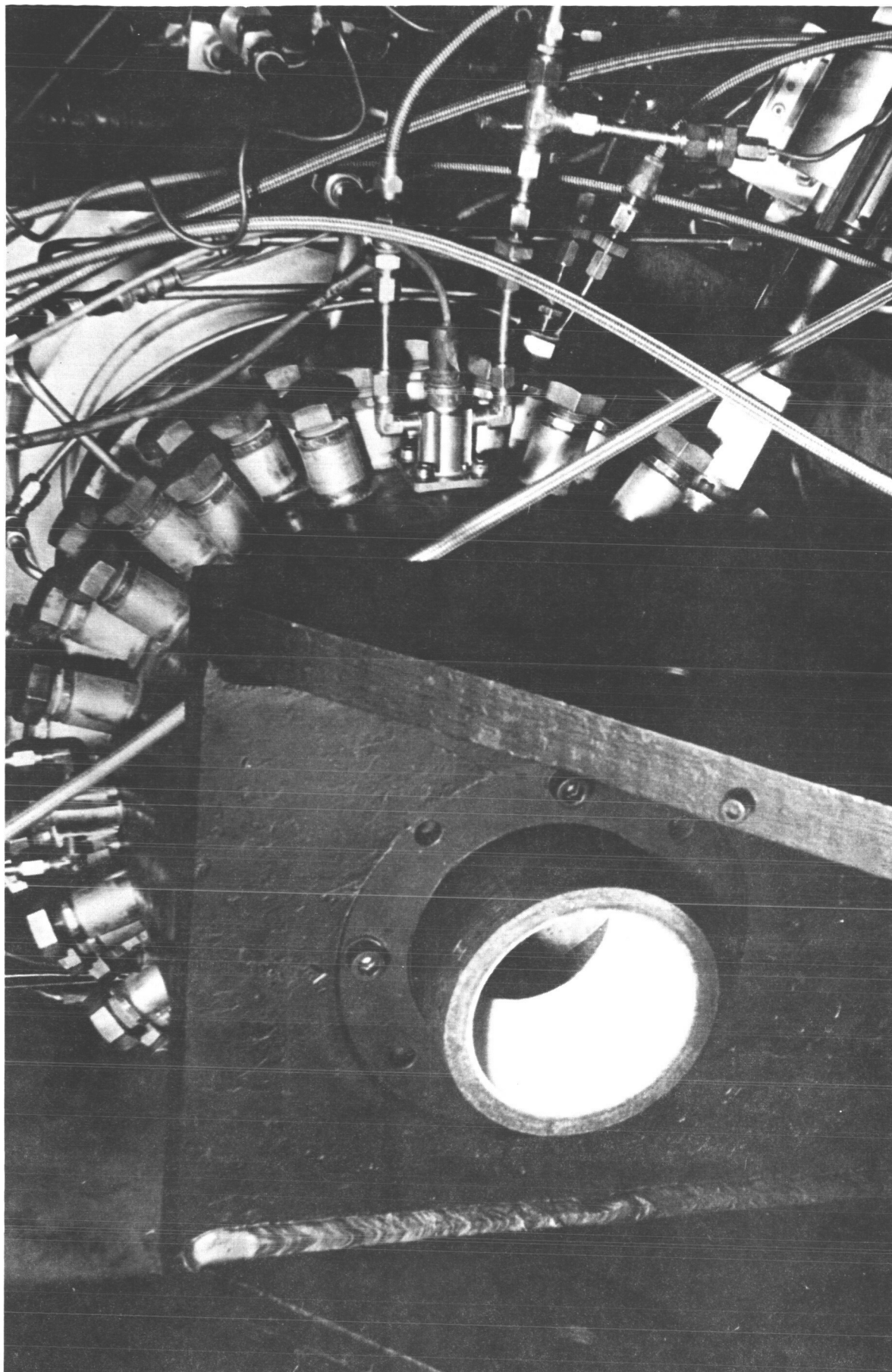


Figure 21



Acoustic cavity lined rocket chamber

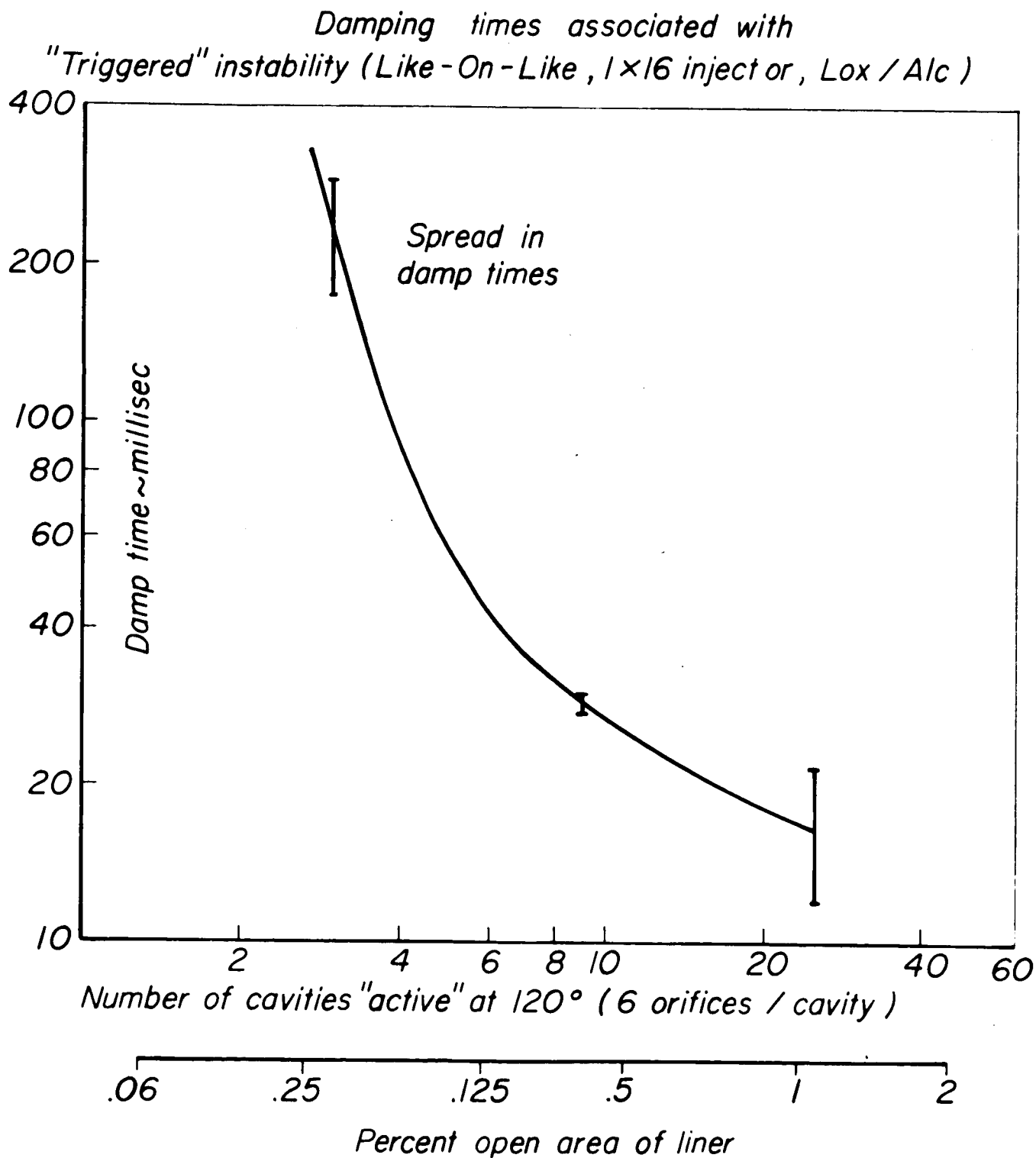
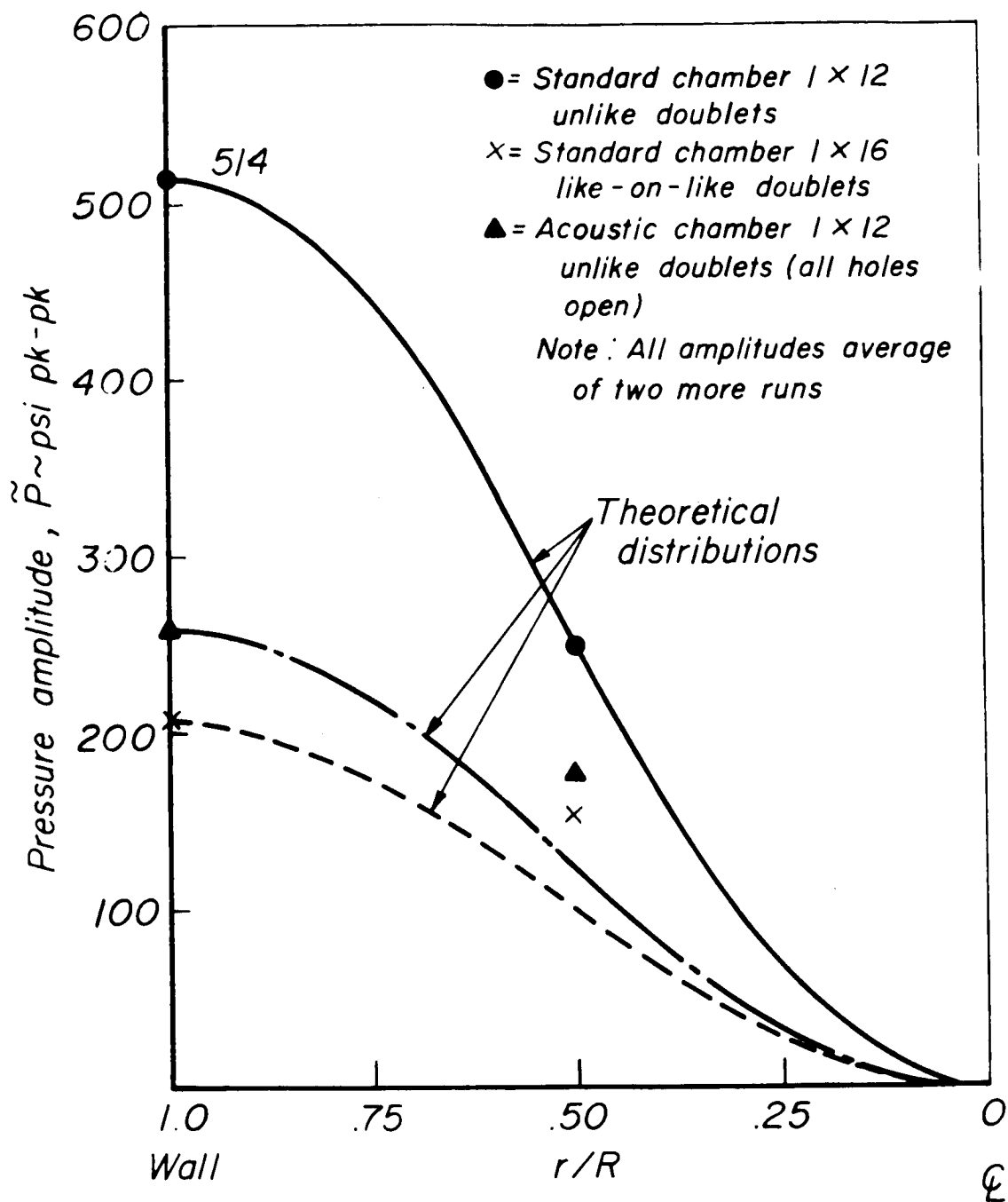
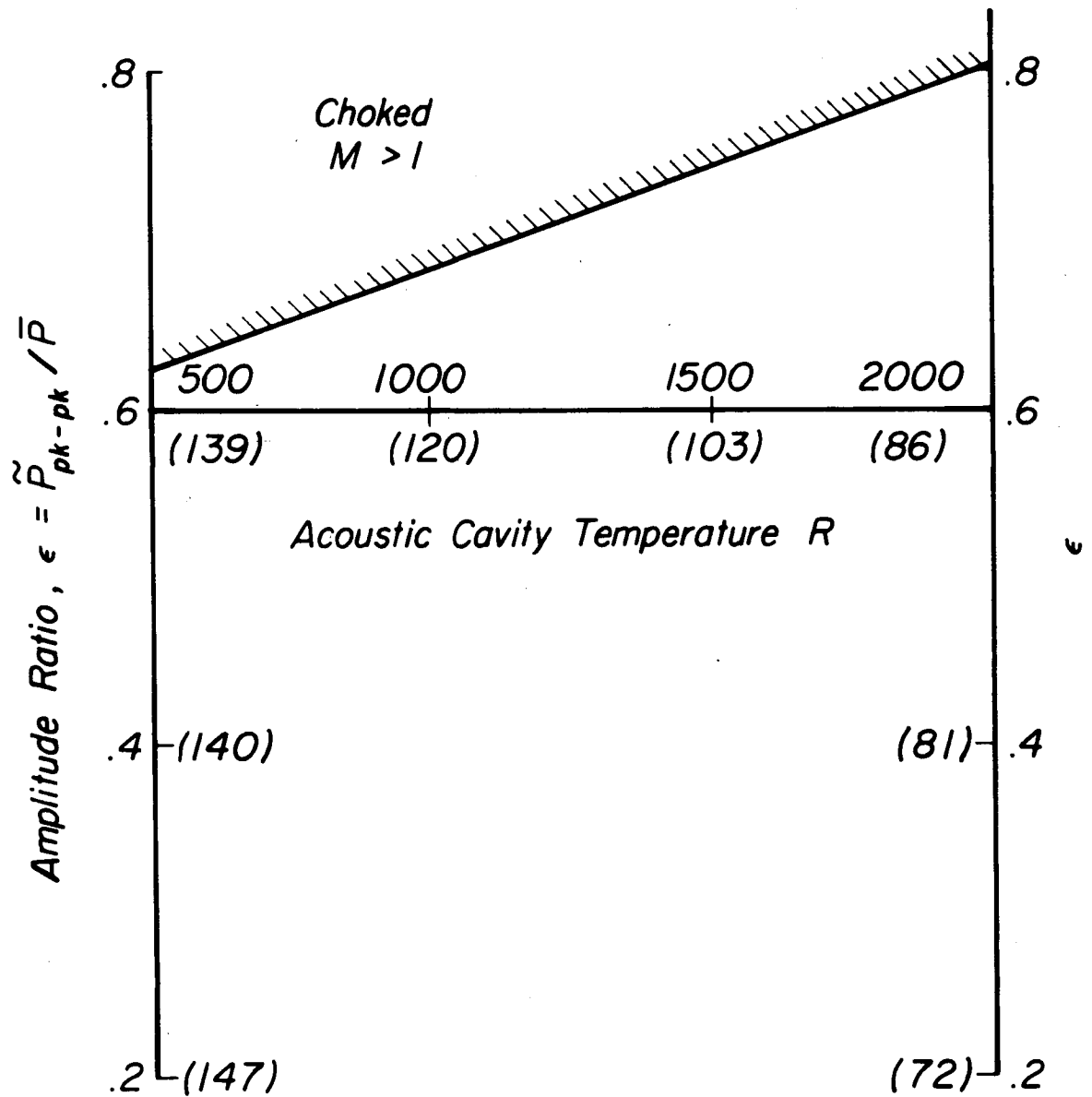


Figure 23



Radial pressure amplitude distributions
 first tangential mode

Figure 24



Phase Between Cavity
and Chamber ~ (Degrees Lag)

Figure 25

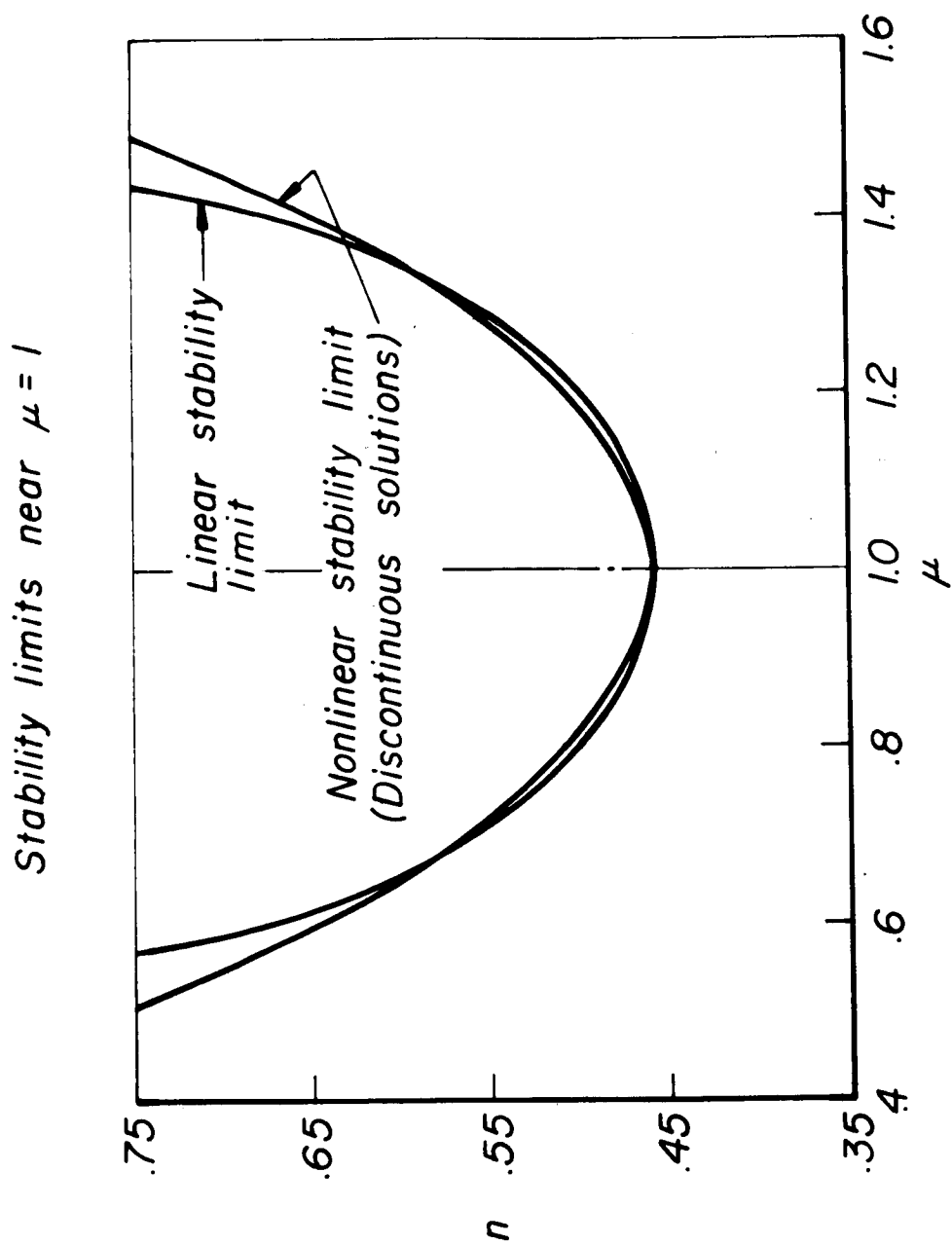


Figure 26

NP21-4234-67

Peak to peak and shock amplitude
as functions of normal displacement, $\mu^{(0)} = .28$

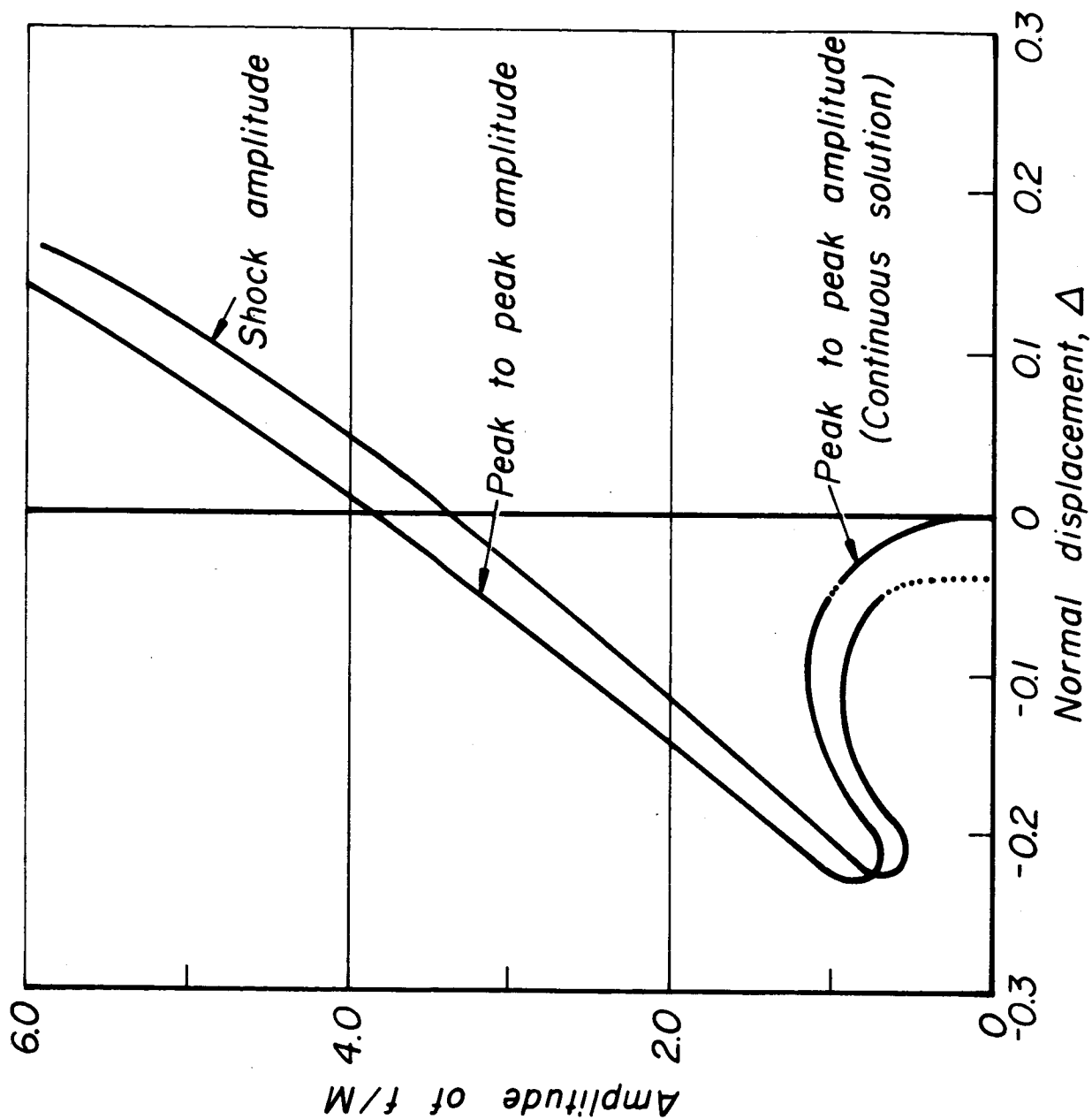


Figure 27

Peak to peak and shock amplitudes
as functions of normal displacement, $\mu^{(0)} = .80$

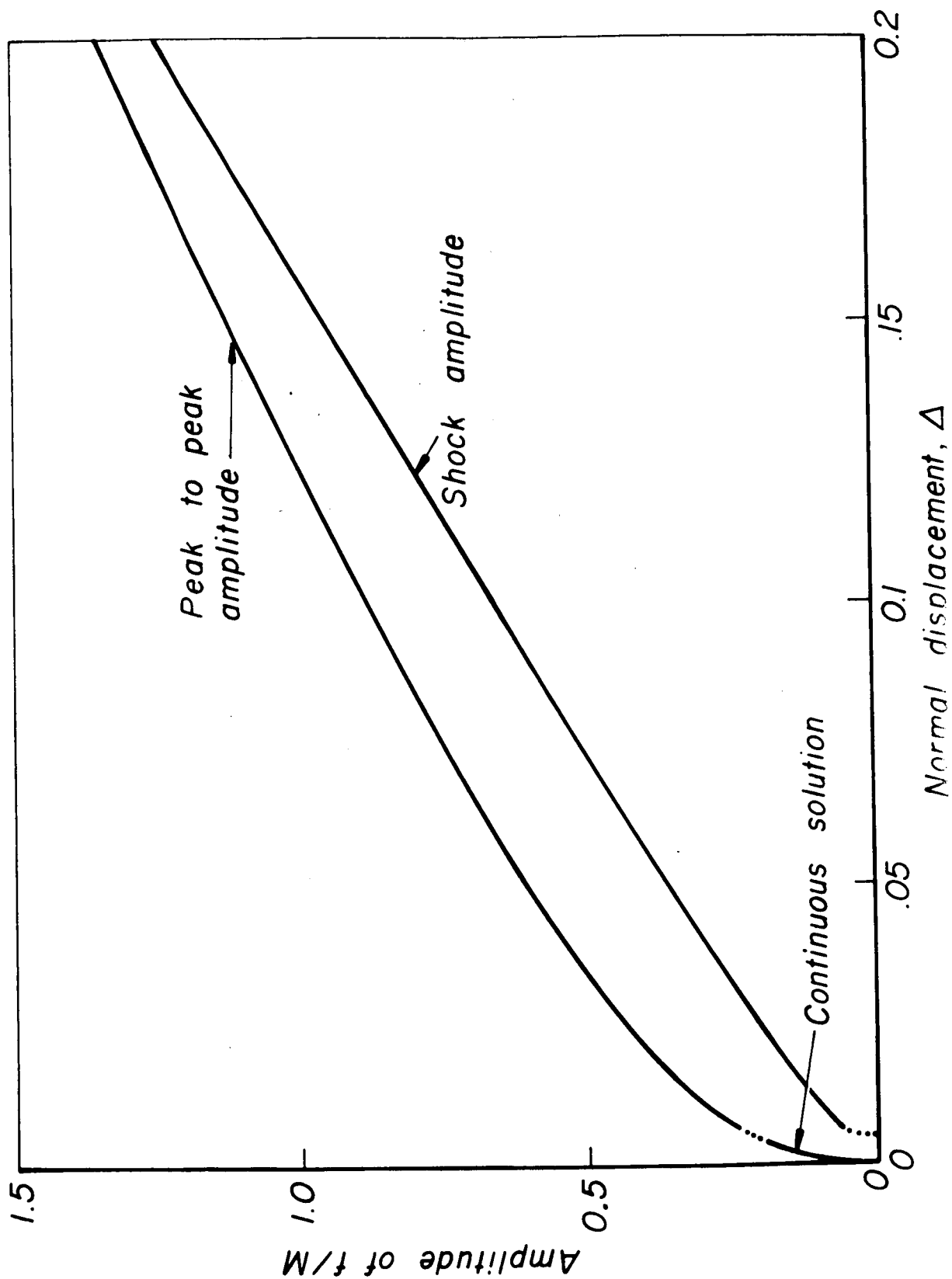


Figure 28

JP21-4232-67

First order period as a function of
normal displacement, $\mu^{(0)} = 28$

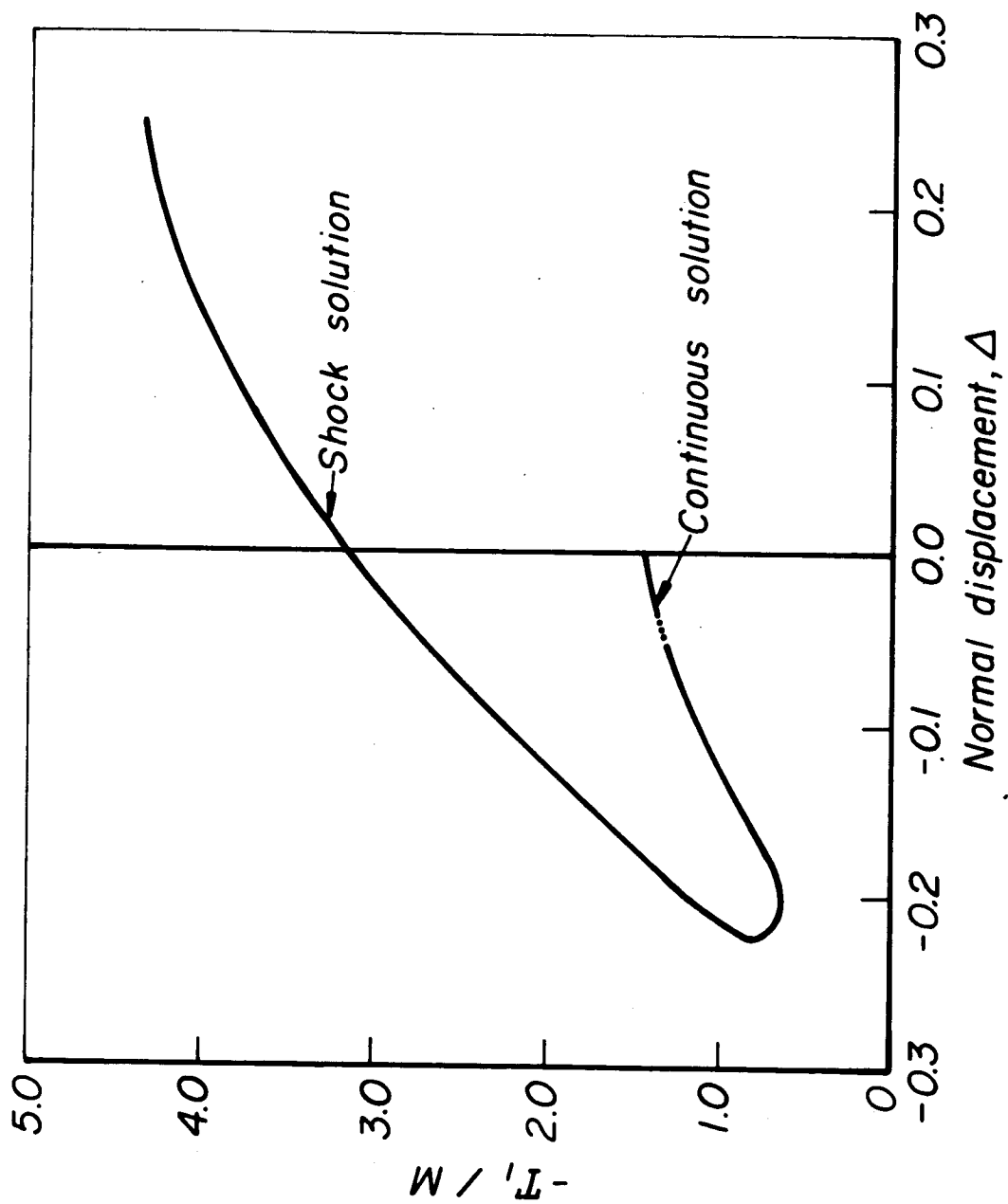


Figure 29

First order period as a function of
normal displacement, $\mu^{(0)} = .80$

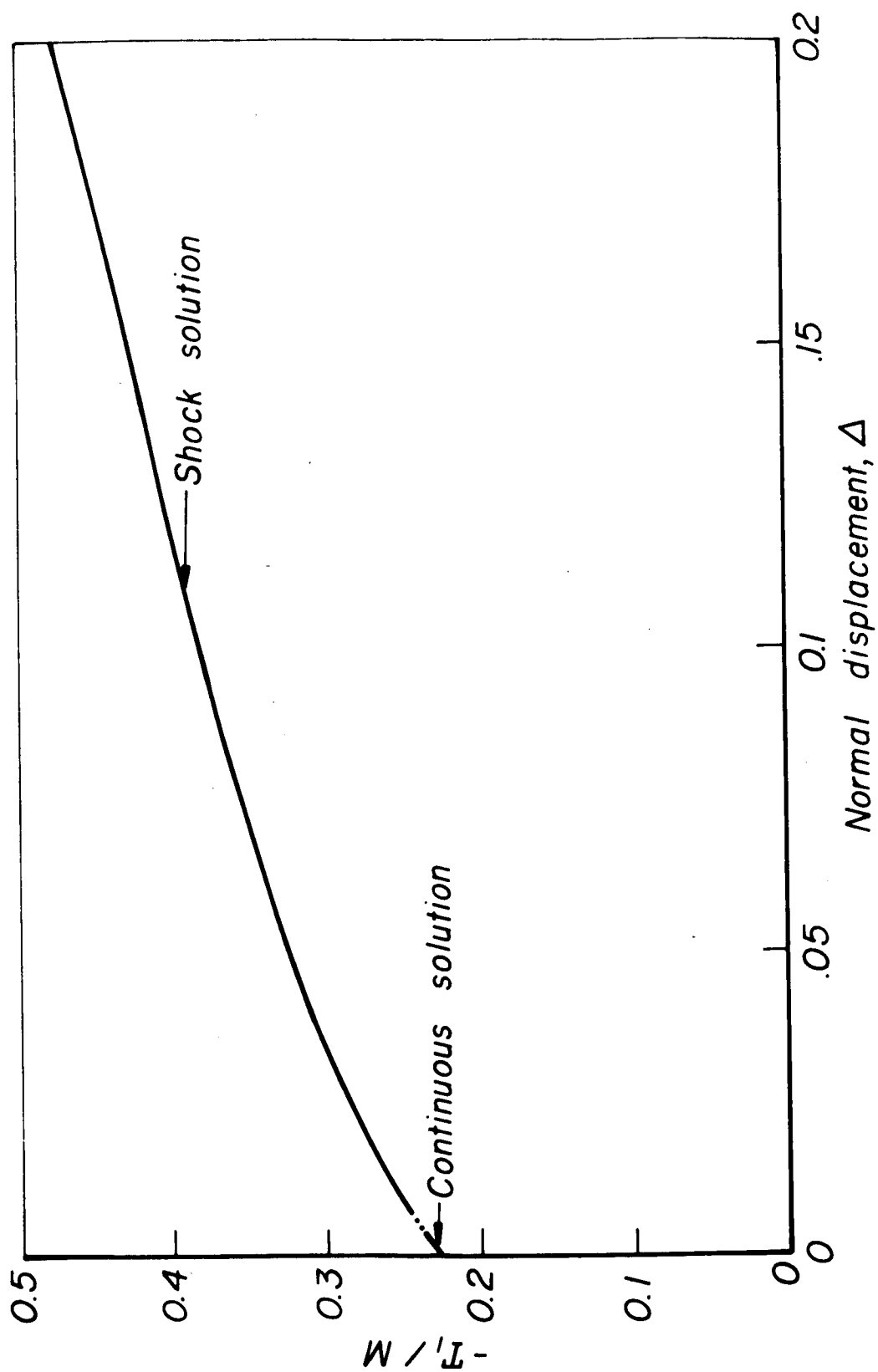


Figure 30

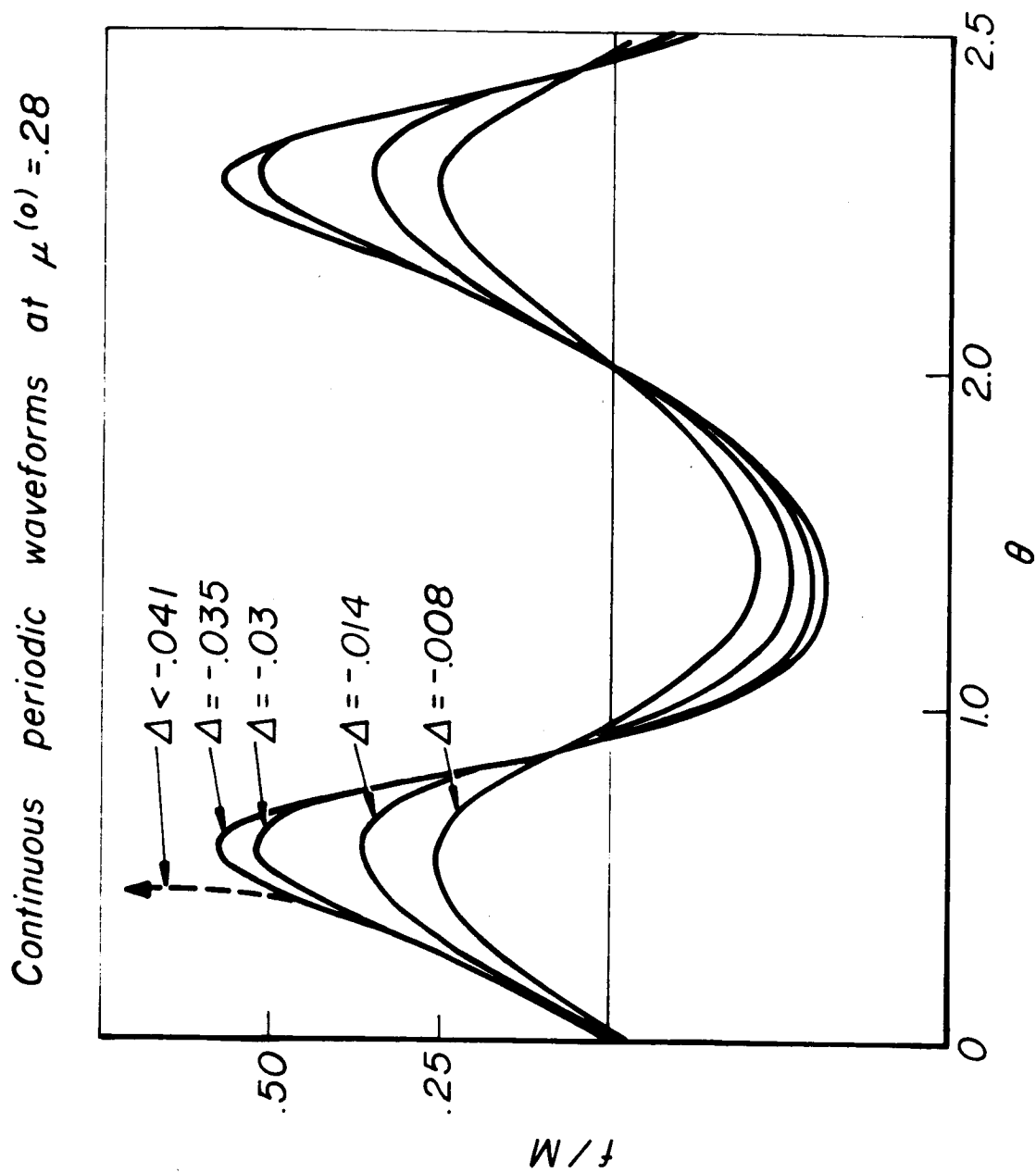


Figure 31

Pressure waveform for $\mu = 1.0$ $n = 2.5$
 Distributed combustion $d\bar{u}/dx = M_E$

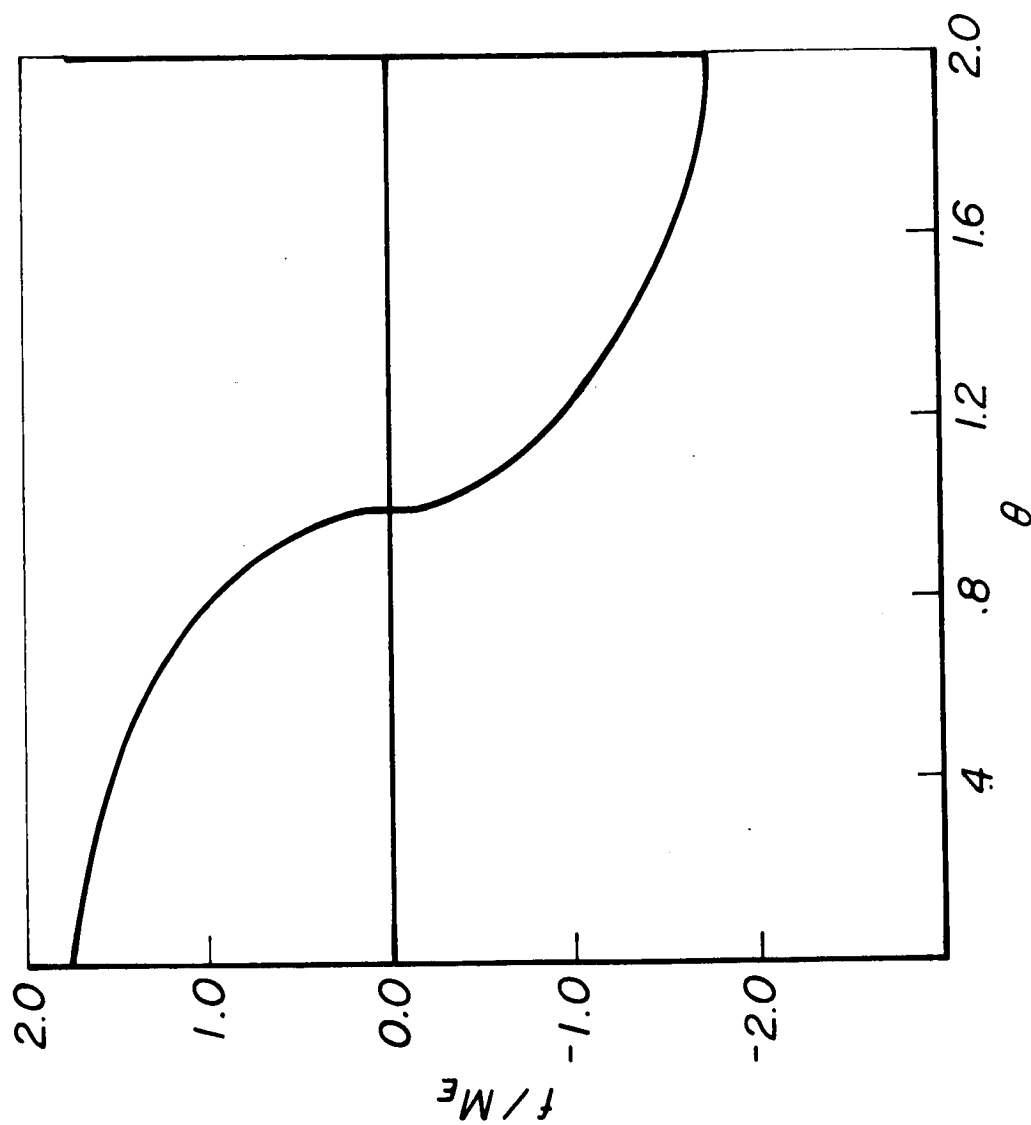


Figure 32

Pressure waveforms along the line $\mu = 1$

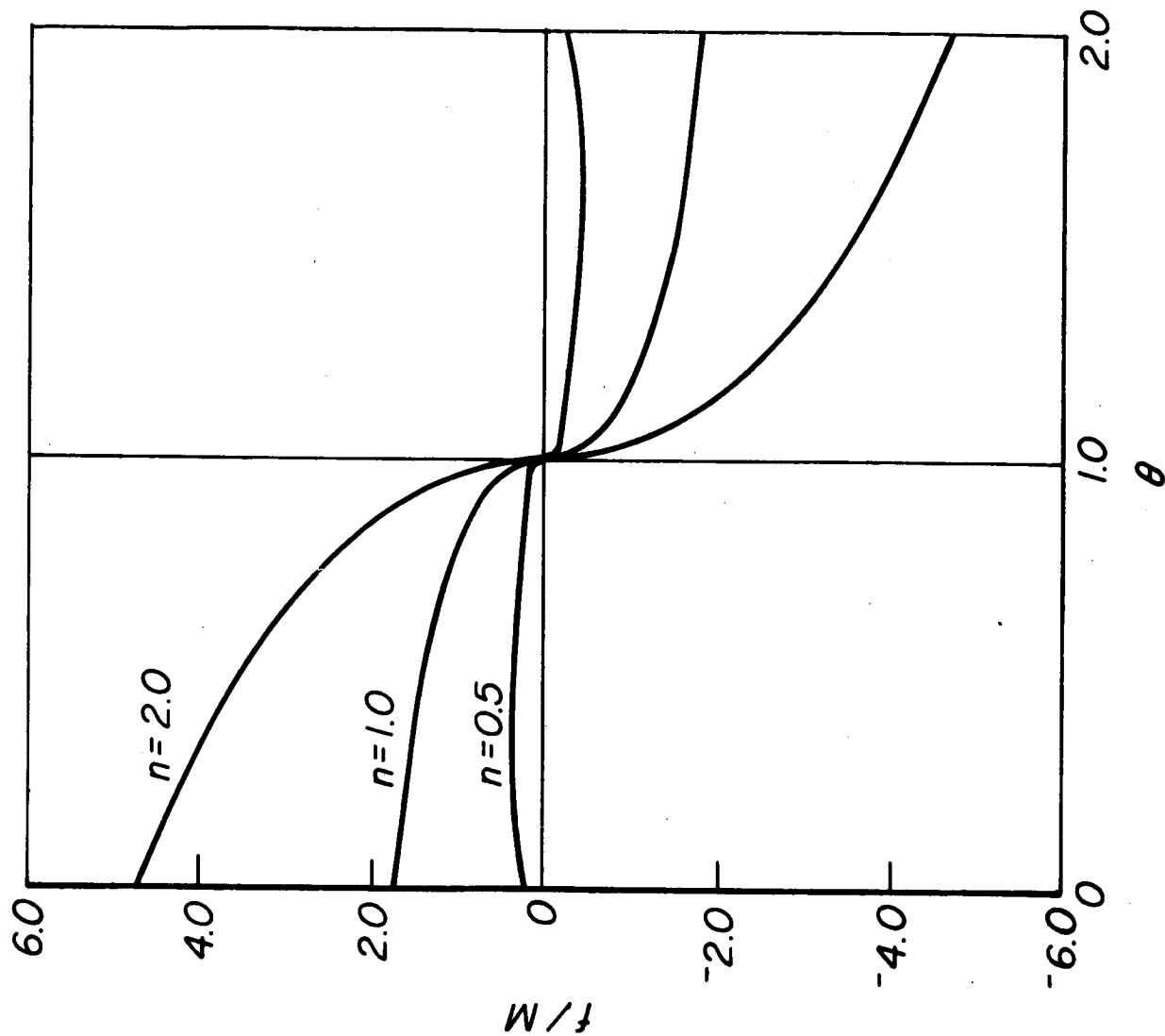


Figure 33

Steady - State Solution
Drop Temperature \bar{T}_d vs Axial Distance X

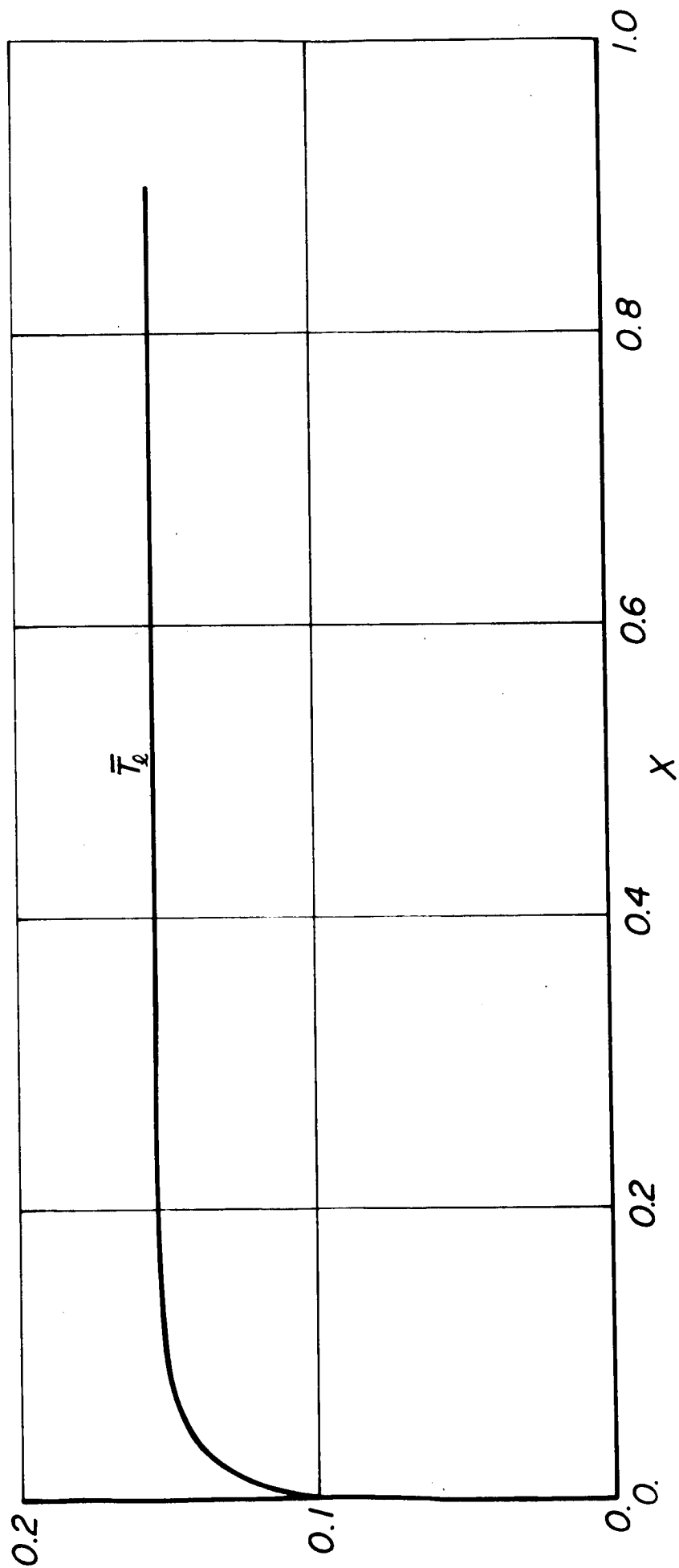


Figure 34

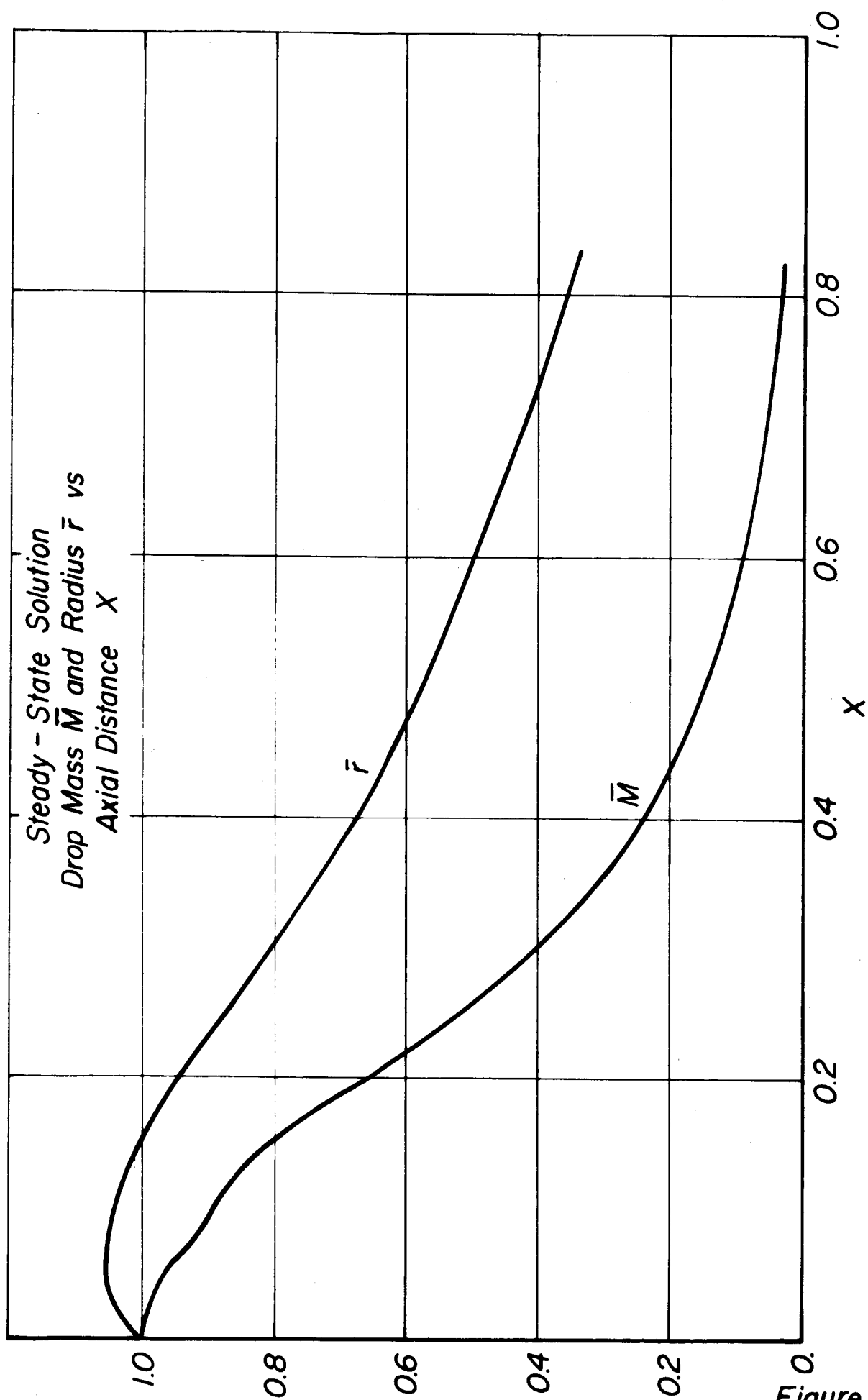


Figure 35

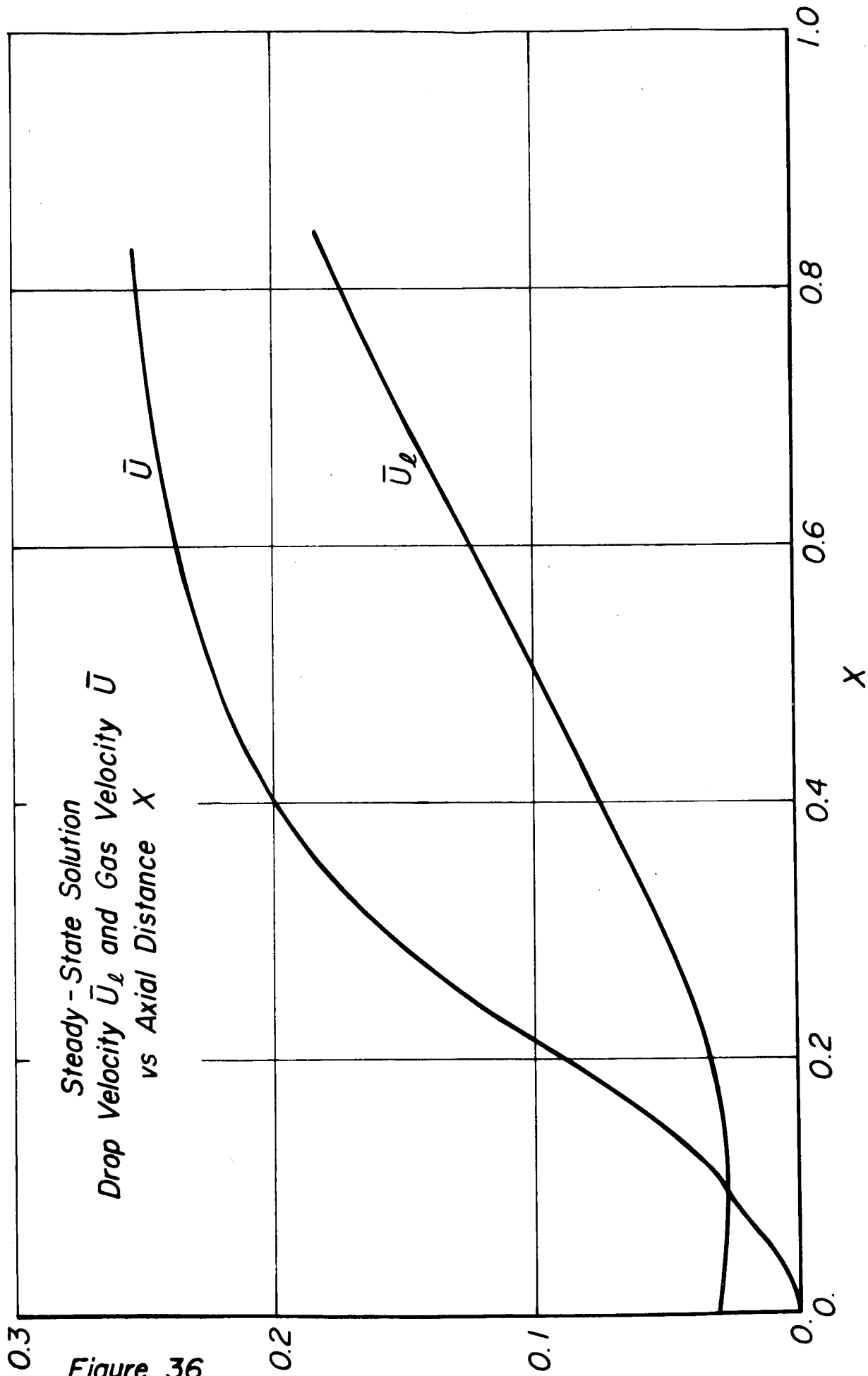


Figure 36

Steady - State Solution
Vaporization Rate per Drop \bar{W} vs
Axial Distance X

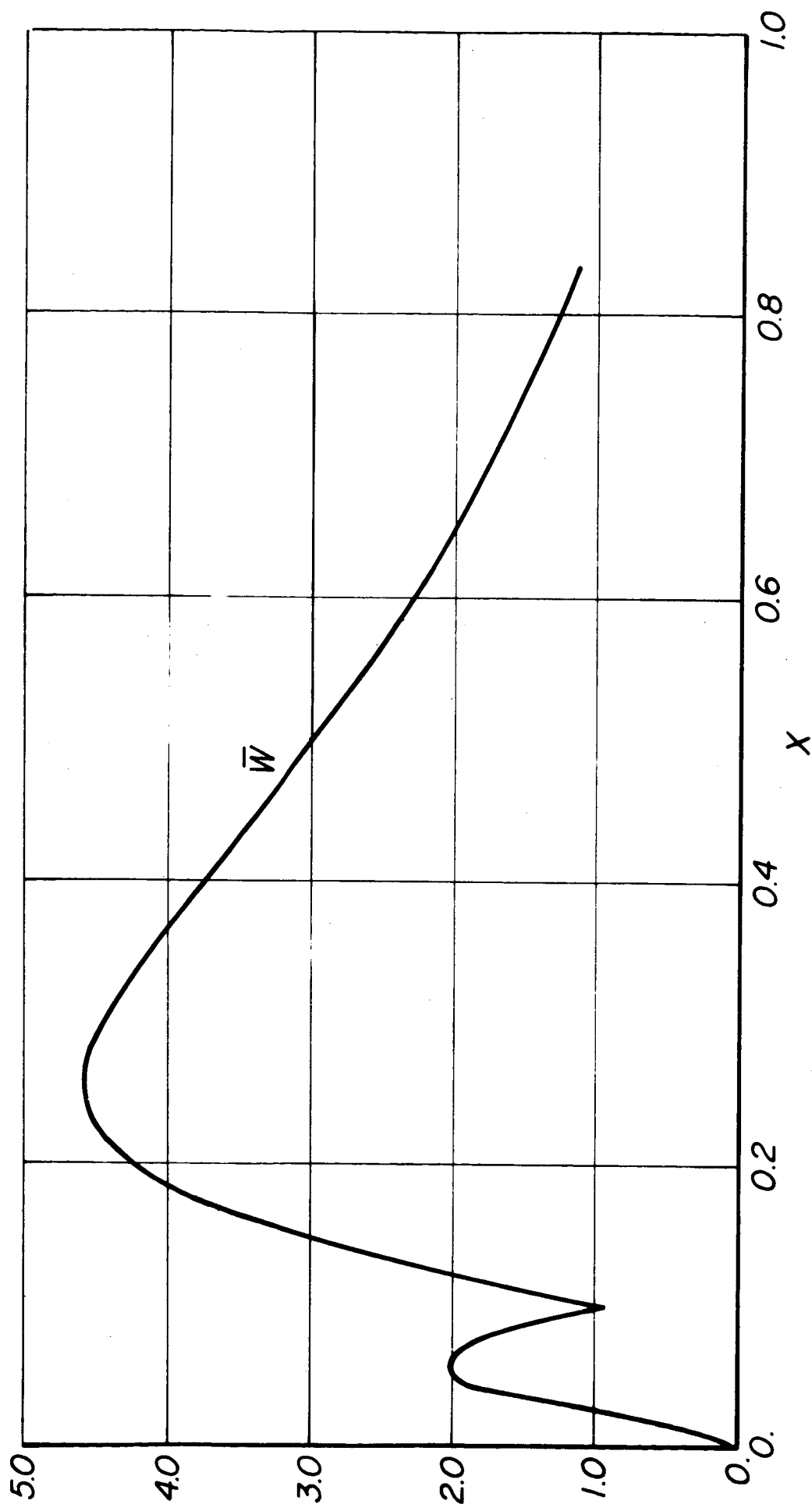


Figure 37

Steady - State Solution
Vaporization Rate per Unit Volume \bar{W}_T vs
Axial Distance X

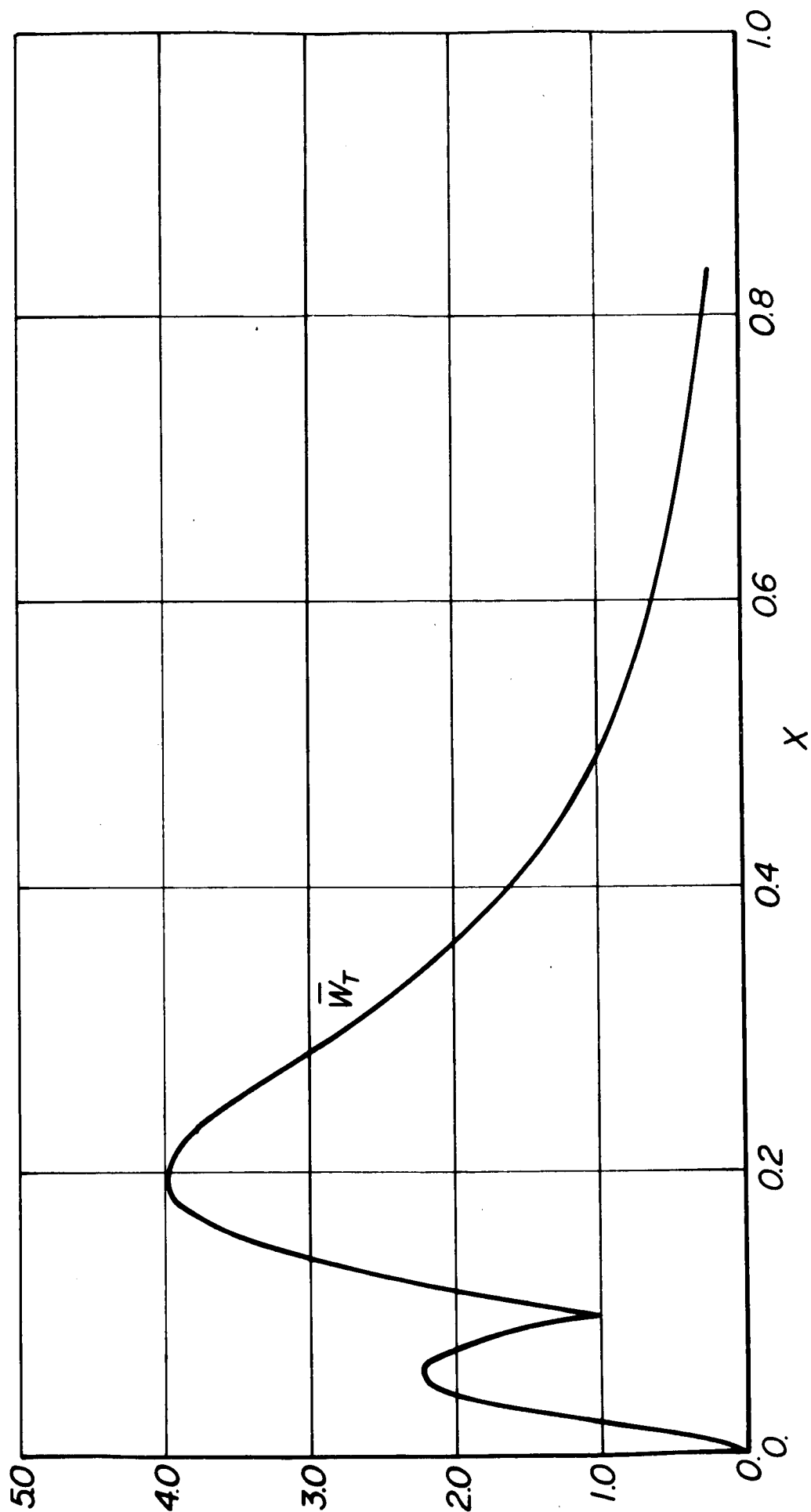


Figure 38

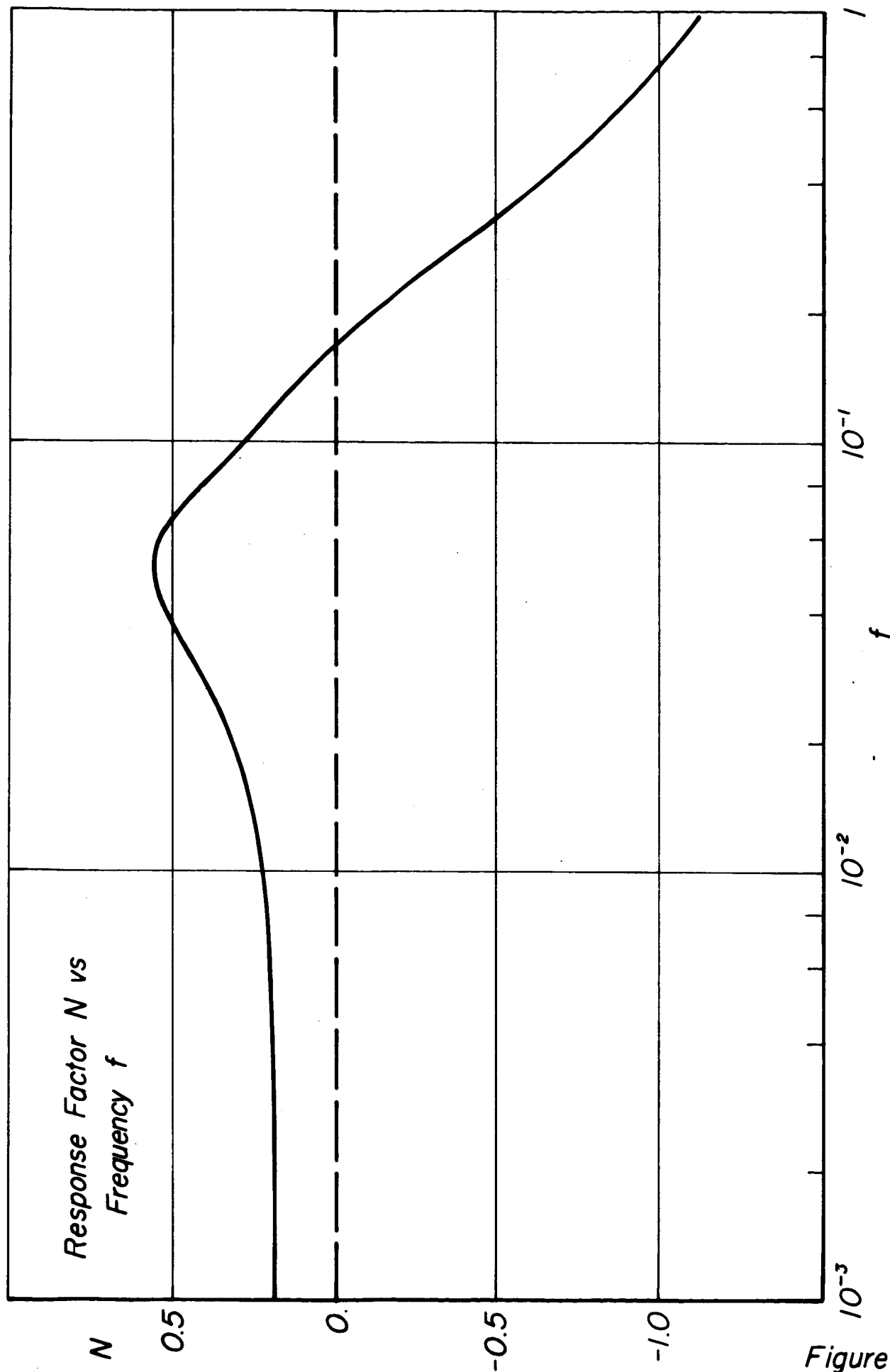


Figure 39

Response Factor N vs
Frequency f

$P_A^* = 20.0 \text{ atm}$
 $P_B^* = 30.0 \text{ atm}$

A
B

10^{-1}

f

10^{-2}

10^{-3}

0.5

0.

-0.5

-1.0

Figure 40 N

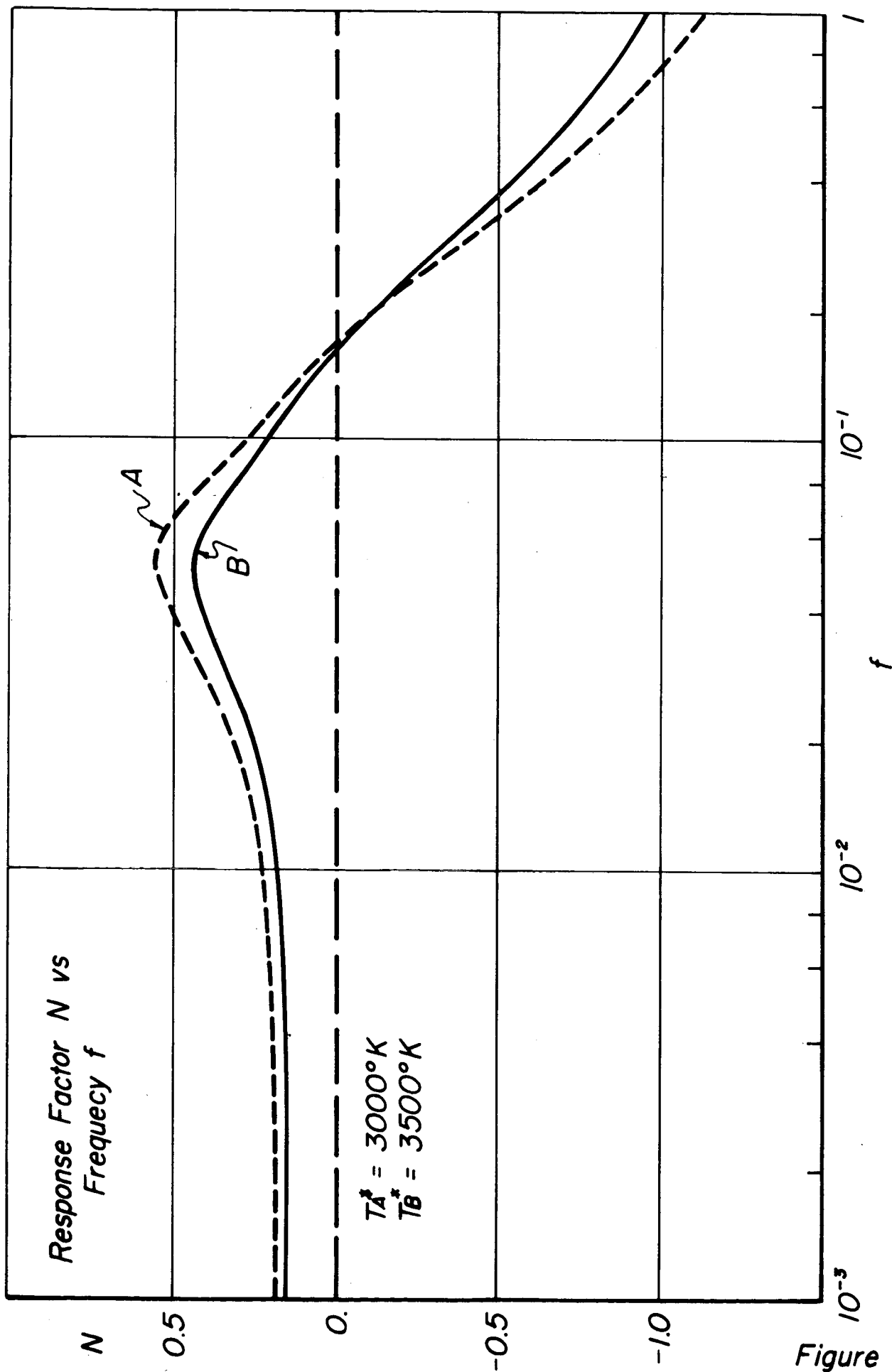
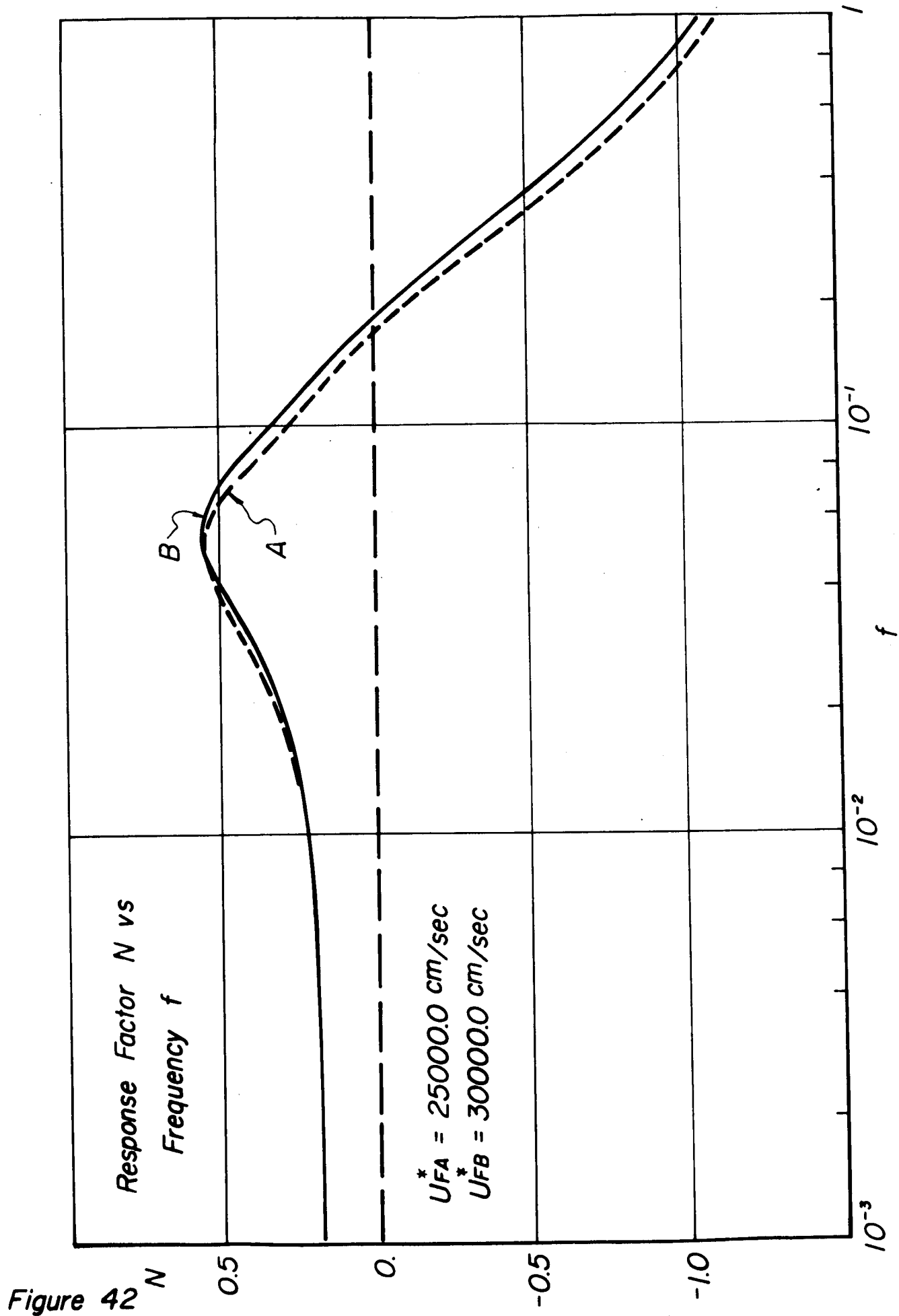


Figure 41



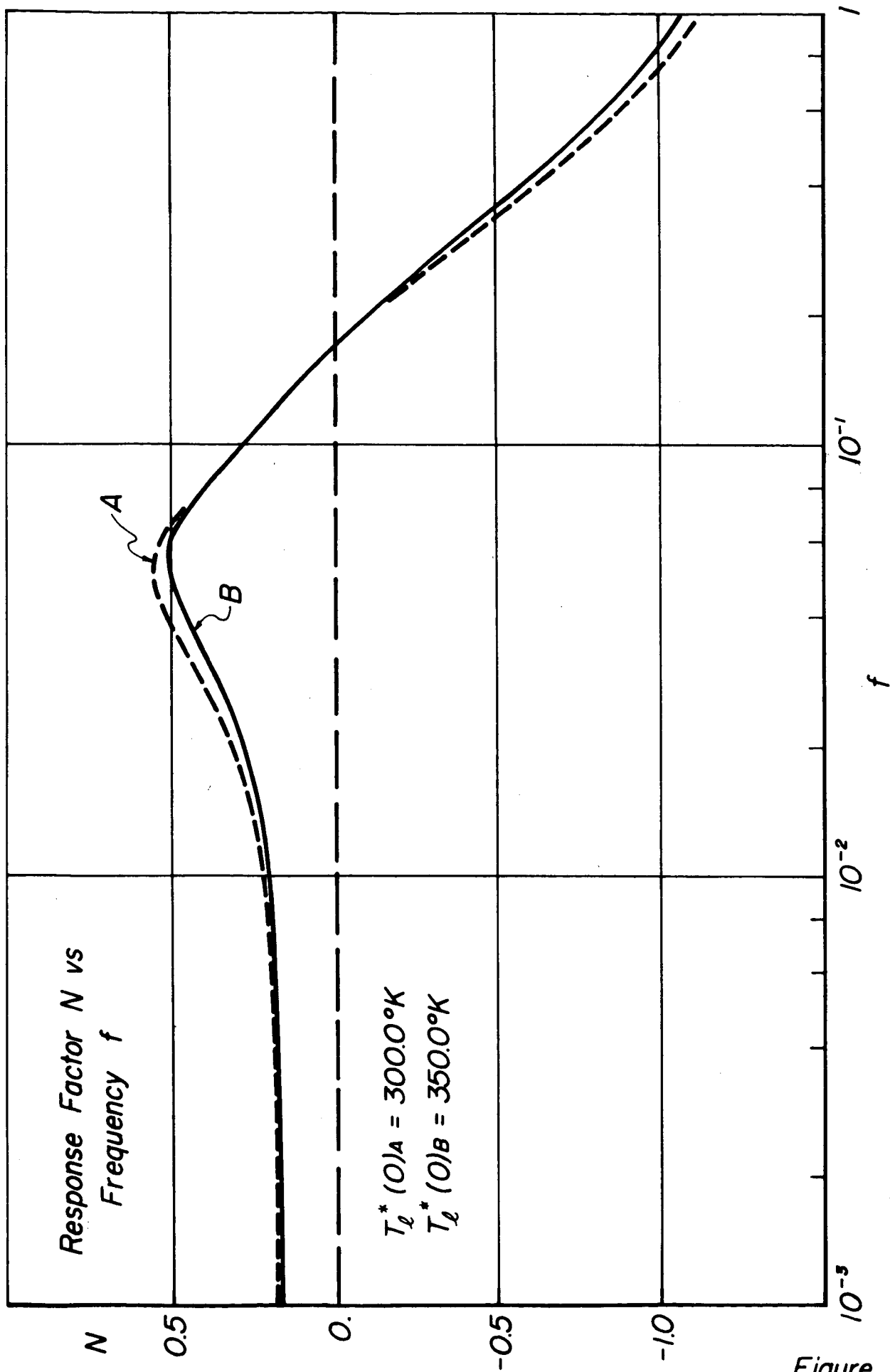


Figure 43

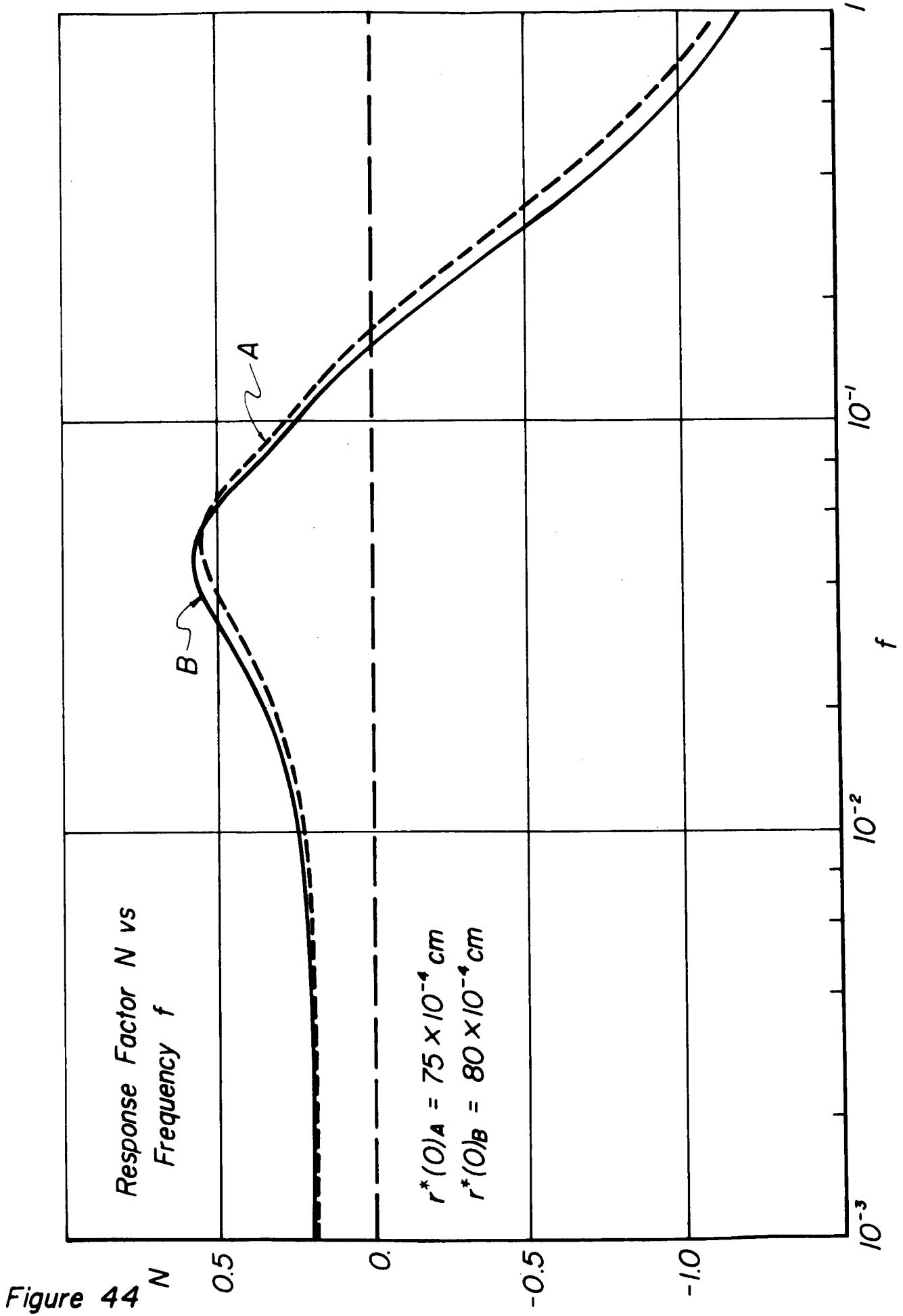


Figure 44

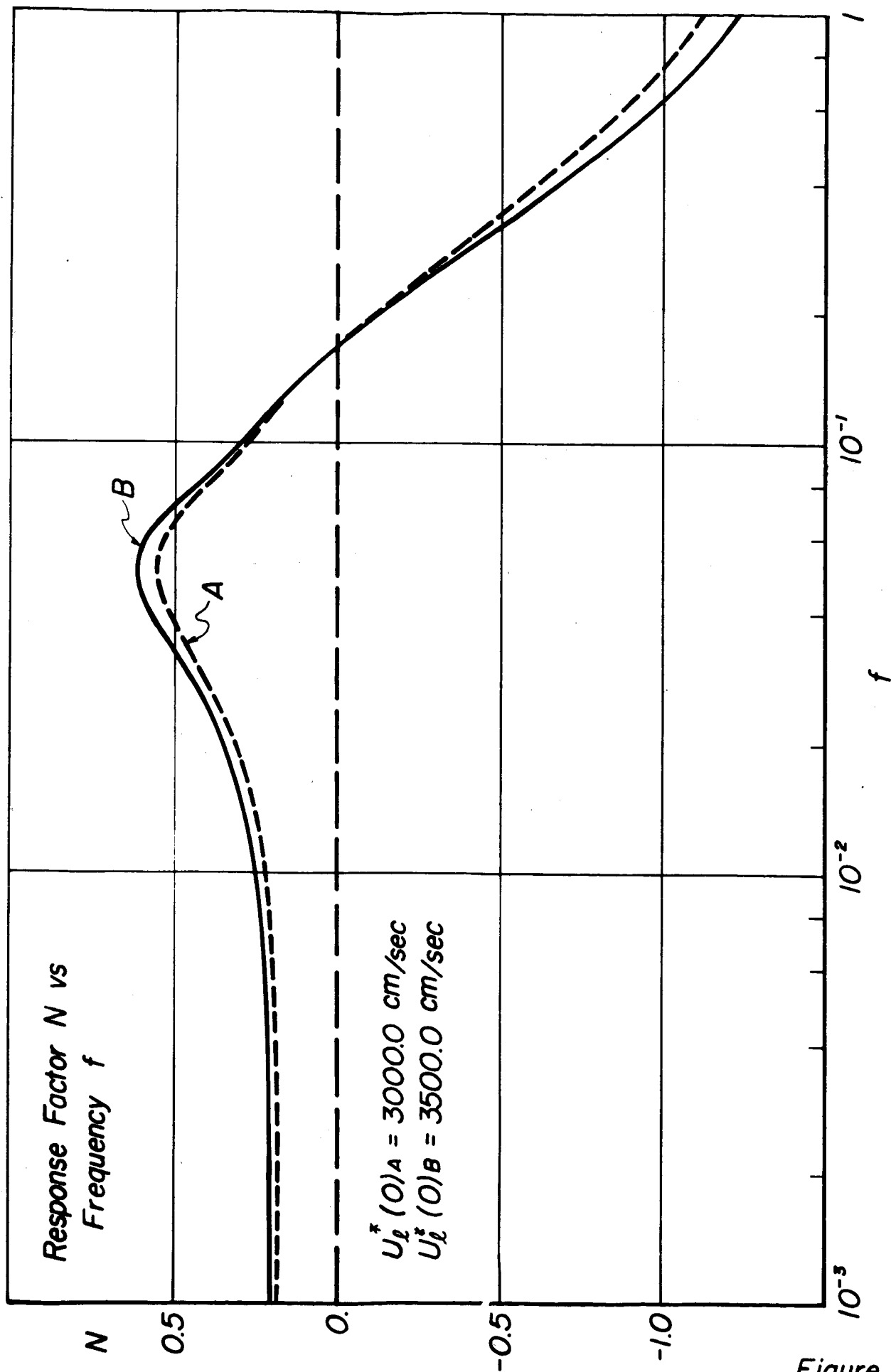


Figure 45

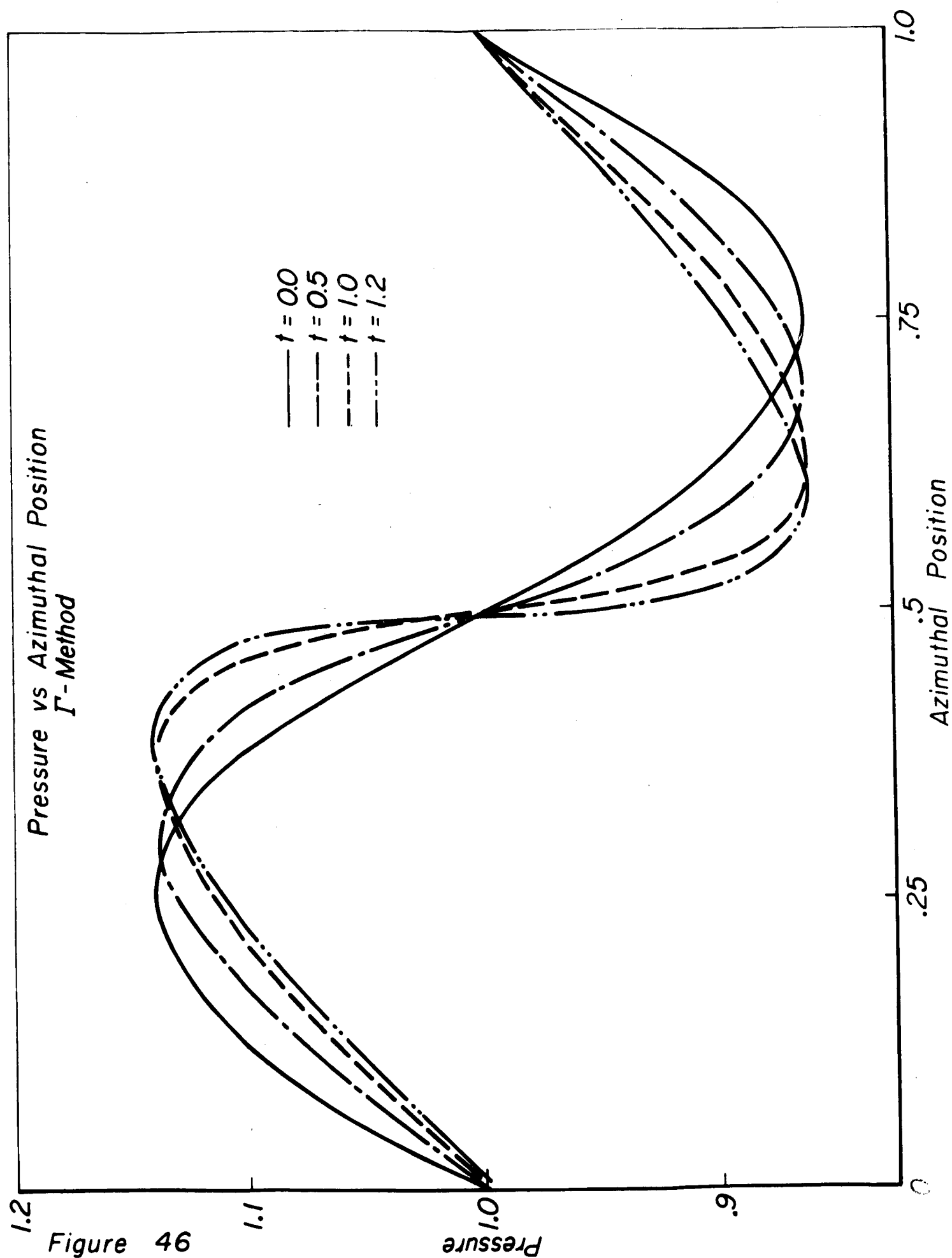


Figure 46

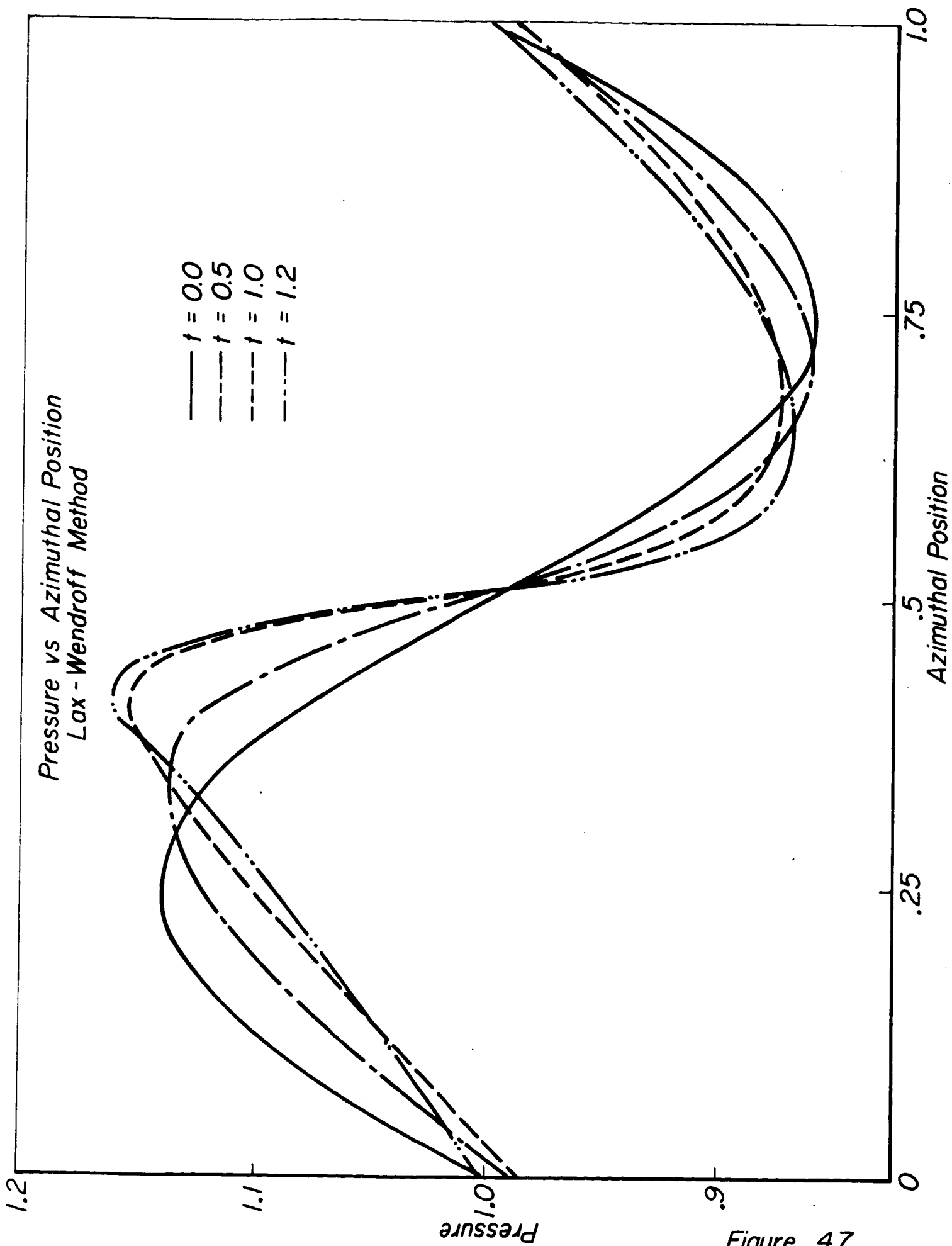


Figure 47

TABLE I

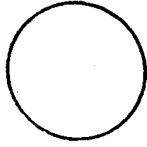
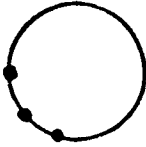
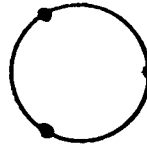

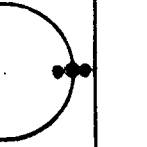
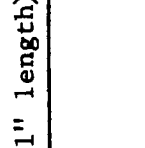
LINER STUDIES WITH LIKE-ON-LIKE INJECTION (LOX/ALC, 1 x 16 F) P _c = 150 psia					
ACTIVE CAVITIES (.375" cavity length, 2800 Hz)	PRESSURE OSCILLATIONS (psi pk-pk) Initial Final		FREQUENCY (Hz)	DAMP TIME (millisec)	
none 	226-236	200-250	2900-3000	∞	
3 grouped (within 72° @ .75" from injector face) 	222-240	130-150	2900-2970	∞	
3 @ 120° (.75 inch from face) 	235-242	74-76/c.n.	2720	170-285	
3 @ 120° (2 inches from face) 	-	78-97	2785-2855	∞	
9 @ 120° (3 @ .75, 2.00 & 3.25") 	222-226	c.n.	2650 (during damp)	28-30	
26 @ 120° (plus 27 @ 120° with .141" length) 	193-216	c.n.	2670	12-22 millisec	

TABLE II

LINER STUDIES WITH UNLIKE INJECTION (LOX/ALC 1 x 12 DOUBLETS) $P_c = 150$ psia					
ACTIVE CAVITIES (.375" cavity length)	PRESSURE OSCILLATIONS (psi pk-pk)		FREQUENCY (Hz)	DAMP TIME (millisec)	
	Initial	Final			
None	Spontaneous	340	3150-3185	∞	
9 @ 120° (3 @ .75, 2.00 & 3.25")	"	275	3090	∞	
17 @ 120° (6 @ .75, 5 @ 2.00 & 6 @ 3.25")	"	300	3000	∞	
26 @ 120° (9 @ .75, 8 @ 2.00 & 9 @ 3.25")	"	288 - 132 - 54 (115 AP)		∞	
26 @ 120° (plus 27 @ 120° with .141" length)	"	133	2940	∞	
52 open (@ .75, @ 2 & @ 3.25")	"	50 — 150	4670-4700	∞	
53 open (@ .75 @ 2 & @ 3.25")	"	216-258	3000	∞	

DISTRIBUTION FOR THIS REPORT

NASA

NASA Headquarters
Washington, D.C. 20546
Attn: Alfred Gessow
Robert S. Levine RPL (3)
A. O. Tischler RP

NASA
Universal North Building
Connecticut & Florida Avenues
Washington, D.C.
Attn: T.L. Smull, Director
Grants & Space Contracts (10)

NASA Scientific & Technical
Information Facility
P.O. Box 33
College Park, Maryland 20740 (15)

NASA Headquarters
Washington, D.C. 20546
Attn: E.L. Gray, Director
Advanced Manned Missions, MT
Office of Manned Space Flight

Attn: V.L. Johnson, Director
Launch Vehicles & Propulsion, SV
Office of Space Science

Ames Research Center
Moffett Field
California 94035
Attn: Technical Librarian
Designee: Harold Hornby
Mission Analysis Division

Goddard Space Flight Center
Greenbelt, Maryland 20771
Attn: Technical Librarian
Designee: Merland L. Moseson
Code 620

Jet Propulsion Laboratory
California Institute of Technology
4800 Oak Grove Drive
Pasadena, California 91103
Attn: J.H. Rupe

Attn: Technical Librarian
Designee: Henry Burlage, Jr.
Propulsion Div., 38

John F. Kennedy Space Center, NASA
Cocoa Beach, Florida 32931
Attn: Technical Librarian
Designee: Kurt H. Debus

Langley Research Center
Langley Station
Hampton, Virginia 23365
Attn: Technical Librarian
Designee: Floyd L. Thompson, Director

NASA
Lewis Research Center
21000 Brookpark Road
Cleveland, Ohio 44135
Attn: M.F. Heidmann (Technical Monitor)
R.J. Priem
E. Conrad

Attn: Technical Librarian
Designee: A. Silverstein, Director

Manned Spacecraft Center
Houston, Texas 77001
Attn: G. Spencer

Attn: Technical Librarian
Designee: Robert R. Gilruth, Director

Marshall Space Flight Center
R-P&VED
Huntsville, Alabama 35812
Attn: Jerry Thomson
R.J. Richmond

Attn: Technical Librarian
Designee: Hans G. Paul

GOVERNMENT INSTALLATIONS

Headquarters, U.S. Air Force
Washington 25, D.C.
Attn: Technical Librarian
Designee: Col. C.K. Stambaugh
AFRST

Aeronautical Systems Division
Air Force Systems Command
Wright-Patterson Air Force Base
Dayton, Ohio 45433
Attn: Technical Librarian
Designee: D.L. Schmidt
Code ASRCNC-2

Air Force Missile Test Center
Patrick Air Force Base
Florida
Attn: Technical Librarian
Designee: L.J. Ullian

Air Force Office of Scientific Research
Propulsion Division
Washington, D.C.
Attn: B.T. Wolfson

Air Force Rocket Propulsion Laboratory
Research & Technology Division
Air Force Systems Command
Edwards, California 93523
Attn: R.R. Weiss, RPRR

Attn: Technical Librarian
Designee: H. Main

Air Force Systems Division
Air Force Unit Post Office
Los Angeles 45, California
Attn: Technical Librarian

ARL (ARC)
Building 450
Wright-Patterson Air Force Base
Dayton, Ohio
Attn: K. Scheller

Arnold Engineering Development Center
Arnold Air Force Station
Tullahoma, Tennessee
Attn: Technical Librarian
Designee: H.K. Doetsch

Department of the Navy
Bureau of Naval Weapons
Washington, D.C.
Attn: Technical Librarian
Designee: J. Kay
RTMS-41

Department of the Navy
Office of Naval Research
Washington, D.C. 20360
Attn: R.O. Jackel

Defense Documentation Center Headquarters
Cameron Station, Building 5
5010 Duke Street
Alexandria, Virginia 22314
Attn: TISIA

Naval Ordnance Station
Research & Development Dept.
Indian Head, Maryland 20640
Attn: Lionel A. Dickinson

Picatinny Arsenal
Dover, New Jersey 07801
Attn: E. Jenkins

Attn: Technical Librarian
Designee: I. Forsten, Chief
Liquid Propulsion Lab.
SMUPA-DL

Redstone Scientific Information
Building 4484
Redstone Arsenal
Huntsville, Alabama
Attn: Technical Librarian

RTNT
Bolling Field
Washington, D.C. 20332
Attn: L. Green, Jr.

U.S. Army Missile Command
Redstone Arsenal
Huntsville
Alabama 35809
Attn: J. Connaughton

Attn: Technical Librarian
Designee: Walter Wharton

U.S. Atomic Energy Commission
Technical Information Services
Box 62
Oak Ridge, Tennessee
Attn: Technical Librarian
Designee: A.P. Huber
Gaseous Diffusion Plant
(ORGDP) P.O. Box P

U.S. Naval Ordnance Test Station
China Lake
California 93557
Attn: E.W. Price

Attn: Technical Librarian
Designee: Code 4562
Chief,
Missile Propulsion Div.

CPIA

Chemical Propulsion Information Agency
Applied Physics Laboratory
The John Hopkins University
8621 Georgia Avenue
Silver Spring, Maryland 20910
Attn: T.W. Christian

Attn: Technical Librarian
Designee: Neil Safeer

INDUSTRY CONTRACTORS

Aerojet-General Corporation
P.O. Box 296
Azusa, California 91703
Attn: Technical Librarian
Designee: L.F. Kohrs

Aerojet-General Corporation
P.O. Box 1947
Sacramento, California 95809
Attn: R.J. Hefner

Attn: Technical Librarian
Bldg. 2015, Dept. 2410
Designee: R. Stiff

Aeronutronic
Philco Corporation
Ford Road
Newport Beach, California 92663
Attn: Technical Librarian
Designee: D.A. Carrison

Aerospace Corporation
P.O. Box 95085
Los Angeles, California 90045
Attn: O.W. Dykema

Attn: Technical Librarian
Designee: John G. Wilder
MS-2293
Propulsion Dept.

Astrosystems International, Inc.
1275 Bloomfield Avenue
Fairfield, New Jersey 07007
Attn: Technical Librarian
Designee: A. Mendenhall

Atlantic Research Corporation
Edsall Road and Shirley Highway
Alexandria, Virginia 22314
Attn: Technical Librarian
Designee: A. Scurlock

Autonetics
Div. of North American Aviation, Inc.
3370 Miraloma Avenue
Anaheim, California 92803
Attn: Dr. Ju Chin Chu

Battelle Memorial Institute
505 King Avenue
Columbus 1, Ohio
Attn: Charles E. Day,
Classified Rept. Librarian

Bell Aerosystems Company
P.O. Box 1
Buffalo 5, New York 14240
Attn: K. Berman
J. Senneff

Attn: Technical Librarian
Designee: W.M. Smith

Boeing Company
P.O. Box 3707
Seattle, Washington 98124
Attn: Technical Librarian
Designee: J.D. Alexander

Bolt, Berenak & Newman, Inc.
Cambridge, Mass.
Attn: Dr. Dyer

Chrysler Corporation
Missile Division
P.O. Box 2628
Detroit, Michigan 48231
Attn: Technical Librarian
Designee: John Gates

Curtiss-Wright Corporation
Wright Aeronautical Division
Wood-Ridge, New Jersey 07075
Attn: Technical Librarian
Designee: G. Kelley

Defense Research Corporation
6300 Hollister Avenue
P.O. Box 3587
Santa Barbara, California 93105
Attn: B. Gray
C.H. Yang

Douglas Aircraft Company
Missile & Space Systems Division
3000 Ocean Park Boulevard
Santa Monica, California 90406
Attn: Technical Librarian
Designee: R.W. Hallet
Advanced Space Tech.

Douglas Aircraft Company
Astropower Laboratory
2121 Paularino
Newport Beach, California 92663
Attn: Technical Librarian
Designee: George Moc
Director, Research

Dynamic Science Corporation
1445 Huntington Drive
South Pasadena, California
Attn: M. Beltran

General Dynamics/Astronautics
Library & Information Services (128-00)
P.O. Box 1128
San Diego, California 92112
Attn: Technical Librarian
Designee: Frank Dore

General Electric Company
Advanced Engine & Technology Dept.
Cincinnati, Ohio 45215
Attn: Technical Librarian
Designee: D. Suichu

General Electric Company
Malta Test Station
Ballston Spa, New York
Attn: Alfred Graham, Manager
Rocket Engines

General Electric Company
Re-Entry Systems Department
3198 Chestnut Street
Philadelphia, Pennsylvania 19101
Attn: Technical Librarian
Designee: F.E. Schultz

Geophysics Corporation of America
Technical Division
Bedford, Massachusetts
Attn: A.C. Toby

Grumman Aircraft Engineering Corp.
Bethpage
Long Island, New York
Attn: Technical Librarian
Designee: Joseph Gavin

Institute for Defense Analyses
RESO
400 Army-Navy Drive
Arlington, Virginia
Attn: Warren C. Strahle

Ling-Temco-Vought Corporation
Astronautics
P.O. Box 5907
Dallas, Texas 75222
Attn: Technical Librarian
Designee: Warren C. Trent

Arthur D. Little, Inc.
20 Acorn Park
Cambridge, Massachusetts 02140
Attn: E. Karl Bastress
Attn: Technical Librarian

Lockheed Missiles & Space Co.
P.O. Box 504
Sunnyvale, California 94088
Attn: Technical Information Center
Designee: Y.C. Lee

Lockheed Propulsion Company
P.O. Box 111
Redlands, California 91409
Attn: Technical Librarian
Designee: H.L. Thackwell

McDonnell Aircraft Corporation
P.O. Box 516
Municipal Airport
St. Louis, Missouri 63166
Attn: Technical Librarian
Designee: R.A. Herzmark

The Marquardt Corporation
16555 Saticoy Street
Van Nuys, California 91409
Attn: Technical Librarian
Designee: Warren P. Boardman, Jr.

Martin Marietta Corporation
Denver Division
P.O. Box 179
Denver, Colorado 80201
Attn: Technical Librarian
Designee: J.D. Goodlette (A-241)

Multi-Tech. Inc.
Box 4186 No. Annex
San Fernando, California
Attn: F. B. Cramer

Northrup Space Laboratories
3401 West Broadway
Hawthorne, California
Attn: Technical Librarian
Designee: William Howard

Rocket Research Corporation
520 South Portland Street
Seattle, Washington 98108
Attn: Technical Librarian
Designee: Foy McCullough, Jr.

Rocketdyne
Division of North American Aviation
6633 Canoga Avenue
Canoga Park, California 91304
Attn: R. Fontaine
R.B. Lawhead

Attn: Technical Librarian
(Library 586-306)
Designee: E.B. Monteath

Space & Information Systems Division
North American Aviation, Inc.
12214 Lakewood Boulevard
Downey, California 90241
Attn: Technical Librarian
Designee: H. Storms

Rohm & Haas Company
Redstone Arsenal
Huntsville, Alabama
Attn: Librarian

Stanford Research Institute
333 Ravenswood Avenue
Menlo Park, California 94025
Attn: Technical Librarian
Designee: G. Marxman

Thiokol Chemical Corporation
Huntsville Division
Huntsville, Alabama
Attn: Technical Librarian
Designee: John Goodloe

Thiokol Chemical Corporation
Reaction Motors Division
Denville, New Jersey 07832
Attn: D. Mann
Attn: Technical Librarian
Designee: Arthur Sherman

TRW Systems
One Space Park
Redondo Beach, California 90278
Attn: G.W. Elverum
Attn: Donald H. Lee
Attn: Technical Librarian
Designee: Sam J. Van Grouw

United Technology Center
Division of United Aircraft Corporation
P.O. Box 358
Sunnyvale, California 94088
Attn: R.H. Osborn
Attn: Technical Librarian

Pratt & Whitney Aircraft Company
Division of United Aircraft Corp.
West Palm Beach
Florida
Attn: G. Lewis

Pratt & Whitney Aircraft Company
Division of United Aircraft Corp.
Engineering, Building 1-F
East Hartford, Connecticut
Attn: D.H. Utvik

Research Laboratories
Division of United Aircraft Corp.
400 Main Street
East Hartford, Connecticut 06108
Attn: Technical Librarian
Designee: Erle Martin

Walter Kidde and Company
Aerospace Operations
567 Main Street
Belleville, New Jersey 07109
Attn: Technical Librarian
Designee: R. J. Hanville

Warner-Swasey Company
Control Instrument Division
32-16 Downing Street
Flushing, New York 11354
Attn: R.H. Tourin

UNIVERSITIES

California Institute of Technology
204 Karman Laboratory
Pasadena, California 91109
Attn: Fred E. Culick

Case Institute of Technology
Engineering Division
University Circle
Cleveland, Ohio 44106
Attn: C.R. Klotz

Dartmouth University
Hanover
New Hampshire
Attn: P.D. McCormack

Georgia Institute of Technology
Aerospace School
Atlanta 13
Georgia
Attn: Ben T. Zinn

Illinois Institute of Technology
10 W. 35th Street
Chicago, Illinois
Attn: P.T. Torda

The John Hopkins University
Applied Physics Laboratory
8621 Georgia Avenue
Silver Spring, Maryland
Attn: W.G. Berl

Massachusetts Institute of Technology
Cambridge 39
Massachusetts
Attn: T.Y. Toong
Dept. of Mechanical Engineering
Attn: Gail E. Partridge, Librarian
Engineering Projects Laboratory

New York University
Dept. of Chemical Engineering
New York 53, New York
Attn: P.F. Winternitz

Ohio State University
Rocket Research Laboratory
Dept. of Aeronautical & Astronautical Eng.
Columbus 10, Ohio
Attn: Technical Librarian

Polytechnic Institute of Brooklyn
Graduate Center
Route 110
Farmingdale, New York
Attn: V.D. Agosta

Purdue University
School of Mechanical Engineering
Lafayette, Indiana
Attn: J.R. Osborn

Sacramento State College
Engineering Division
60000 J. Street
Sacramento, California 95819
Attn: F.H. Reardon

Sheffield University
Research Laboratories
Harpur Hill
Buxton, Derbyshire
England
Attn: V.J. Ibberson

University of California
Institute of Engineering Research
Berkeley, California
Attn: A.K. Oppenheim

University of Michigan
Aeronautical & Astronautical Eng. Labs.
Aircraft Propulsion Lab.
North Campus
Ann Arbor, Michigan
Attn: J.A. Nicholls

University of Southern California
Dept. of Mechanical Engineering
University Park
Los Angeles, California 90007
Attn: M. Gerstein

University of Wisconsin
Dept. of Mechanical Engineering
1513 University Avenue
Madison, Wisconsin
Attn: P.S. Myers

Yale University
Dept. of Engineering & Applied Science
Mason Laboratory
400 Temple Street
New Haven, Connecticut
Attn: B.T. Chu